Tandem Mass Spectrometric and Ion Mobility Studies of Supramolecular Complexes

Inaugural-Dissertation

to obtain the academic degree

Doctor rerum naturalium (Dr. rer. nat.)

submitted to the Department of Biology, Chemistry and Pharmacy

of Freie Universität Berlin

by

Jan-Marwin Wollschläger

2019

This thesis was developed under the supervison of Prof. Dr. Christoph A. Schalley between November 2016 and March 2019 at the Department of Biology, Chemistry and Pharmacy of Freie Universität Berlin.

1st Referee: Prof. Dr. Christoph A. Schalley

2nd Referee: Prof. Dr. Beate Paulus

Date of defence: 02.07.2019

Abstract

Synthetic supramolecular systems share many similarities with natural biological assemblies, especially when considering that the structure and guest binding are typically governed by non-covalent interactions. As such, the defining characteristic is that only comparably weak forces define the shape of a synthetic supramolecule or the tertiary structure of a protein, so that the resulting dynamic binding mode makes structure elucidation challenging. One of the major advances in recent analytical chemistry has been the development of ion mobility-mass spectrometry (IM-MS) to tackle the challenging problems faced in proteomics, glycomics, metabolomics, and lipidomics. By analogy, the prospects of applying IM-MS to supramolecules are bright and it is to be expected that unprecedented analytical insights into diverse systems such as host-guest complexes, molecular devices, self-assemblies and metallosupramolecular complexes will be obtained.

The recurrent theme throughout this dissertation is that both structure (differentiation of diastereomers, photoisomers, mechanoisomers) and non-covalent interactions (hydrogen bonding, TTF^{n+}/TTF^{n+}-charge repulsion, dispersive interactions) can be investigated by a combination of the three methods of ion-mobility mass spectrometry (IM-MS), collision-induced dissociation (CID) and gas-phase H/D-exchange (GP-HDX). In the study of the gas-phase chiral recognition of crown-ether ammonium complexes, the importance of a single hydrogen bond for the enantiodifferentiation was revealed. Similarly, in an azobenzene model a hydrogen bonding interaction led to an increased stability of the (*Z*)-photoisomer. This surprising observation illustrates an important aspect, namely that there can be significant differences between the gas-phase and the solution environment. In the absence of solvent, both the stabilization of charged sites and the Coulomb repulsion of nearby charges are accentuated.

In a way, the conundrum of supramolecular mass spectrometry revolves around the problem that ions are easily manipulated in the gas-phase where a high analytic resolution power is available, to then face the question if the obtained results still reflect the solution environment.

Therefore, it is very convincing to see that in three of the five presented studies, the solution environment is reflected in a quantitative fashion: In the quantification of the enantiomeric excess (first study), the quantification of photoisomer content (second

study), and the quantitative determination of equilibrium constants for redox-controlled dethreading (third study).

Together with these five studies, and the detailed description in the subsequent chapters, I expect the treatment to be useful also from the practitioner's point of view. It is my hope that the performance, speed, and reliability with which measurements can be performed with modern instrumentation will make IM-MS a routine analytical tool in the repertoire of the working supramolecular chemist.

Zusammenfassung

Synthetische Supramoleküle haben viele Gemeinsamkeiten mit natürlichen biologischen Systemen. Besonders ins Auge fällt die Tatsache, dass in beiden Fällen nicht-kovalente Wechselwirkungen strukturbestimmend sind. Während sich sowohl die Natur, z.B. bei der Tertiärstruktur von Proteinen, als auch der supramolekulare Chemiker, z.B. bei der Synthese von Inklusionsverbindungen, diesen dynamischen Bindungsmodus zunutze machen, stellt die Untersuchung von nicht-kovalenten Wechselwirkungen die analytische Chemie vor große Herausforderungen.

Um diesen Herausforderungen an die moderne Strukturaufklärung gerecht zu werden, hat sich in den letzten Jahren die Kupplung der Ionenmobilitätsmassenspektrometrie (IM-MS) als besonders vielversprechend hervorgetan. So konnten viele Fortschritte im Bereich der Protein-, Lipid- und Kohlenhydratanalytik erzielt werden. Es erscheint daher naheliegend, dass IM-MS in Zukunft auch neue Einblicke in synthetisch-supramolekulare Systeme verschaffen wird.

Ein wiederkehrendes Motiv in meiner Dissertation ist, dass sowohl die Struktur (z.B. die Unterscheidung von Isomeren) als auch die nicht-kovalenten Wechselwirkungen (z.B. Wassterstoffbrückenbindungen, TTF^{n+}/TTF^{n+}-Ladungsabstoßung) durch die Kombination von Ionenmobilitätsmassenspektrometrie (IM-MS), kollisionsinduzierter Dissoziation (CID) und Gasphasen-H/D-Austausch (GP-HDX) untersucht werden können. So konnte in einer chiralen Erkennungsstudie von Kronenether/Ammonium-Komplexen in der Gasphase die Auswirkung einer einzelnen Wasserstoffbrücke auf die Enantiodifferenzierung gezeigt werden. Im Falle des später vorgestellten Azobenzolmodellsystems führt eine Wasserstoffbrücke sogar dazu, dass das (Z)-Azobenzol in der Gasphase das stabilere Photoisomer ist. Dies ist eine überraschende Beobachtung und offenbart, dass sich die Verhältnisse zwischen Lösung und Gasphase dramatisch voneinander unterscheiden können. In Abwesenheit stabilisierenden Lösungsmittels treten ladungsstabilisierende Kräfte und Coulomb-Abstoßung in den Vordergrund. Somit ergibt sich für die supramolekulare Gasphasenchemie die etwas widersprüchliche Situation, dass die Massenspektrometrie einerseits die gezielte Manipulation einzelner Ionen – und somit eine hohe Trennkapazität – erlaubt, andererseits aber die Relevanz der erhaltenen Daten für die Lösungsumgebung unsicher bleibt.

Wie die vorliegende Arbeit anhand von fünf Studien zeigt ist es jedoch sehr wohl

möglich, klare Rückschlüsse auf die Lösungsumgebung zu ziehen. Unter anderem konnten die enantiomere Zusammensetzung (erste Studie), der Anteil von Photoisomeren (zweite Studie) und die Lage eines redox-induzierten Abfädelungsgleichgewichtes (dritte Studie) in hoher Übereinstimmung mit der Lösungsumgebung quantifiziert werden.

Ich hoffe, dass mit der vorliegenden Arbeit IM-MS als performante, schnelle und zuverlässige Technik auch aus praktischer Sicht für den supramolekularen Chemiker zugänglicher wird.

Contents

List of abbreviations

AM1	Austin model 1
ATD	arrival time distribution
CID	collision-induced dissociation
CCS	collision cross section
CRM	charge residue model
CV	cyclic voltammetry
DFT	density functional theory
DPV	differential pulse voltammetry
DT-IMS	drift tube ion mobility spectrometry
EHS	exact hard sphere scattering
EPR	electron paramagnetic resonance
ESI	electrospray ionization
EXSY	exchange spectroscopy
FT-ICR	Fourier transform ion cyclotron resonance
GP-HDX	gas-phase H/D-exchange
HPLC	high performance liquid chromatography
IEM	ion evaporation model
IM-MS	ion mobility-mass spectrometry
IMS	ion mobility spectrometry
IRMPD	infrared multi photon dissociation
MS	mass spectrometry
NMR	nuclear magnetic resonance
PA	projection approximation
PM3	parameterized model 3
TM	trajectory method
TOF	time of flight
TTF	tetrathiafulvalene
TW-IMS	travelling wave ion mobility spectrometry

1
CHAPTER

Introduction

The rising interest in functional supramolecular materials goes along with an increasing demand for analytical methods suitable for the investigation of these systems. This is why the further development of modern mass spectrometric gas-phase characterization techniques is of high interest to the chemical community and will in the long run not only facilitate the development of new supramolecular materials, such as molecular shuttles and motors, but—even more importantly—provide deeper insights into both the structure and the dynamics of these systems. A combination of multiple gas-phase characterization techniques enables a deeper understanding of such systems that will inevitably also lead to the development of new supramolecular materials, including molecular devices, such as molecular shuttles and motors.

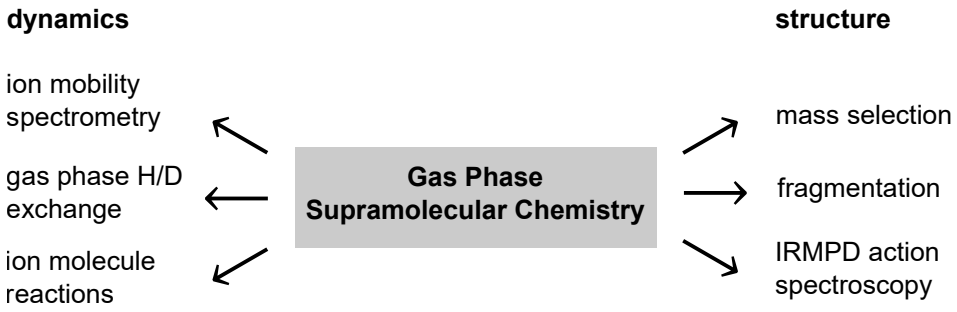

The aim of the present dissertation project is the study of supramolecular complexes with advanced mass spectrometric techniques. The focus lies on the structure, especially the differentiation of isomers, and the identification of intramolecular forces of these systems. A particularly intriguing aspect of studying supramolecular systems in the gas-phase is the possibility of investigating intramolecular forces such as hydrogen bonding and van der Waals forces—both being major motifs in protein folding, enzyme catalysis and molecular recognition in general—with simplified biological mimics in the absence of solvent. The systems investigated in the five reported publications are structurally diverse and include crown-ether ammonium pseudorotaxanes and oligorotaxanes, azobenzene switches, and titanium helicates.

Supramolecular chemistry is a large field that comprises a multitude of different classes of new materials, the common feature being that the chemical systems under study are made up from smaller molecular subunits. The forces holding these subunits together are manifold, rising from weak van der Waals and π-π interactions to strong interactions like electrostatic forces or hydrogen bonding. As shown in Table 1, these interactions vary in strength over a wide range of few kJ/mol up to several hundred kJ/mol.[1,2]

Table 1: Overview over types of interactions and bonding important in supramolecular chemistry.[1,2]

bond type	bond energy [kJ/mol]	example
covalent bond	120 - 500	ubiquitous
coordinative bond	80 - 340	potassium ferricyanide
hydrogen bonding	4 - 120	DNA
ion-ion interaction	200 - 300	tetrabutylammonium chloride
ion-dipole interaction	50 - 200	$Na^{\oplus}$ ⋯ [15]-crown-5
cation-π interaction	5 - 80	$K^{\oplus}$ in benzene
dipole-dipole interaction	5 - 50	acetone
π-π interaction	0 - 50	benzene
van-der-Waals interaction	4 - 20	argon

An important class of supramolecules are the so-called mechanically interlocked molecules (MIMs), as indicated in Figure 1. These are held together by their interlocked three-dimensional arrangement, thus representing a mechanical type of bond, though additional intramolecular forces between subunits might exist as well. While catenanes consist of two interlocking rings, rotaxanes are characterized by a linear molecule (termed the axle) being threaded through a macrocycle (termed the wheel), without spontaneous dethreading. All systems that have been studied in this thesis are marked in red, together with a page reference to the study. Together with the work of Anneli Kruve-Viil, who focused on the study of catenanes and knots, the work of our group encompasses almost all types of supramolecular systems, and all types of MIMs, and shows the generality of gas-phase supramolecular chemistry methods. A more detailed and highly interesting presentation of mechanostereochemistry can be found in the recent textbook of Stoddart and Bruns and related publications.[3,4]

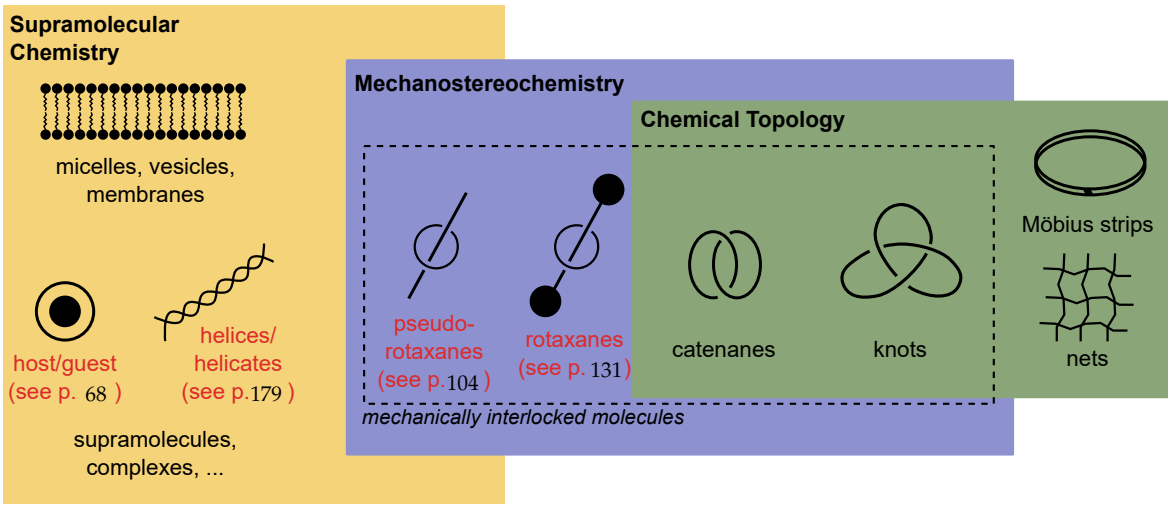

Figure 1: Overview over the different types of materials under study in supramolecular chemistry. Recently, attention has shifted to the class of mechanically interlocked molecules (MIMs) due to their applications as molecular devices. Types of systems studied in this thesis are marked in red. My studies focused on (pseudo-)rotaxanes, host/guest complexes and helicates.

The mechanical bonding between axle and wheel provides a means to assemble new molecular shapes in a modular fashion. In our group, rotaxanes and pseudorotaxanes thus present a central focus in the development of new materials.

Recently, our group developed a divalent pentastable redox-switchable donor-acceptor rotaxane,[5] and showed that a photoswitchable rotaxane can operate on solid support.[6,7] These materials are promising for applications as stimuli-responsive materials and as a starting point for building molecular devices. Going along with these new developments, an increased understanding of the structure and the non-covalent interactions in these complexes is pivotal. With that aim in mind, our group has developed several systems to study multivalent binding, including chelate and allosteric cooperativity effects.[8–11] In these studies, isothermal titration calorimetry (ITC) is used to determine binding energies and to differentiate enthalpic and entropic contributions to the multivalent binding interactions. By systematically varying the host and guest systems in a double mutant cycle, detailed knowledge about the multivalent binding interactions, including chelate and cooperativity effects, is obtained.[8–11]

In multivalent binding, several weak interactions add up to create the overall binding event, the guiding principle that takes effect in many natural processes as well.

Due to the very nature of multivalent binding—with several weak interactions at different locations—analysis in the solution state can be challenging. This is why our group

attempts to extend our knowledge about non-covalent binding in the gas phase through mass spectrometry and ion mobility spectrometry. We have recently summarized the advantages of studying molecular containers with these gas-phase techniques.[12]
While X-ray crystallography and NMR spectroscopy are widely employed analytical methods in supramolecular chemistry, electrospray ionization (ESI)-MS is continuously increasing in importance as a key technique for the characterization of supramolecules providing the three "S" advantages highlighted by McLafferty: specificity, sensitivity and speed.[12] ESI-MS can be used to study the solution environment and has been employed successfully in numerous studies including protein folding and enzyme catalysis.[12] On the other hand, isolated ions are studied in high vacuum. Thus, properties and reactivity intrinsic to the isolated ion of interest can be investigated in the absence of solvent. This is particularly advantageous for supramolecular systems as fast guest/ligand exchanges would often occur in solution, thereby complicating the analysis. For studying non-covalent interactions, the simplification provided by isolating the species of interest and stripping off the solvent environment not only makes the experimental results easier to interpret but also facilitates the comparison with electronic structure calculations that are typically carried out in the gas phase.
ESI is a very efficient ionization method, that can be used to ionize most of the systems encountered in supramolecular chemistry. For very weakly bound complexes, cold-spray ionization (CIS) is useful, where the sample solution and ion source are cooled, thereby generating ions with lower internal energy to prevent early fragmentation.[13]
The efficiency with which ESI and its variants ionizes most classes of polar compounds means that many supramolecular systems can be easily transferred into the gas phase. Once the ion has been isolated in the high vacuum of the mass spectrometer, shown in Figure 2A, a wide array of gas-phase techniques is available to study its structure, dynamics and reactivity. Several MS/MS techniques (CID, IRMPD, BIRD, ...) may be used to fragment the isolated species (B), thereby gaining insight into the connectivity of the ion as well as the strength of intramolecular forces. In that regard, gas-phase H/D-exchange (C) has to be mentioned, as it provides a way to study the dynamics of the subunits contained in the supramolecule and the intercomponent binding between them and was used in our group to reveal the hydrogen bonding and dynamic behavior of supramolecular systems in the gas phase.[14–17]

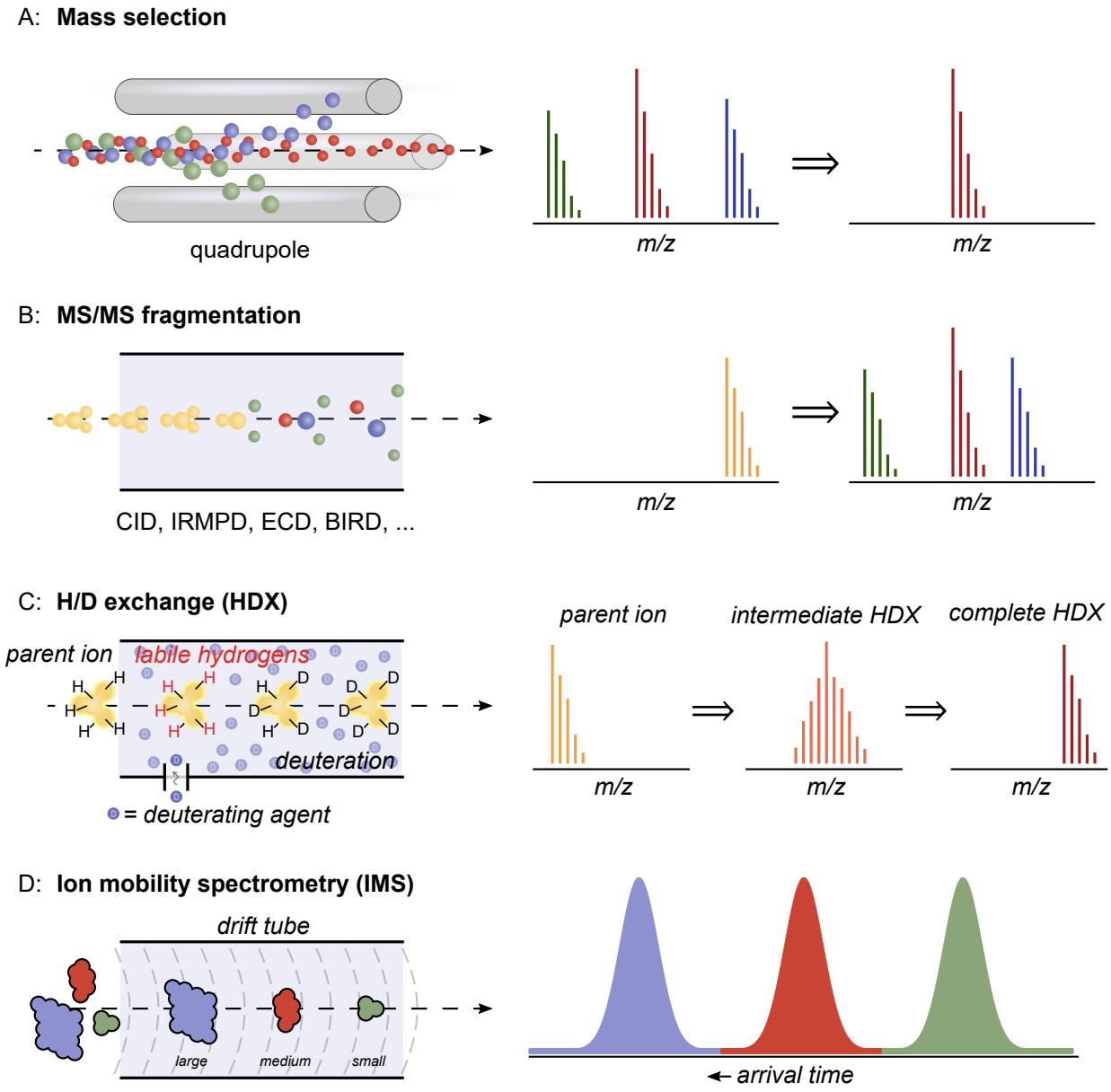

Figure 2: After isolation of a selected ion into the high vacuum of the mass spectrometer, many different gas-phase techniques are available to study both structure and dynamics of the isolated species.

Finally, ion mobility-mass spectrometry (IM-MS) is a rapidly developing field, since commercial instruments have become broadly available lately. As shown in Figure 2D, the analyte ions are pulled through a drift tube by an electric field. The drift tube is filled with a buffer gas, such as nitrogen or helium. As the analyte ions collide with the molecules of the buffer gas, their movement through the drift tube is slowed down. Bigger ions collide with the buffer gas more often, thereby delaying their arrival at the detector. As the result, information about the size of the ion is obtained from the arrival-time distribution (ATD). This is an important improvement as isomers and

different conformations can be differentiated that were formerly indistinguishable by MS due to having the same m/z. This advantage has been exploited in the study of many natural systems and many insights have been gained about the conformation of biomolecules in the gas phase.[18–20] However, we feel that the advantages of IMS in the field of supramolecular systems are largely unexploited, a gap that needs to be filled as IMS greatly enhances the amount of information about the isolated gas-phase species. Each of these modern mass spectrometric methods will be discussed in more detail in the following methods section.

2

CHAPTER

Methods

2.1 Electrospray ionization (ESI)

Electrospray ionization (ESI) is a soft ionization method where analytes may be either inherently positively or negatively charged ions or neutral molecules, in which case ionization is achieved by attachment of ions from the solution (e.g. H^+, Na^+, Cl^-) or deprotonation during the ESI process. ESI belongs to the group of atmospheric pressure (AP) ionization methods and allows for easy liquid chromatography-mass spectrometry (LC-MS) coupling. It is a soft ionization method that is suited for the analysis of large and non-volatile polar compounds such as proteins and DNA.[21,22] Particularly convenient is the formation of multiply charged species, so that ions with high molecular mass are shifted into a smaller *m/z*-range covered by most (cheaper) analyzers. Furthermore, due to the low amount of fragmentation, interpretation of the results, including determination of the molecular mass, is simplified considerably. These advantages make ESI the ionization method of choice in many biological applications including proteomics, metabolomics and glycomics. Another promising field is the study of supramolecular systems, which is the topic of this work. Figure 3 explains the working principle behind the ESI method.[22,23] Typically, a polar solvent (e.g. MeOH, H_2O, MeCN) containing the analyte is pumped through a capillary needle. A high voltage source (1-5 kV) establishes an electric field between the needle and a plate with an inlet into the mass spectrometer. Due to the strong electrical field the liquid is drawn through the tip of the needle, forming a so called Taylor cone. From there, solvent droplets containing the analyte ions M^+ are emitted and subsequently accelerated in the electric field towards the plate. On their way, solvent molecules evaporate from the droplets, while the charge remains. As a result, the charge density on the surface increases until the Rayleigh limit is reached.[21–23]

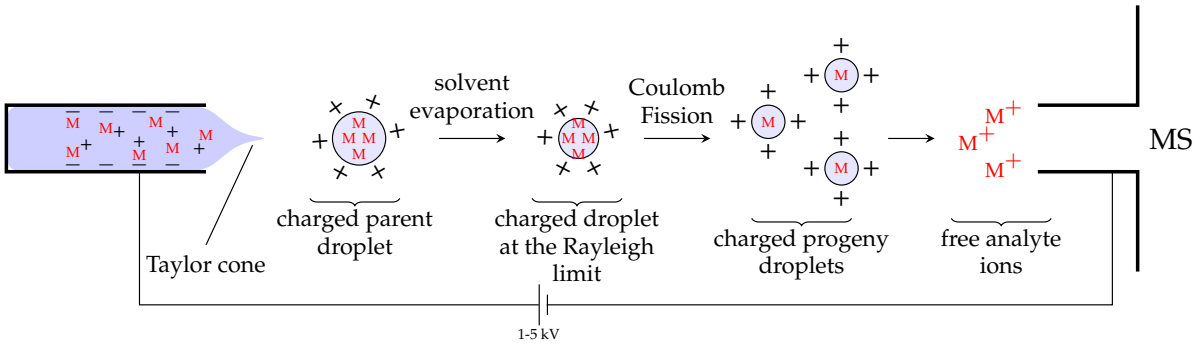

Figure 3: Schematic description of the ESI process.

There are two models by which the formation of the free gas-phase ions can be explained (*see* Figure 4).[24] In the ion evaporation model (IEM), the droplets get smaller until the field strength gets high enough to directly emit the ion from the solvent droplet into the gas phase. In the charge residue model (CRM), the droplets undergo evaporation up to a point at which the force of Coulomb repulsion at the surface overcomes the surface tension.[24] The droplet releases charge and mass in a so called *Coulomb fission*. From there, clusters of solvent and analyte undergo further evaporation finally yielding desolvated gas-phase ions. Small ions are liberated into the gas phase according to the IEM, while larger ions are formed as described by the CRM.[24] One common adaptation of ESI is the so called Z-spray which provides a more efficient and cleaner way of generating ions and separating them from solvent and buffer molecules.[24,25]

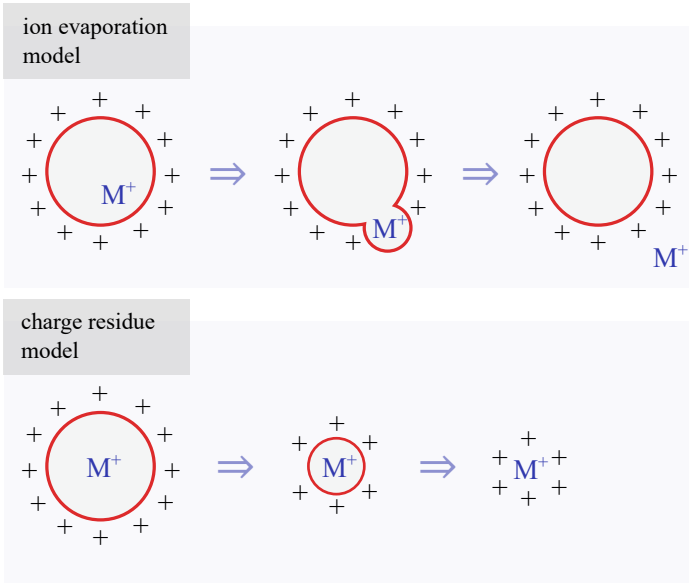

Figure 4: Illustration of the ion evaporation and the charge residue model.

In a conventional ESI source, ions travel along a straight line into the instrument, as shown on the left side of Figure 5. Even though most of the neutral molecules will diffuse to the edge of the spray cone and finally be absorbed by the vacuum system, some solvent molecules still arrive at the orifice towards the mass analyzer, the so called skimmer. The solvent molecules/neutrals deposit and can thereby block the skimmer

hole. The Z-spray prevents this problem by sending the ions on a Z-shaped trajectory, as illustrated on the right side of Figure 5. By use of this configuration, only analyte ions enter the orifice of the mass analyzer, whereas neutral molecules are quickly removed by the vacuum system.[25]

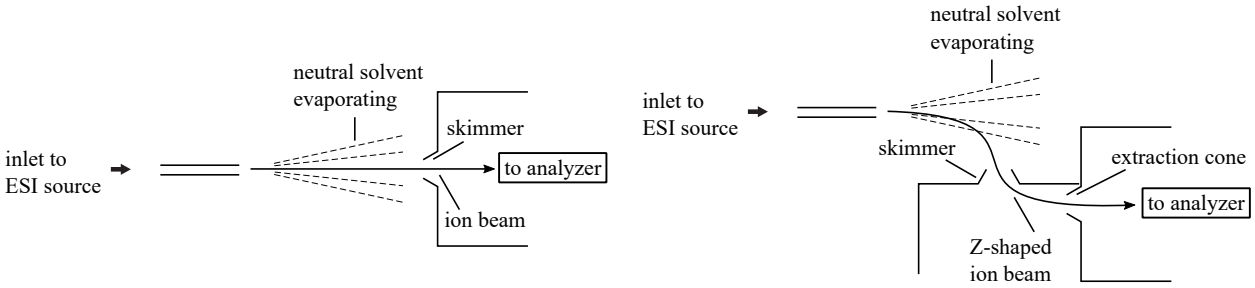

Figure 5: Illustration of a normal ESI source (*left*) in comparison to the Z-spray ion source (*right*).

2.2 Ion mobility-mass spectrometry (IM-MS)

The rapid advances in ion mobility-mass spectrometry (IM-MS) are starting to have a significant impact on the analytical laboratories worldwide. While the history of plain ion mobility spectrometry (IMS) reaches back about 50 years,[26] the more recent hyphenation of ion mobility with mass spectrometry greatly expanded the scope. The combination of the well-known analytical advantages of high-resolution mass spectrometry with the molecular size and shape information from the ion mobility dimension results in an unprecedented analytical power. Applications span across a plethora of very different fields such as small-molecule chemistry, pharmacology, proteomics, and glycomics.[27–30]

2.2.1 Drift-tube ion mobility spectrometry (DT-IMS)

When ions are exposed to an electric field (see Figure 6), they are accelerated along the field lines and thus guided trough the drift cell according to the equation

$$m \cdot a = E_{\mathrm{el}} \cdot q, \tag{2.1}$$

where m is the mass, a is the acceleration, E_{el} is the electric field strength and q is the charge of the ion. This simple motion is distorted upon the addition of a buffer gas, as collisions with molecules in the gas scatter the ions in random directions. Under the assumption that the electric field is uniform, the ion cloud thus gains a constant velocity along the field lines, simultaneously growing in size due to diffusion. This constant velocity can be explained by the cancellation of two opposing forces, the electric field force accelerating and the friction force due to collisions with the buffer gas deaccelerating the ions at equilibrium.[26,31,32] Thus, we obtain

$$v_{\mathrm{d}} = K \cdot E_{\mathrm{el}}, \tag{2.2}$$

where v_{d} is the drift velocity, E_{el} is the electric field strength and K is a proportionality constant called the ion mobility.

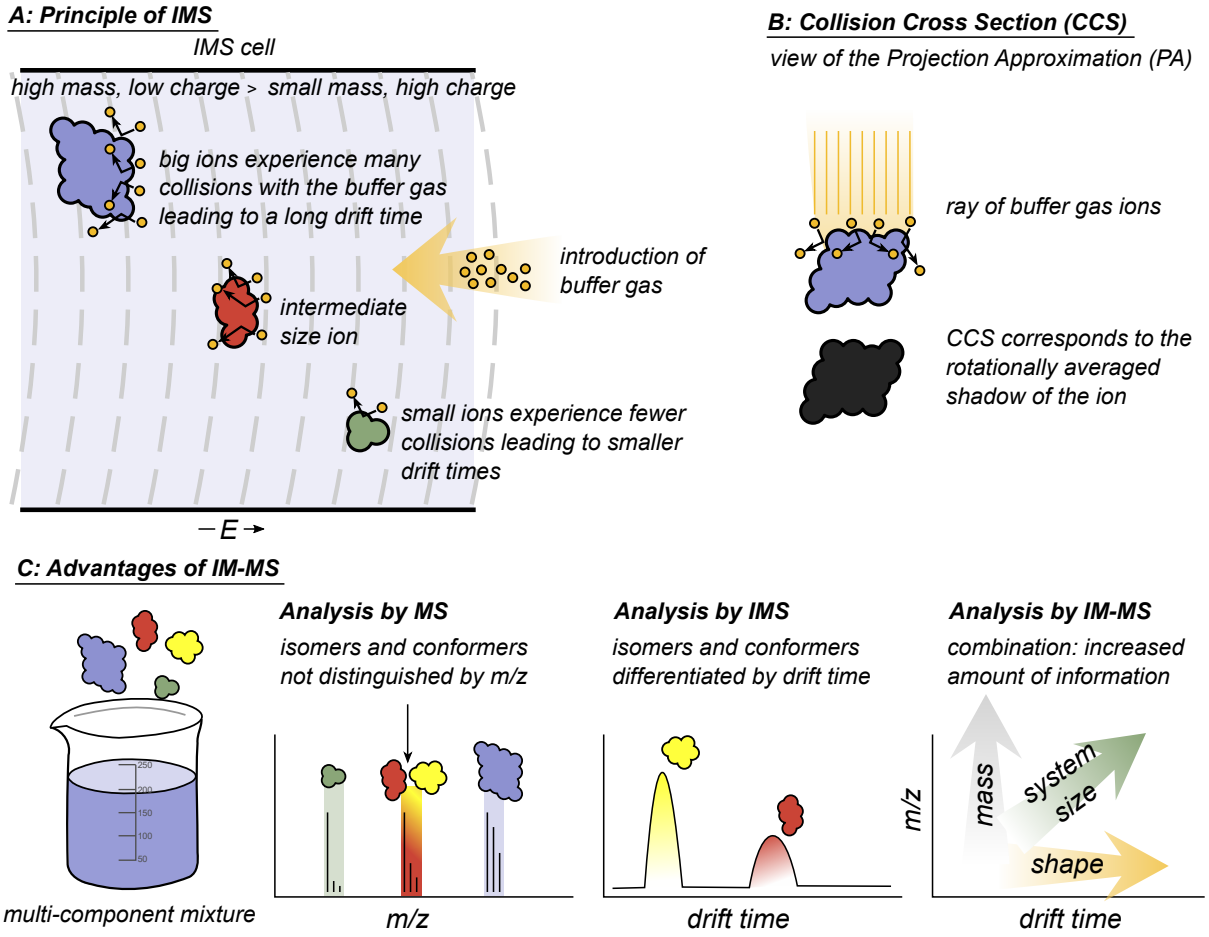

Figure 6: A: General principle of ion mobility spectrometry. Ions are accelerated in an electric field inside the IMS cell. Big ions experience many collisions with the buffer gas leading to a long drift time, while small ions experience fewer collisions leading to a smaller drift time. B: The collision cross section (CCS) gives an instrument-independent description of the size of an ion, that can be thought of as the rotationally averaged shadow of the ion. C: The combination of mass spectrometry with ion mobility spectrometry leads to the hyphenated technique IM-MS.

As K is dependent on the applied temperature and pressure, it is convenient to define the reduced ion mobility K_ϕ such that

$$K_\phi = \frac{p}{p_\phi} \cdot \frac{T_\phi}{T} \cdot K, \tag{2.3}$$

where $p_\phi = 1013$ mbar and $T_\phi = 273$ K so that K_ϕ is independent of the temperature and pressure in use.[26,31] By use of equation 2.2 and the fact that $v_\mathrm{d} = L \cdot t_\mathrm{d}^{-1}$, we obtain

$$t_\mathrm{d} = \frac{L}{K \cdot E_\mathrm{el}} + t_0, \tag{2.4}$$

where t_0 is the dead time of the system. We apply the fact that

$$E_{el} = U \cdot L^{-1} \qquad (U \text{ const.}), \tag{2.5}$$

leading to

$$t_d = \frac{L^2}{K \cdot U} + t_0, \tag{2.6}$$

so that the ion mobility K can be calculated from the slope of the curve obtained by plotting the drift time t_d against the reciprocal voltage U^{-1}.[26,31]

2.2.2 The Mason Schamp equation

Given the reduced mass μ, the temperature T, the charge $q \cdot e$ and the number density N (i.e. the number of buffer gas molecules per unit volume), the Mason Schamp equation[30]

$$\Omega = \frac{3}{16} \cdot \sqrt{\frac{2\pi}{\mu k_B T}} \cdot \frac{q e}{N K_\phi} \tag{2.7}$$

allows for the calculation of the collision cross section σ from the reduced ion mobility K_ϕ. The collision cross section Ω is a device-independent description of the size of a molecule, that can be derived by theoretical models as well.[26,30]

2.2.3 Travelling wave ion mobility spectrometry (TW-IMS)

In travelling wave ion mobility spectrometry (TW-IMS), a sequence of symmetric potential waves is continuously propagating through a tube, thereby pulling ions through the IMS system, as shown in Figure 7. The velocity by which an ion is propelled along the wave depends on the ion's mobility *K*, so that different species transit the cell in unequal drift times.[33] The ion dispersion capability and good sensitivity have made TW-IMS an attractive platform for structural biology and handling of complex separation tasks.

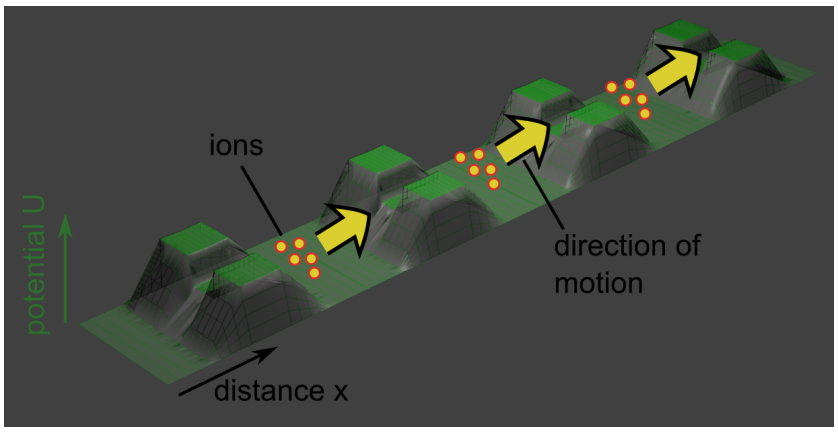

Figure 7: Dynamic electric field propelling ions in a travelling wave IMS system.

Despite its successful commercialization, for example in the Waters Synapt implementation, the fundamentals of TW-IMS have been understood only qualitatively. Therefore, CCS values can only be deduced from TW-IMS data via empiric multipoint calibration (see section 6.6, appendix, for a detailed procedure) using ions of known mobility (for example determined by DT-IMS).[33]

2.2.4 The collision cross section (CCS)

The simplest description of the collision cross section is given via the projection approximation (PA), where the CCS is given as the shadow projected by imaginary buffer gas rays hitting the molecular surface and rotationally averaging the result (see Figure 8A). This procedure can formally be expressed in terms of the integral

$$\Omega_{PA} = N \cdot \int_0^{2\pi} \int_0^{\pi} \int_{-\infty}^{+\infty} \int_{-\infty}^{+\infty} M(\phi, \psi, x, y)\, dx\, dy\, d\phi\, d\psi, \tag{2.8}$$

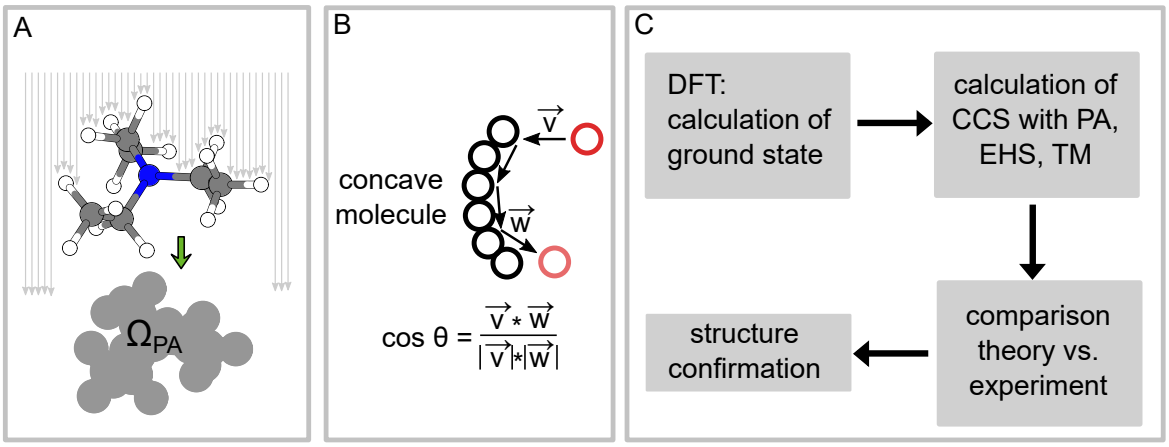

Figure 8: A: In the projection approximation (PA), the CCS is defined as the rotationally averaged "shadow" of the ion. B: In the exact hard-sphere scattering (EHS), the scattering angle of the buffer gas molecule with the ion is taken into account. In particular, grazing collisions and multiple collisions with the buffer gas can be taken into account. C: The typical CCS interpretation workflow. After the ground state† has been calculated with a suitable electronic structure method (often DFT), the CCS is predicted via PA, EHS, or TM. The theoretical value may then be compared with the experimental value so that the structure of the ion can be confirmed.

where we define

$$M(\phi, \psi, x, y) = \begin{cases} 1 & \text{if a collision occurs} \\ 0 & \text{otherwise.} \end{cases} \tag{2.9}$$

Here, ϕ is the polar angle, and ψ is the azimuthal angle of rotation around the geometric center, and N is a normalization constant. With increasingly higher resolution of the IMS instrumentation, it was felt that a more elaborate description of the CCS value was needed. The exact hard sphere scattering (EHS) method[34] assumes an infinite hard wall potential between each atom of the ion and the buffer gas molecules. By taking the scattering angle, θ, into account, grazing collisions and multiple collisions in concave ions are treated, as illustrated in Figure 8B. Formally, the EHS method can be expressed in terms of the integral

$$\Omega_{EHS} = N \cdot \int_0^{2\pi} \int_0^{\pi} \int_{-\infty}^{+\infty} \int_{-\infty}^{+\infty} 1 - \cos\theta(\phi, \psi, x, y)\, dx\, dy\, d\phi\, d\psi, \tag{2.10}$$

that also shows the similarity of the approach to the PA method. An even more elaborate treatment is provided by the trajectory method (TM), where the collisions are

†Here and throughout the rest of the text the word *ground state* refers to the set of 3D coordinates $\vec{r}$ of a molecular structure for which the geometry optimization algorithm converged, meaning that the energy $E(\vec{r})$ is at a local minimum. That is, the derivative of the energy with respect to the position of the atoms, $\frac{\partial E}{\partial \vec{r}}$, is the zero vector and the second derivative matrix of the system, $\frac{\partial \partial E}{\partial r \partial r}$, also known as the Hessian matrix, which describes the curvature of the PES, has all positive eigenvalues.

explicitly modelled by means of a Lennard-Jones (LJ) potential. While the TM method is generally expected to give the most accurate physical description, it has been noted that the method is more sensitive due to the parametrization of the LJ potentials,[35] and considering the many influencing factors (LJ parameters, buffer gas temperature, ...) the simplicity of the PA method leads to a higher transparency of the achieved accuracy, so PA at the moment seems to be favorable in the small-molecule regime where multiple collisions are neglectable.

Finally, it should be noted that the investigation of new algorithms for the prediction of CCS values is still an active field of research and new methods such as the projected superposition approximation (PSA) method[36] are expected to give high accuracy with a minimal runtime cost in the future.

2.2.5 IMS for the differentiation of isomers

Due to the size and shape information provided by the CCS, many types of isomerism may be distinguished via IMS. For example, IM-MS has been used to distinguish peptide isomers.[37] Figure 9 shows several examples of isomers and conformers that exhibit characteristic differences in their CCS value. In general, more compact ions correspond to a smaller CCS.

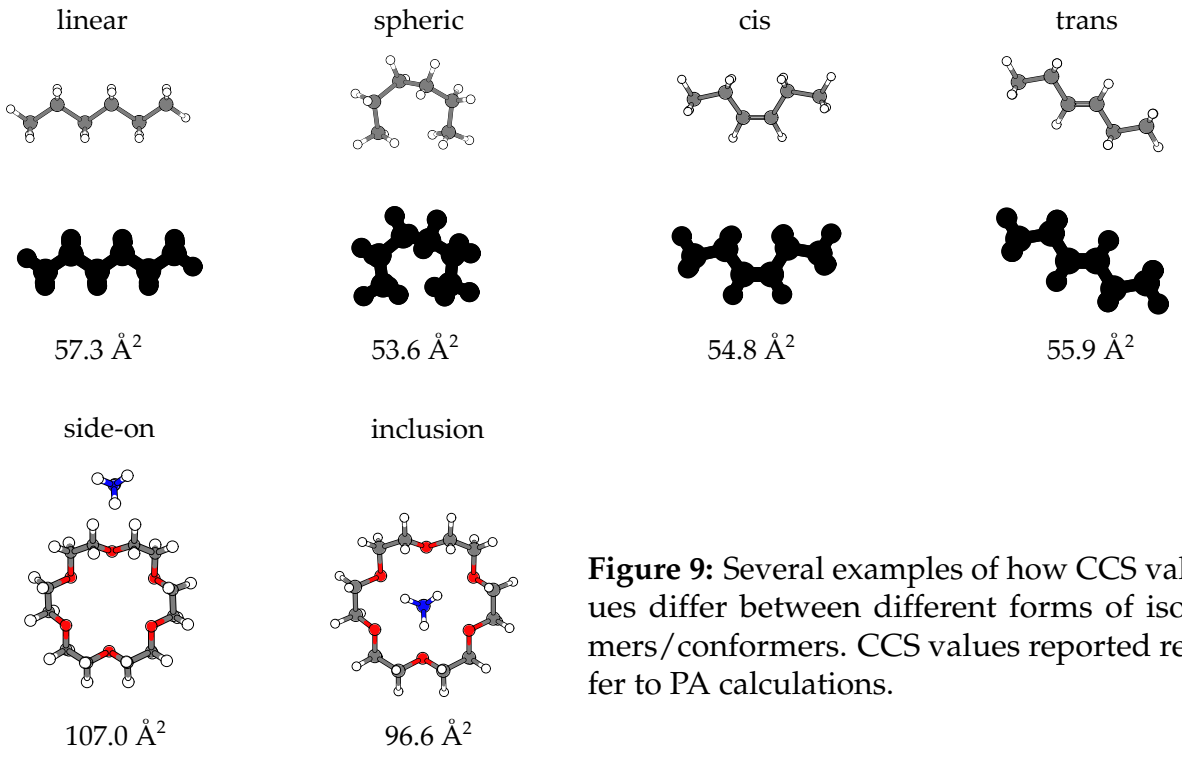

Figure 9: Several examples of how CCS values differ between different forms of isomers/conformers. CCS values reported refer to PA calculations.

2.3 Energy-resolved IMS

In a technique referred to as energy-resolved IMS,[38] ions are activated in the gas phase via collision-induced dissociation prior to entering the drift cell. This way, it was shown that isobaric carbohydrates components with CCS differences as little as 3% could be resolved by their different stabilities. By controlling the supplied activation energy, certain components can be selectively suppressed.[38] In this text, energy-resolved IMS will generally refer to the idea of activating an ion via CID before the IMS cell, and noting the effect of the activation on the ion's drift time or CCS. As shown in Figure 10, the principle of energy-resolved IMS can be used to study the unfolding of the ions in the gas-phase. It should be noted that the ion will increase in size upon unfolding in most cases. However, as the study of the "molecular lasso" in later chapters will show, unfolding can also lead to a more compact structure of the ion.

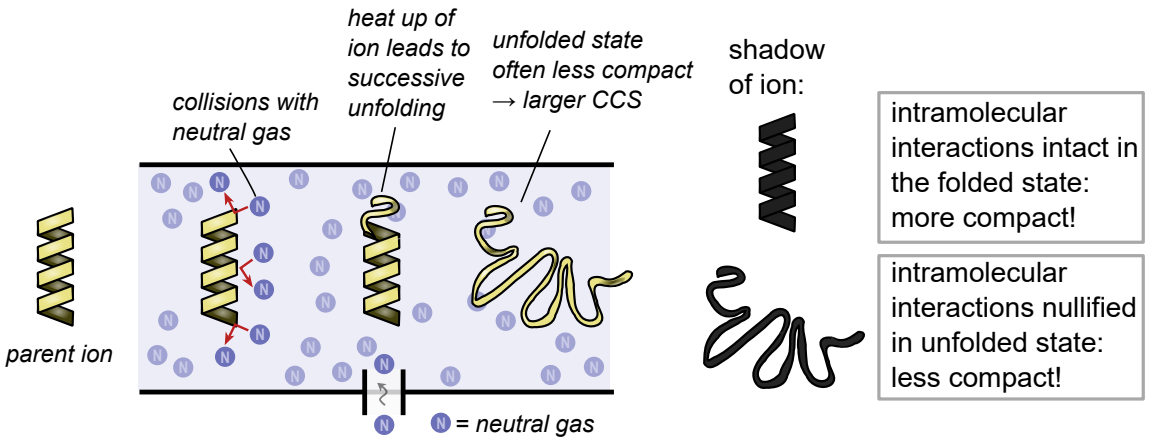

Figure 10: Principle behind energy-resolved IMS folding studies. Activation of the ion induces successive unfolding of the ion. By monitoring the change in the CCS value information about the structure of the ion can be deduced.

2.4 Collision-induced dissociation (CID)

Collision-induced dissociation (CID) is one of the most important methods to fragment ions in the gas phase for the purpose of MS/MS-experiments. CID is assumed to follow a two-step mechanism. The precursor ion, $(A+B)^+$, is activated by the collision with a neutral target gas, N, and subsequently fragments:[39]

$$(A+B)^+ + N \rightarrow (A+B)^{+*} + N \tag{2.11}$$

$$(A+B)^{+*} \rightarrow A^+ + B \tag{2.12}$$

CID processes can be classified into two categories. Low-energy CID occurs in the 1-100 eV range of collision energy and is observed in triple quadrupoles, quadrupole ion traps (QIT) and FT-ICR instruments. High-energy CID happens in the keV range and is seen in sector field and TOF instruments.[39]

2.4.1 Survival yield (SY) method

The survival yield (SY) is a convenient quantitative measure[40–43] to describe the efficiency of fragmentation, and can be linked to the internal energy of the ion.[44] The SY is defined according to[45]

$$SY = \frac{\int I_p}{\int I_p + \sum_{i\in 1\cdots n} \int I_{F,i}}, \tag{2.13}$$

where $\int I_p$ is the integral of the intensity of the parent ion, while $\sum_{i\in 1\cdots n} \int I_{F,i}$ is the sum of the intensity integrals of all n fragment ions. The SY can be well described by a sigmoid function (see Figure 11), given by the expression

$$SY = \frac{a-b}{1+e^{\left(E_{coll}-E_{coll}^{50\%}\right)/d}} + b, \tag{2.14}$$

where a and b are empirical constants with values close to 1 and 0, respectively, while E_{coll} is the collision energy in the laboratory frame, and $E_{coll}^{50\%}$ where the SY is 50%, is also termed the characteristic collision energy (CCE). Finally, d is the width of the steepest part of the sigmoid.[45]

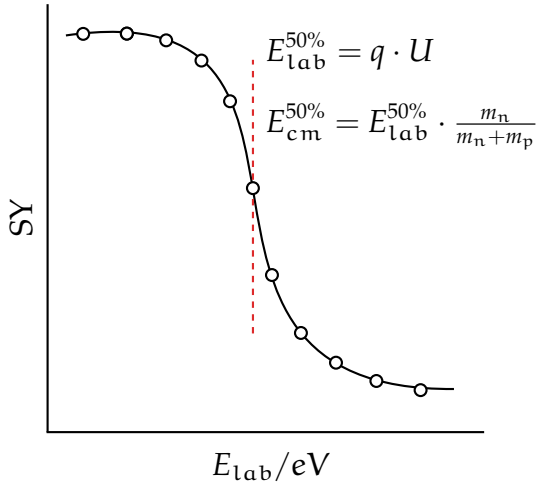

Figure 11: Graphical plot of the SY against the collision energy with equations for determination of the CCE in both laboratory and center of mass frame.

As shown in Figure 11, the applied collision voltage U directly corresponds to the laboratory frame energy via multiplication by the charge q of the ion, thus giving the equation

$$E_{lab}^{50\%} = q \cdot U = e \cdot z \cdot U. \tag{2.15}$$

Similarly, the collision energy in the center-of-mass frame, $E_{cm}^{50\%}$, is obtained via evaluating the equation

$$E_{cm}^{50\%} = E_{lab}^{50\%} \cdot \frac{m_n}{m_n + m_p}, \tag{2.16}$$

where m_n is the mass of the neutral molecule used as the collision gas and m_p is the mass of the parent ion. For a molecule to fragment within the time frame of the CID experiment, it needs to uptake more internal energy than the activation energy for fragmentation to drive the reaction sufficiently fast. This excess energy is called the "kinetic shift" and generally increases together with the available degrees of freedom which are higher for larger molecules.[46,47] Nevertheless, interesting conclusions can be drawn for isobaric species or in other cases—where the internal degrees of freedom are different—by careful comparison with electronic structure methods,[48] or by correcting the kinetic shift either theoretically or experimentally.[49–52]

2.5 Infrared multiphoton dissociation (IRMPD)

Infrared multiphoton dissociation (IRMPD) occurs in two steps. After photoactivation of the precursor ion, $(A+B)^+$, the excited ion subsequently fragments:[53]

$$(A+B)^+ + n \cdot h\nu \rightarrow (A+B)^{+*} \quad (2.17)$$

$$(A+B)^{+*} \rightarrow A^+ + B \quad (2.18)$$

Here, n is the number of photons absorbed and $h\nu$ is the photon energy. After absorption of the IR radiation, the excitation energy is quickly redistributed over all vibrational degrees of freedom, and IRMPD is thus an ergodic process. Photoactivation is achieved by the use of IR lasers. As the energy provided by these lasers is not high enough to initiate dissociation, multiphoton processes are needed to effect dissociation. IRMPD may be used for MS/MS experiments with QIT and FT-ICR mass spectrometers, as these are able to store ions for longer time periods.[53]

2.6 Gas-phase H/D-exchange (GP-HDX)

The common reagents for gas-phase H/D-exchange (GP-HDX) include the basic ND_3, neutrals D_2O and CH_3OD, as well as the acidic DCOOD and CH_3COOD, among several other reagents.[54]

Mechanistically, GP-HDX consists of several steps (see Figure 12A). After the substrate ion (S) and HDX reagent (R) have formed a complex, a proton transfer has to take place, with the direction depending on whether an acid or base is used as the HDX reagent. Subsequent steps are isotope scrambling, transfer of the deuteron and finally dissociation of the deuterated substrate and protonated reagent. Because proton transfers are required, the rate of the HDX depends on the difference in proton affinity (PA) between substrate and reagent.[54]A difference higher than ≈ 85 kJ/mol usually prohibits any HDX. Notable exceptions are amino acids and peptides which have differences in PA as high as 200 kJ/mol and still exhibit HDX in the gas-phase.

To explain the HDX in amino acids and peptides, two different mechanisms have been proposed: The onium (see Figure 12B) and the relay mechanism (see Figure 12C).[55] Basic reagents engage in the onium mechanism, while less basic HDX reagents exchange via the relay mechanism.[54] As detailed mechanistic knowledge about GP-HDX is available, the method developed into a useful tool for probing the structure of ions in the gas-phase across a wide range of functional groups.[56]

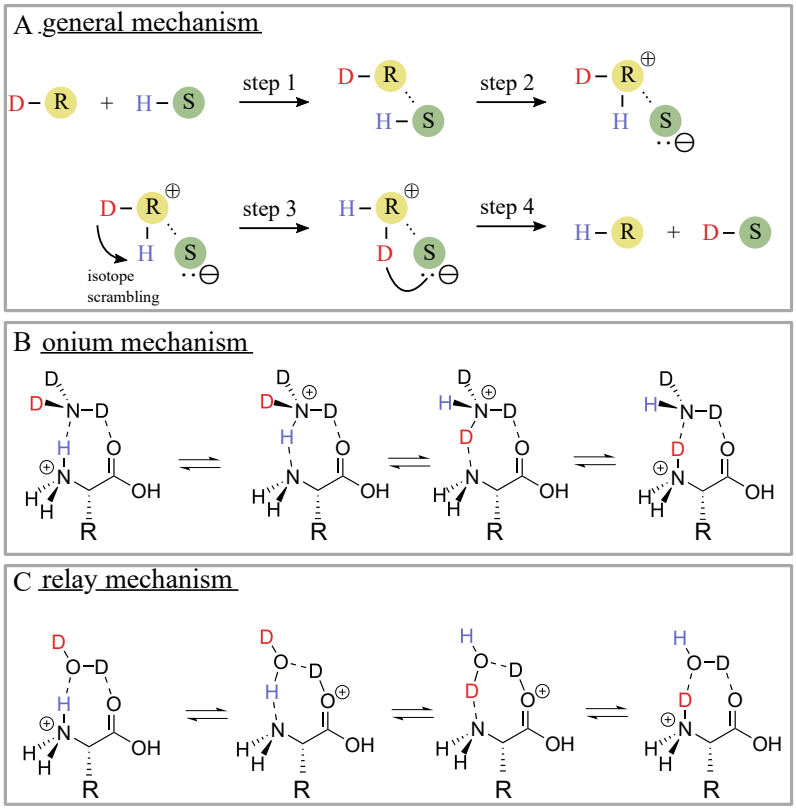

Figure 12: A: General mechanism of GP-HDX. B: Onium mechanism. C: Relay mechanism.

GP-HDX is commonly applied to biomolecules.[54,57–59] The secondary, tertiary and quaternary structure of proteins can be studied.[60] The principle is illustrated in Figure 13. Protons that are buried inside the protein are inaccessible for the HDX reagent and will not exchange. Protons engaged in hydrogen bonding will also exchange slower. Thereby, information about the three-dimensional structure of the biomolecule is obtained.[54,57–59] One study reported a setup for GP-HDX in a travelling wave ion guide for the study of protein conformations.[61]

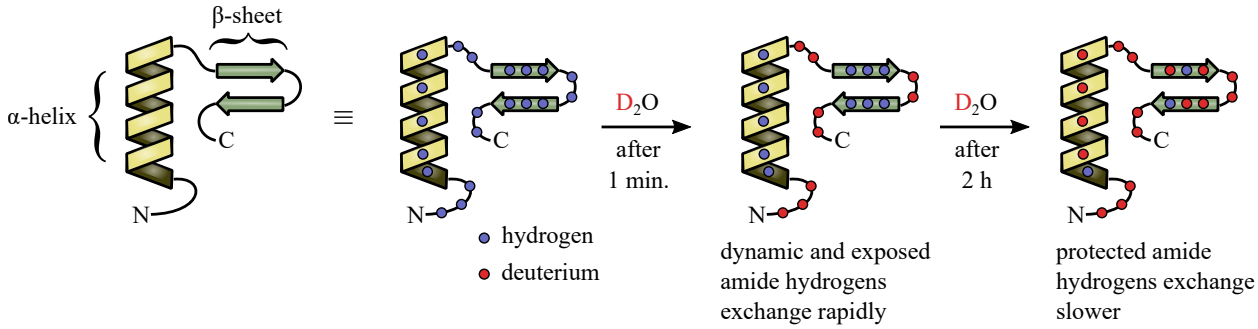

Figure 13: Principle how the secondary, tertiary and quaternary structure of proteins can be elucidated via HDX. Inner protons and protons engaged in hydrogen bonding exchange slower than exposed hydrogens.

As noted before, synthetic supramolecular systems can be seen as mimics of biological systems with deep functional and structural similarities. For example, hydrogen bonding is a pervasive organization principle in natural systems and also used in many synthetic supramolecular systems. Accordingly, detailed insights into the hydrogen bonding of supramolecular systems can be obtained using a similar methodology as in protein conformation studies.

This is nicely illustrated by several earlier studies of Henrik Winkler, including a one-dimensional Grotthuss mechanism in resorcinarene and pyrogallarene capsules,[62] gas-phase organocatalysis,[17] and the dynamic motion of building blocks within ions in the gas-phase.[14,15]

The setup for GP-HDX experiments at our Fourier-transform ion cyclotron resonance (FT-ICR) instrument was described in a recent review.[54]

2.7 Instrumental setup

Travelling-wave ion-mobility mass spectrometry (TW-IMS) measurements were performed with a Waters Synapt G2-S HDMS quadrupole TW-IMS time-of-flight mass spectrometer (Manchester, UK) utilizing an electrospray ionization (ESI) source.[63] The instrumental setup is shown in Figure 14 (top). Take note of the trap- and transfer-cells, that are located before and after the IMS cell, respectively. Because of this flexible setup, it is possible to either excite drift-time selected components (activation in transfer cell), or to examine the influence of collisional activation on the size and shape of the ion (activation in trap cell). GP-HDX experiments were performed using the Varian IonSpec QFT-7-FT-ICR-MS, shown in Figure 14 (bottom).[54]

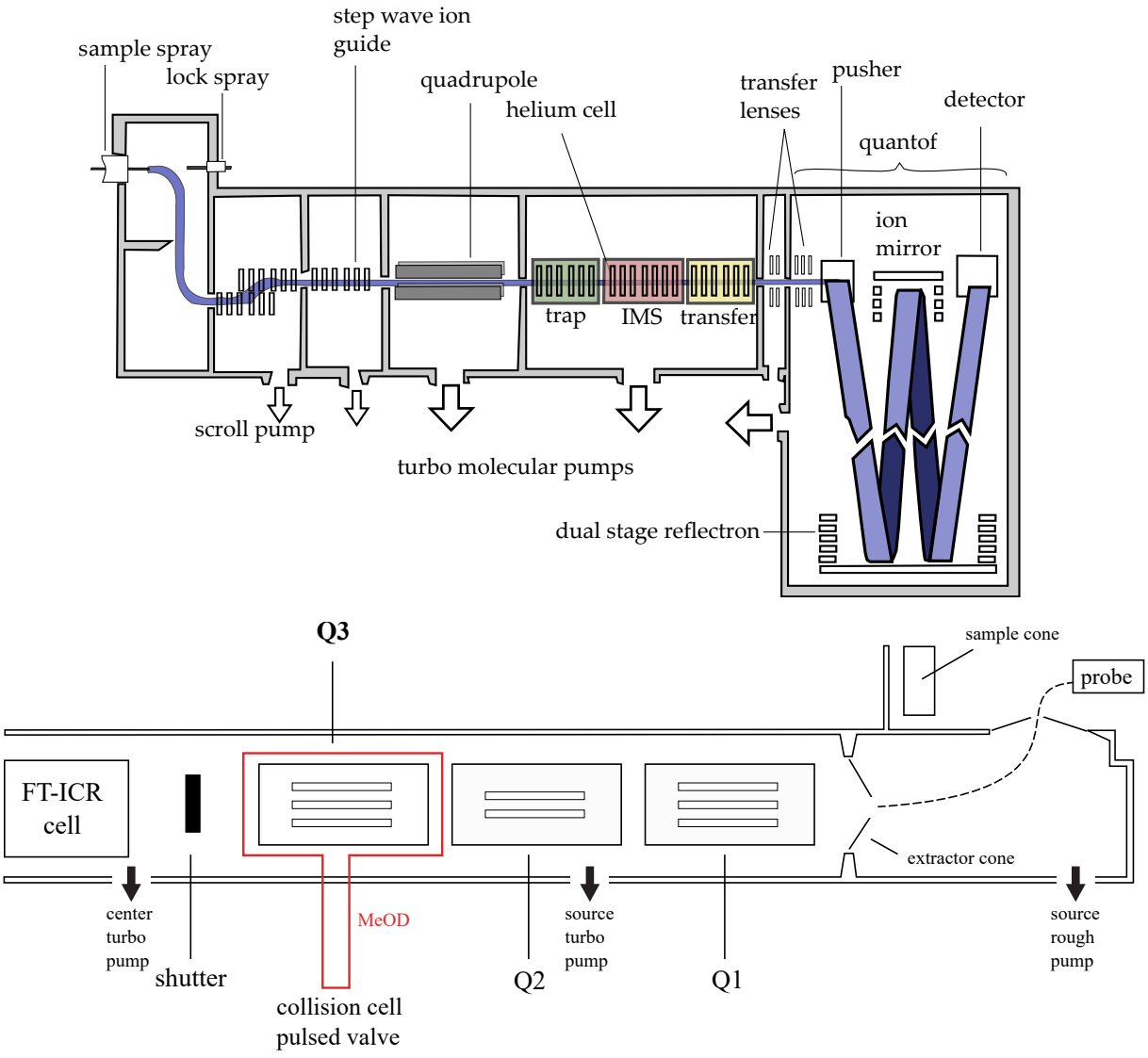

Figure 14: Top: Instrumental setup of the Waters Synapt G2-S HDMS TW-IMS time-of-flight mass spectrometer. Redrawn by the author from the description given in the instrument manual.[64] Bottom: Instrumental setup of the Varian IonSpec QFT-7-FT-ICR-MS instrument used for gas-phase H/D-exchange reactions.

2.8 DFT in gas-phase supramolecular chemistry

The work presented here has been complemented with electronic structure calculations. Mostly, the density functionals B3LYP, M06-2X and the semiempirical methods AM1 and PM3 have been employed to obtain suitable molecular structures for CCS calculations. In this section, the theoretical background of density functional theory (DFT) and how it relates to other electronic structure methods is briefly presented.

Generally, *ab initio* electronic structure methods base their description of electronic systems on fundamental theoretical principles, such as the electronic Schrödinger equation[65]

$$\hat{H}\Psi = E\Psi. \tag{2.19}$$

Here, Ψ is the electronic wave function, E is the exact electronic energy and $\hat{H}$ is the non-relativistic electronic Hamiltonian in the Born-Oppenheimer approximation. As a direct solution is computationally not feasible, suitable approximations are used to reduce the computational complexity of the problem. In the Hartree-Fock (HF) method, the electronic wave function Ψ is approximated by a single Slater determinant[66,67]

$$\Psi = ||\psi_1 \cdot \psi_2 \cdots \psi_n||, \tag{2.20}$$

where the spatial part of the spin orbitals are expanded as a linear combination of gaussian-type basis functions ϕ_j of the form

$$\psi_i^{\text{spatial}} = \sum_j c_{ij} \cdot \phi_j \tag{2.21}$$

with suitable expansion coefficients c_{ij}.[66,67] This means that electron correlation—the instantaneous interaction between different electrons in the system—is neglected. Therefore, even if a complete basis set was employed, the obtained energy, the so called HF limit, would still lie higher than the exact solution. This difference between the HF limit and the exact energy is called the correlation energy of the system.[68] The fundamental cause of this energy is the repulsive electron-electron interaction that occurs if two electrons occupy a nearby space and is not treated in the effective HF potential. To remedy these shortcomings, a frequently applied electronic structure method—that relies on its own theoretical foundations—is density functional theory (DFT). In DFT, it

is assumed that all properties of the system can be expressed in terms of the electron density $\rho(\vec{r})$. While the electronic wavefunction depends on the x-,y-, and z-coordinate of all n electrons—$3n$ coordinates in total—the electron density $\rho(\vec{r})$ can be expressed in terms of the three coordinates $\vec{r} = x, y, z$ in space, only. So by formulating the problem in terms of the electron density, a large reduce in the computational cost is achieved.[68] In 1964, the Hohenberg-Kohn theorems were first formulated,[69] that would later form the foundation of DFT, as it is known today. Briefly, the Hohenberg-Kohn existence theorem states that there exists a unique functional E such that

$$E\left[\rho(\vec{r})\right] = E_{\text{elec}}. \tag{2.22}$$

Here, E_{elec} is the exact electronic ground state energy of the system. Furthermore, Hohenberg and Kohn showed that the electron density obeys the variational principle, meaning that the exact electronic ground state energy is the global minimum.[70] Both the existence and variational Hohenberg-Kohn theorems together constitute the theoretical foundation of DFT.[70]

While a function can be seen as a map from one scalar to another scalar value, a functional maps a function to a scalar quantity. Here, the function $\rho(\vec{r})$ depends on the spatial coordinates $\vec{r}$, while the energy E is a functional of the density $\rho(\vec{r})$. Kohn and Sham postulated that the functional can be expressed in the general form[68]

$$E\left[\rho(\vec{r})\right] = T_e\left[\rho(\vec{r})\right] + V_{ne}\left[\rho(\vec{r})\right] + V_{ee}\left[\rho(\vec{r})\right] + E_{xc}\left[\rho(\vec{r})\right], \tag{2.23}$$

where T_e is the kinetic energy of the non-interacting electrons, V_{ne} is the nuclear-electron attraction, while V_{ee} is the classical part of the electron-electron repulsion. The last term E_{xc} is the exchange-correlation functional that takes all other aspects of the real system into account. Then, in the Kohn-Sham procedure, it is solved for the orbitals χ_i, from fictional non-interacting partials, that minimize the energy by solving the pseudo-eigenvalue equations

$$\hat{h}_i^{KS}\chi_i = E_i\chi_i, \tag{2.24}$$

in a fashion very similar to the Hartree-Fock-Rothaan-Hall method.[67] Here $\hat{h}_i^{KS}$ is a single-particle Hamiltonian, and we express the density in terms of the fictional orbitals as[71]

$$\rho(\vec{r}) = \sum_i (\chi_i)^2. \tag{2.25}$$

The key point is that for a similar computational cost as HF, the energy obtained in DFT includes electron correlation.[68] In principle, DFT could give the exact ground state energy if the exchange correlation term was known. However, as the exact form of the functional E_{xc} remains unknown, a multitude of different approximations have been suggested. These can be seen as climbing a ladder on the accuracy scale, as illustrated in Figure 15.[72,73] Beginning with local density (LDA), the accuracy can be systematically improved reaching near chemical accuracy (± 1 kcal/mol).[72–74] For the exchange term, Becke's method is often employed.[75] For the correlation term, a functional by Lee, Yang and Parr is often used.[76] Hence the acronym BLYP is used. Besides pure DFT methods (BLYP, VWN), hybrid-DFT methods are used (B3PW91, mpW1k), where a mixing with HF is included. For organic systems, one of the most popular is the B3LYP hybrid functional. This includes the Becke exchange and the LYP correlation functional and is of the form[77,78]

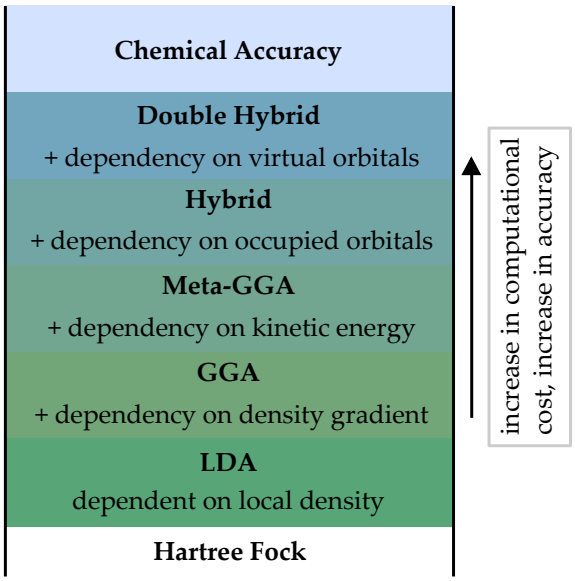

Figure 15: Illustration of the accuracy achieved with different methods of DFT.

$$E_{xc}^{B3LYP} = (1-a)E_x^{LSDA} + aE_x^{HF} + b\Delta E_x^{B} + (1-c)E_c^{LSDA} + cE_c^{LYP}, \tag{2.26}$$

where LSDA is the acronym for local spin density approximation. The three coefficients a, b, c are responsible for the naming of this functional, and are fitted to empirical data. A relatively recent development are the meta hybrid functionals that include terms depending on the kinetic energy density and HF exchange.[77] One popular meta hybrid functional is M06-2X developed by Y. Zhao and D. G. Truhlar.[79] M06-2X shows

Table 2: Overview over DFT studies/benchmarks on different types of non-covalent interactions. A general overview can be found in [80].

type of interaction	set size	refs
crown-ether alkali cation complexation	5	[81]
crown-ether ammonium complexation	>10	[82],[83]
dispersion	10	[84],[85]
dispersion in hydrocarbons	12	[86]
dispersion in heavy-atom hydrides	28	[87]
hydrogen bonds	66	[84],[88]
halogen, chalcogen and pnictogenbonds	30	[89]
charge transfer	11	[90],[91]

a high performance in benchmarks of thermodynamical properties (dissociation energies, ionization energies, electron and proton affinities, ...), as well as π-systems and non-covalent interactions.[79,92] Hence, M06-2X is a promising functional for use in supramolecular chemistry and in particular in the prediction of ground state geometries for CCS calculations. A similar accuracy is achieved with the TPSS/TPSSh (hybrid) meta-GGA functional,[93] for which state of the art accuracy has been reported in the reproduction of the thermochemistry of crown ether ammonium complexes.[82]

The treatment of non-covalent interactions with DFT may even approach chemical accuracy provided that the right functionals and a sufficiently large basis set is used. The Minnesota functionals already treat dispersion from the parametrization step of the functional.[94] In other density functionals a dispersion correction, such as Grimme's D3 model,[87] should be employed.[95,96] Table 2 gives an overview of benchmarks for different types of non-covalent interactions. Further information on the theoretical treatment of non-covalent interactions with DFT can be found in the provided references.

For the computationally assisted interpretation of mass spectra, very large databases have been collected for electron ionization (EI),[97,98] out of which common fragmentation pathways could be deduced.[99,100] This allows the operator to interpret EI spectra by database look-ups as well as rule-based spectra simulation.[101,102] For collision-induced dissociation (CID), the amount of data available is comparably small. One reason is the influence of many parameters on the final spectrum, so that it is difficult to compare

CID spectra between instruments and even laboratories.[97,103] Even though a standardization of CID that supports database comparisons was proposed,[104] and common fragmentation pathways of some compound classes have been identified,[105–108] there is still no unified way for the computer-assisted interpretation of CID spectra.[108]

As of today, the only computational assistance available to the CID operator are electronic structure calculations that can be used in different ways to predict fragmentation pathways.[97]

DFT was applied to rationalize spectra of peptides and proteins.[109,110] In the field of small molecules, the references are comparibly scarce. Characteristic losses of ammonia, water, and carbon monoxide from aromatic molecules with amino, hydroxyl, and carboxyl groups have been identified by DFT.[111] In particular, the rate-limiting step for these losses under CID conditions were calculated so that conclusions about the reaction mechanism of these neutral losses could be drawn.[111] Similarly, DFT was used to explain carbon monoxide losses in the proton adducts of five-membered lactons.[112] The important observation common to all these DFT studies is that the protonation site directs the subsequent fragmentation in its proximity.[97] The bond length changes induced by protonation were directly linked to the observed fragments, for which both DFT and semiempirical methods may be used.[113,114]

Recently, an important step towards the fully-automated prediction of EI spectra has been realized.[115,116] While the fragmentation mechanisms of EI differ from CID, there remains the hope that a fully automated prediction of CID spectra can be realized in the near future, maybe even including rule-based approaches that do not rely on comprehensive databases.[108] A software-assisted CID spectra simulation would need to address both kinetic and thermodynamic aspects in the implementation of the prediction algorithm.[97]

Similar questions as discussed above for CID also arise in the computational assistance of IM-MS data. In particular, the automated prediction of CCS values of a given analyte would be highly desirable from a practical viewpoint.

At the moment, explicit modelling of the molecule with a suitable electronic structure method is still necessary. The obtained ground state geometry is then used as input to the CCS prediction routine.

DFT was used for the interpretation of IM-MS studies for diverse systems including

catechin epimers,[117] Tröger bases,[118] host/guest complexes,[119,120] protonated water clusters,[121] tripeptides,[35] and even 20-residue peptides.[122] Alternatively, semiempirical calculations have been employed including the coordination chemistry of terpyridines,[123] chiral hexaimine macrocycles,[124] and oligorotaxanes.[125] The theoretical underpinnings of these semiempirical procedures are the topic of the next section.

2.8.1 Semiempirical calculations

While DFT is the method of choice for many questions of modern computational chemistry, it's scaling of $\mathcal{O}(n^3)$, where n is the number of electrons of the system, still imposes restrictions on the system size.[126] Although better scaling DFT methods are currently in development,[127] semiempirical methods still remain a choice for the qualitative treatment of very large organic systems.

Semiempirical methods are based on a similar theoretical foundation as HF, but use a minimal basis set and approximate or completely neglect terms such as inner electrons or the two electron integral. To correct for the errors introduced by these approximations, parameters are introduced that are fitted either to experimental data or *ab initio* methods. The big advantage is the low computational cost and the resulting short runtime of semiempirical calculations. However, the obtained results are only representative when the treated system is covered by the parametrization of the method.[128]

Most semiempirical methods are based on the *modified neglect of differential overlap* (MNDO).[129] Here, the two electron integral of each atom type is fitted with respect to empirical properties such as enthalpy of formation, geometry, dipole moment or first ionization energy. In *zero differential overlap* (ZDO), all products of basis functions that locate the same electron at different atoms are neglected.[130]

The *Austin Model 1* (AM1) developed by M. J. S. Dewar is based on MNDO but employes a modified expression for the nuclei-nuclei repulsion term.[131] This modified expression includes a (physically incorrect) attractive interaction between nuclei to simulate van der Waals forces. An advantage of AM1 is that hydrogen bonding is treated to some extend and that enthalpies of formation are more accurate than in MNDO.[130]

James Stewart developed the Parametric Model 3 (PM3) which uses a Hamiltonian that is very similar to AM1, but bases the parametrization on a broader number of molecular properties.[132] This difference in parametrization allows PM3 to treat hydrogen bonds comparably well, although inter- and intramolecular interactions are still exaggerated in some cases (e.g. the hydroxyl group in 1-pentanol is strongly attracted to the terminal methyl group).[130]

Despite these caveats, there is an ample amount of reference studies on the use of semiempirical methods in mass spectrometry to guide new investigations.[114,116,133–137]

3
CHAPTER

Summarized Results

This chapter summarizes the main results of my thesis, which have been published in five peer-reviewed papers, including collaborations with the groups of Markus Albrecht from RWTH Aachen, Kari Rissanen from University of Jyvaskala, Beate Paulus and Biprajit Sarkar from Freie Universität Berlin.

The aim of my dissertation project was the study of supramolecular complexes with advanced mass spectrometric techniques. Throughout the five studies reported here, the two major aspects are the differentiation of different types of isomers and the investigation of intramolecular forces (as illustrated in Table 3).

Table 3: Overview over the five main projects of my dissertation, and the different types of isomerism and interactions investigated.

Study	Isomerism/Structural Aspect	Interaction
1. chiral recognition	diastereomers/enantiomers	hydrogen bonding
2. azobenzene photo-isomerization	(*E*)/(*Z*)-photoisomers	hydrogen bonding
3. molecular lasso	mechanoisomers	crown-ether ammonium complexation / hydrogen bonding, TTF^{n+}/NH_3R^+-charge repulsion
4. oligorotaxane	conformers/mechanoisomers	crown-ether ammonium complexation, TTF^{n+}/TTF^{n+}-charge repulsion
5. titanium helicates	monomer/dimer-equilibrium	dispersive interactions, solvent effects

To gain the necessary structural details needed to identify isomers or underlying intramolecular/intermolecular non-covalent interactions, I employed a combination of several mass spectrometric techniques, as shown in Table 4. All three methods can be used to investigate both isomerism and underlying non-covalent interactions.

Table 4: Overview of how modern mass spectrometric methods can reveal information about isomerism and non-covalent interactions.

Method	Isomerism	Interaction
Ion mobility-mass spectrometry (IM-MS)	differences in drift time/CCS	TTF^{n+}/TTF^{n+}-charge repulsion increases CCS, stronger hydrogen bonding may affect CCS
Collision induced dissociation (CID)	differences in stability and fragmentation pathways	stronger hydrogen bonding increases stability of ion
Gas-phase H/D exchange (GP-HDX)	differences in exchange rate and number of exchangeable protons	hydrogen bonding influences exchange rate, strong hydrogen bonding may completely inhibit any GP-HDX

In my initial first-author study,[138] chiral BINOL-based crown-ether ammonium complexes were investigated. Chirality plays a fundamental role throughout chemistry, biology, and pharmaceutics, as the three major building materials of life— proteins, nucleic acids, and polysaccharides— are based on chiral monomers so that recognition events in living organisms always occur in an intrinsically chiral environment. Hence, two enantiomers of the same drug can display vastly different pharmacological effects. Thalidomide (Contergan) is the most prominent example, where the (*R*)-enantiomer has the desired anti-nausea effect, while the (*S*)-enantiomer is teratogenic, although quick *in vivo* racemization is possible.[139] Still, in the past decades, thalidomide has undergone a remarkable comeback from a dreadful drug inducing birth defects (due to its quick *in vivo* racemization) into an effective therapy for treating leprosy and multiple myeloma.[140]

While plain mass spectrometry in itself cannot distinguish enantiomers as they have the same m/z-ratio (isobaric), several approaches have been suggested to implement enantioseparation in MS by the formation of diastereomeric non-covalent complexes. In a seminal publication by Sawada,[141] it was established that enantioselectivity can be

achieved in fast atom bombardment (FAB)-MS by the relative peak intensity method on diastereomeric non-covalent complexes. This approach was extended towards gas-phase reactions of cyclodextrin complexes.[142] Another important example is Cooks' kinetic method, which is based on the collision-induced dissociation (CID) of copper/amino acid complexes, among several other systems.[143–148] Another approach towards gas-phase enantiodifferentiation is a modification of classical ion mobility-mass spectrometry (IM-MS). As shown in Figure 16 (**I**A), neither mass spectrometry nor plain IM-MS differentiate between enantiomeric ions. The underlying reason being that both experiments are inherently achiral, so that no enantioseparation can be achieved. However, addition of (*S*)-2-butanol to the buffer gas affords a chiral medium (see Figure 16 (**II**A)), that differentiates between enantiomeric ions by drift time (Figure 16 (**II**C)).[149] Another strategy again relies on non-covalent complex formation between both enantiomeric ions and a chiral host molecule H*: After formation of diastereomeric complexes $G_{(R)} \subset H^*$ and $G_{(S)} \subset H^*$, both diastereomeric ions are physically different and therefore also correspond to different drift times.

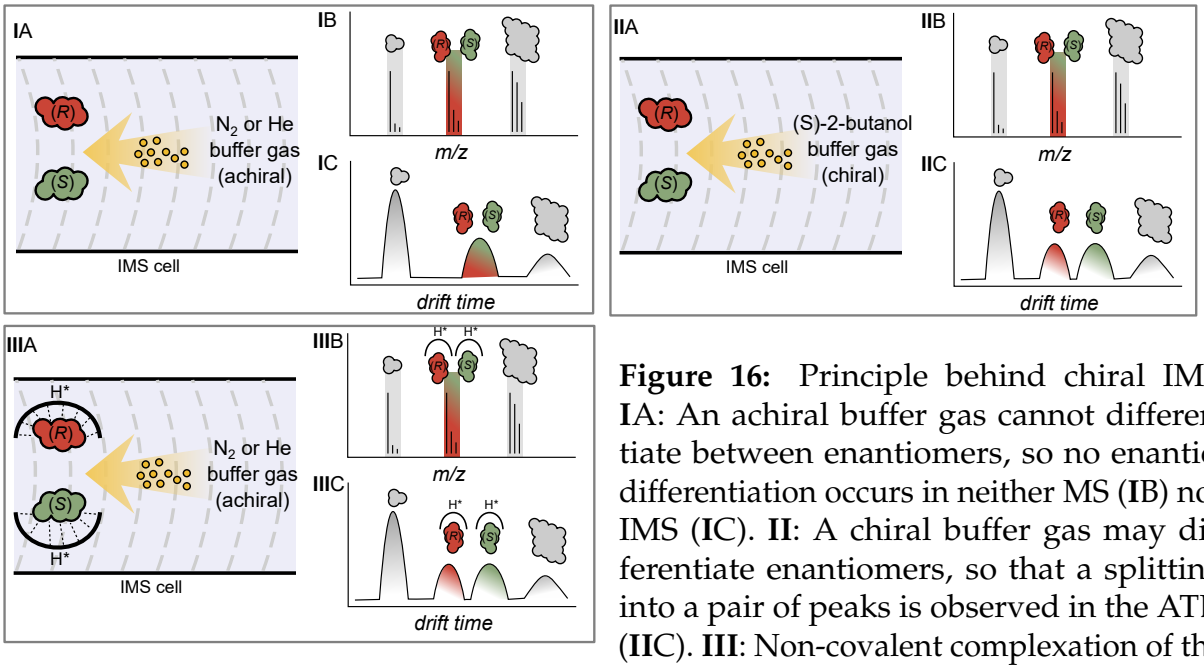

Figure 16: Principle behind chiral IMS. **I**A: An achiral buffer gas cannot differentiate between enantiomers, so no enantiodifferentiation occurs in neither MS (**I**B) nor IMS (**I**C). **II**: A chiral buffer gas may differentiate enantiomers, so that a splitting into a pair of peaks is observed in the ATD (**II**C). **III**: Non-covalent complexation of the analyte enantiomers with a chiral host H* will lead to diastereomeric complexes, that are physically different and hence appear as separate features in the ATD (**III**C).

Three different scenarios of G* ⊂ H* are possible: 1) The size difference between both complexes is too small to be resolved at all, and a single feature is observed in the ATD. 2) The size difference is large enough to baseline-separate both ions, in which case both diastereomers are clearly identified, and may also be quantified directly via peak integration (after prior calibration with reference standards).

3) The size difference is too small to allow for baseline resolution of both features, but is still detectable. In this case, a single peak will be observed in the ATD, of which the centroid will experience an *ee*-dependent shift.[§] This special scenario is depicted in Figure 17. It turns out that there is a direct linear map between the centroid drift times of the gaussian peaks and the enantiomeric composition of the sample. Hence, the *ee* can be directly obtained from the centroid drift time after prior calibration. The centroid of a peak in an ATD is obtained via the weighted sum

$$\sum_{i} A_i \cdot t_{d,i} \,,$$

where i is the bin index, A denotes the abundance (i.e. ion count) at bin i, $t_{d,i}$ denotes the drift time of bin i. What makes this approach especially interesting is the fact that potentially very small structural differences can be studied of a mass-selected component contained in a complex multi-component mixture.

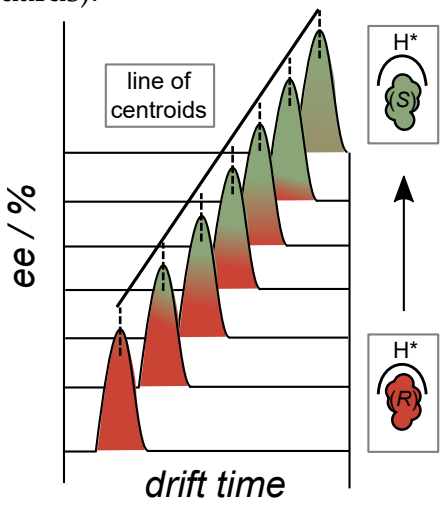

Figure 17: Graphical illustration of the systematic drift time shifts observed for small size differences between diastereomeric host/guest complexes. In these cases, the centroids of the gaussian peaks will gradually shift between the drift time values of clean enantiomers, such that there is a direct linear mapping between the centroid drift time and the enantiomeric composition, as for example expressed in terms of the *ee*.

To test this approach in practice, I designed a TW-IMS study of crown-ether ammonium complexes.

[§] Where $ee = \left|\frac{[R]-[S]}{[R]+[S]}\right|$, where $[R]$, $[S]$ is the concentration of the two enantiomers, respectively.

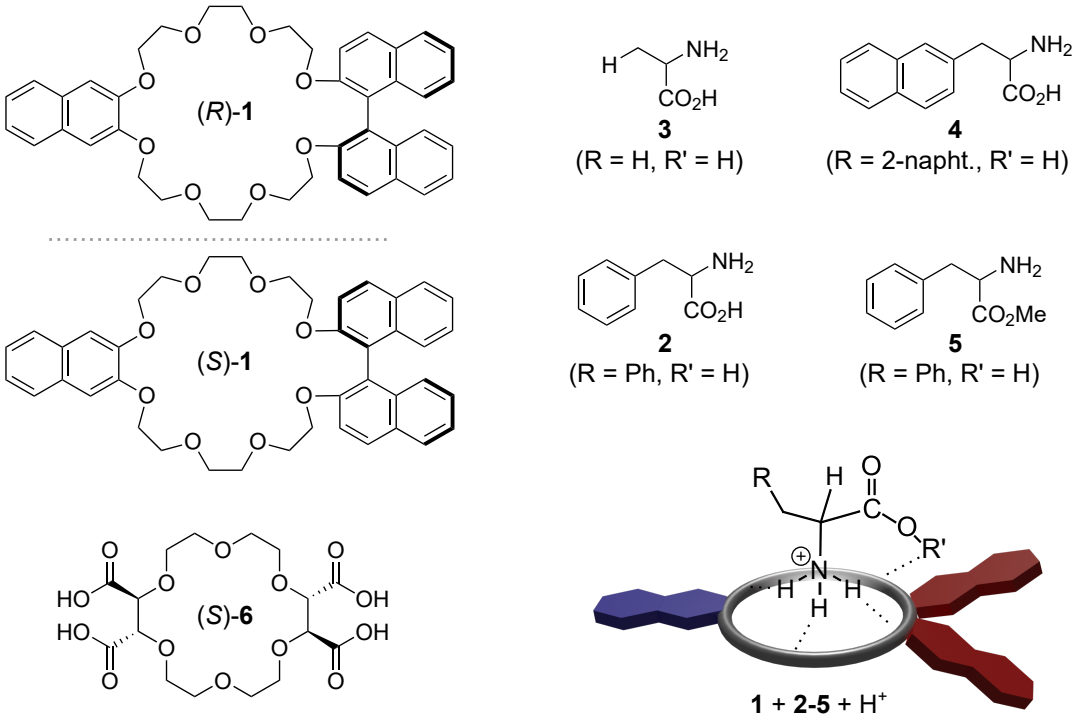

Figure 18: Overview of the two BINOL based 24-crown-7 ethers (*R*)/(*S*)-**1** and tetracarboxyl-18-crown-8-ether (*S*)-**6**, and differently substituted amino acids **2-5**.[138]

As shown in Figure 18, this study examined two BINOL based 24-crown-7-ethers (*R*)/(*S*)-**1**, as well as 18-crown-6-ether (*S*)-**6** as hosts, and differently substituted amino acids **2-5** as guests.

Table 5 shows the collision cross section values measured for each of these crown-ether/ammonium complexes. A clear observation is that the homochiral complexes (e.g. (*R*)-**2**+(*R*)-**1**) exhibit smaller CCS values than the corresponding heterochiral complexes (e.g. (*S*)-**2**+(*R*)-**1**). Furthermore, the CCS difference between homo- and heterochiral complexes, $\Delta\Omega$, successively increases with a bigger substituent size and can be understood by considering that larger substituents will also induce larger size differences geometry-wise. However, for the large substituent in guest **5**, the CCS difference is comparably small.

Table 5: Overview of CCS values of homochiral and heterochiral complexes of **1** with differently substituted guests. Both small substituents and removal of the COOH hydrogen donor group lead to a drop in the CCS difference.

Guest	$\Omega_{homochiral}/Å^2$	$\Omega_{heterochiral}/Å^2$	$\Delta\Omega/Å^2$
2	205.0	205.8	0.8 ± 0.1
3	194.4	194.7	0.3 ± 0.2
4	215.2	216.7	1.5 ± 0.1
5	211.4	211.7	0.3 ± 0.2

In the study, it is shown that the reason for this phenomenon—that methyl esterification drastically lowers $\Delta\Omega$ in comparison to the free carboxyl group—lies in the hydrogen bonding between the crown ether host and the free carboxyl group in the guest. Gas-phase H/D-exchange (GP-HDX) experiments were performed, that further support the existence of hydrogen bonding of the carboxyl group to the crown ether host.

Seeing the tremendous success of amino acids in mass spectrometry-chiral recognition studies,[150] the observation that the free carboxyl group seems to have a strong influence on the enantiodifferation is very interesting. Indeed, while a vast amount of research has been performed on chiral recognition in the gas phase,[151,152] an understanding of the exact interactions responsible for the recognition often remains elusive. As such, seeing that both targeted methyl esterification and gas-phase H/D-exchange reveal the influence of a single hydrogen bond on the enantiodifferentiation provides a new handle on understanding the molecular forces underpinning gas-phase chiral recognition.

Finally, the question was addressed if the phenomenon of gradually shifting centroids illustrated in Figure 17 could be used for *ee* quantification. The best results for this method of *ee* quantification were obtained with tetracarboxyl-18-crown-6-ether **6**. As shown in Figure 19, the small shift of the centroid drift time (left) can indeed be directly linearly correlated to the *ee* of the sample ($R^2 > 0.986$). So the study nicely illustrates that not only non-covalent interactions can be unveiled, but that the accuracy of *ee*-quantification is already at a practically useful level: even small structural differences can be reliably investigated with the "centroid method".

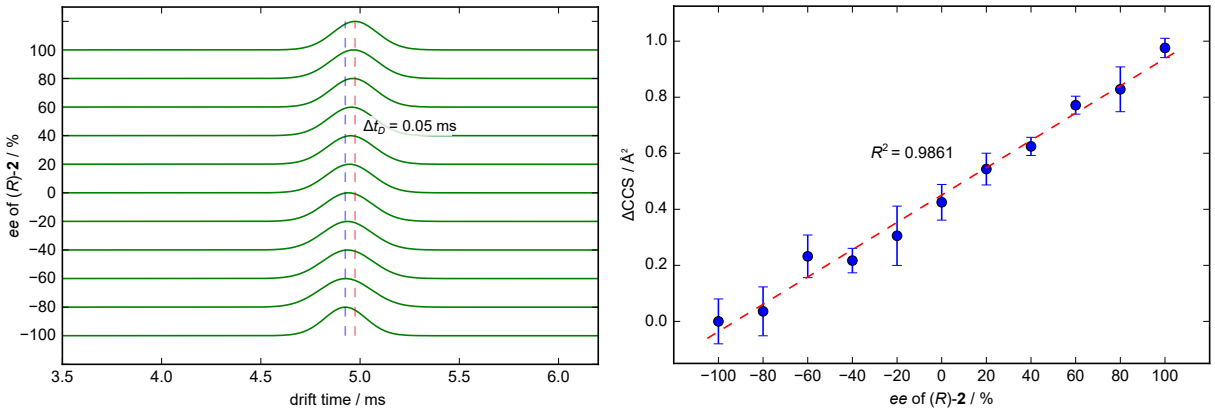

Figure 19: Systematic change in drift time (left) observed for complexes of (*S*)-18-crown-6-tetracarboxylic acid **6** and varying enantiomeric composition of a (*R*)/(*S*)-**2** mixture, and *ee* quantification (right). Errors correspond to five measurements and two standard deviations.[138]

In my second first-author publication,[153] I studied the photoisomerization of a 4,4'-diamido-azobenzene model system. The photoisomerization of azobenzene functionalized materials has a rich history as a versatile tool to drive controlled molecular motion,[154–156] thereby providing exciting opportunities for dynamically responsive molecular systems and materials.[157–160] However, connected with this increased interest in the synthesis and potential applications of photoswitches, there is also a need for the development of new analytical methods to reveal photoresponsive molecular behavior.

Naturally, the question arised if the approach for seeing small structural differences of the first study could be extended towards other systems. So the second study illustrates how TW-IMS can provide valuable insights into the dynamic behavior of azobenzene photoswitches, but also highlights the current limitations.

As in the case of enantiomers considered in the first study, mass spectrometry cannot differentiate between different photoisomers, as the isomeric ions have the same sum formula and are thus *isobaric* (having the same mass). However, due to the additional size information offered by IMS (see Figure 20A), it is possible to distinguish isomers by IM-MS. As discussed in section 2.2.5, it would generally be expected that *cis*-isomers are more compact than the corresponding *trans*-geometry.

A recent DT-IMS study[161] reported that (*E*)- and (*Z*)-isomers of an azobenzene functionalized dendritic bolaamphiphile could only be differentiated by IMS in the disodium adduct $M+2Na^{\oplus}$. In case of the protonated ion, the photoisomers could not be resolved and only a single feature was observed in the ATD.

In agreement with earlier IMS studies on photoisomerization,[123,161–163] we propose the following explanation: Protonation of the azo group reduces the barrier of rotation around the N=N bond, leading to a quick thermal backrelaxation $(Z)\rightarrow(E)$, as illustrated in Figure 20B. In consequence, only the thermodynamically favored (*E*)-isomer is observed in the ATD. In an attempt to test this hypothesis, the author devised three azobenzene model systems **1**-**3** (see Figure 20C), of which only **1** features a basic group at the side chains, while **2** and **3** are protonated at the central azo group (see Figure 20C). Thus, if the mechanism of thermal backrelaxation proposed in Figure 20B is indeed correct, it would be expected that resolution of the photoisomers is only possible for **1**, while **2** and **3** would yield a single feature in the IMS experiment.

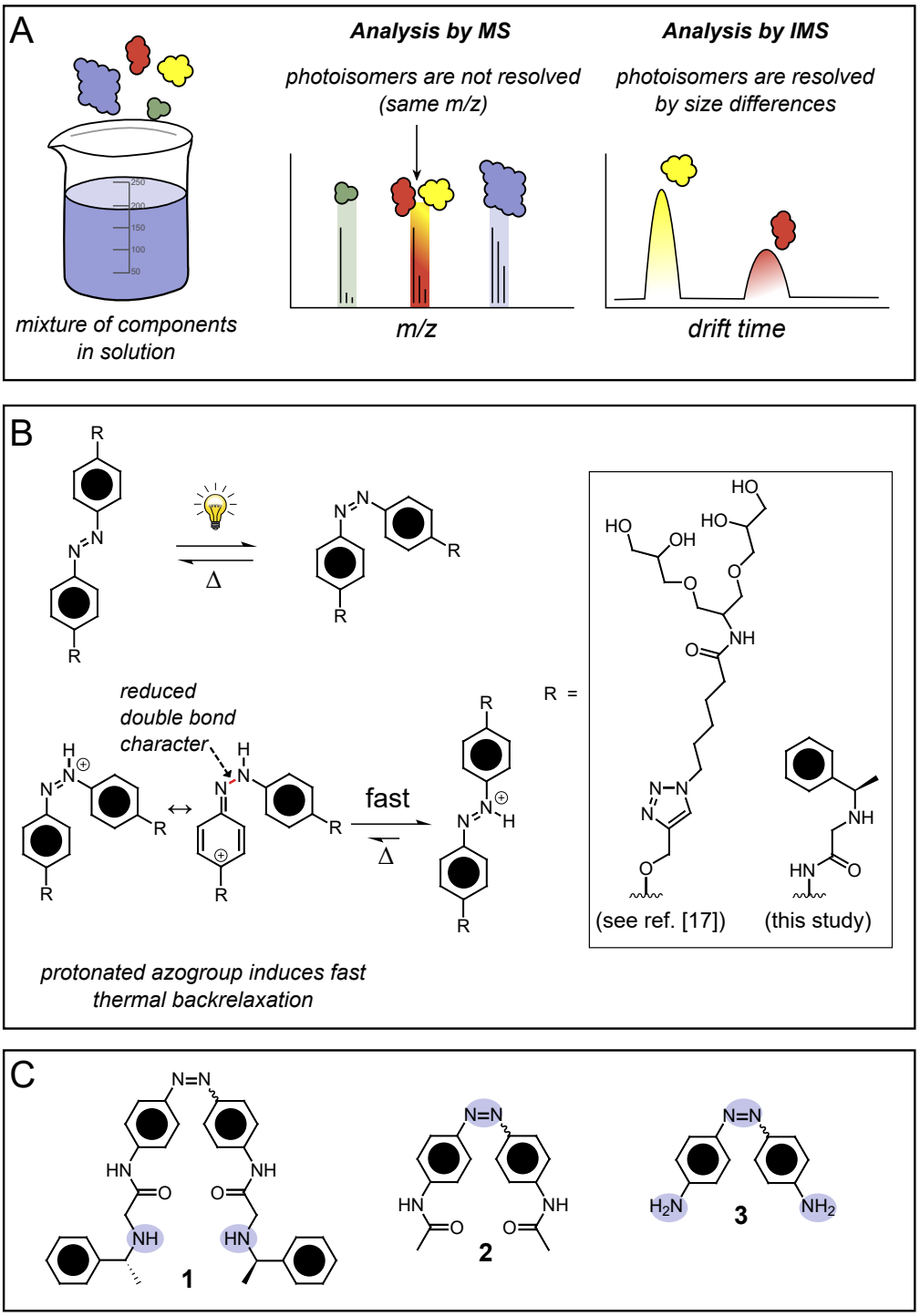

Figure 20: A: While classical mass spectrometry cannot differentiate between differently shaped ions, photoisomers can be directly distinguished by differences in the drift time in the IMS experiment. B: Proposed mechanism of fast thermal relaxation in azobenzenes upon protonation of the azo group. C: To test this hypothesis, a diamidoazobenzene model system **1** was developed. The secondary amine group provides a site for stable charge formation, thus preventing the protonation of the azogroup. Additional control experiments were performed on systems **2** and **3**, as protonation here occurs preferentially at the azobenzene group. Copyright Wiley-VCH Verlag GmbH & Co. KGaA. Reproduced with permission.[153]

The UV-VIS spectrum of **1** features the typical optical transitions observed for diamido azobenzenes.[164,165] Furthermore, the thermal relaxation half life of $t_{1/2} \approx 540$ min. was found to be suitable for IMS analysis. To ascertain that the protonation occurs at the amino moiety, collision-induced dissociation (CID) experiments were performed, as described in section 2.4. Bond cleavages adjacent to the ammonium groups explain the formation of all fragments with major intensity. Most prominently, formation of neutral styrene and primary ammonium ions is observed via 1,2-elimination.

By use of the survival yield (SY) method, the gas phase stability of an ion is determined in terms of the characteristic collision energy (CCE). Further details of this method are described in section 2.4.1. By the SY method (see Figure 21), (*Z*)-**1** was found to be $\Delta V \approx 1.5$ V more stable than (*E*)-**1**. This is surprising, as the stability trend in solution is reversed. The enthalpy of isomerization for plain azobenzene was found to be $\Delta H_{isom.}\big((Z) \rightarrow (E)\big) = -(49 \pm 1)$ kJ/mol by reaction-solution calorimetry,[166] so, at first glance, a similar situation would be expected for the gas-phase as well. To rationalize this surprising finding, we postulated a proton-bridged hydrogen bond in (*Z*)-**1**. To test this hypothesis, gas-phase H/D exchange (GP-HDX) experiments were performed. As shown in Figure 22A, it is observed that (*Z*)-**1** exchanges slower than (*E*)-**1**, i.e. $k_{(E)}/k_{(Z)} \approx (2.5 \pm 0.4)$, which is in line with the proposed ionic hydrogen bond in the (*Z*)-isomer. To further support this interpretation, semiempirical calculations were performed at the PM3 level of theory.[132] As shown in Figure 22B, the (*Z*)-isomer is indeed predicted to be about $\Delta E \approx 15$ kJ/mol more stable, and the hydrogen bond is

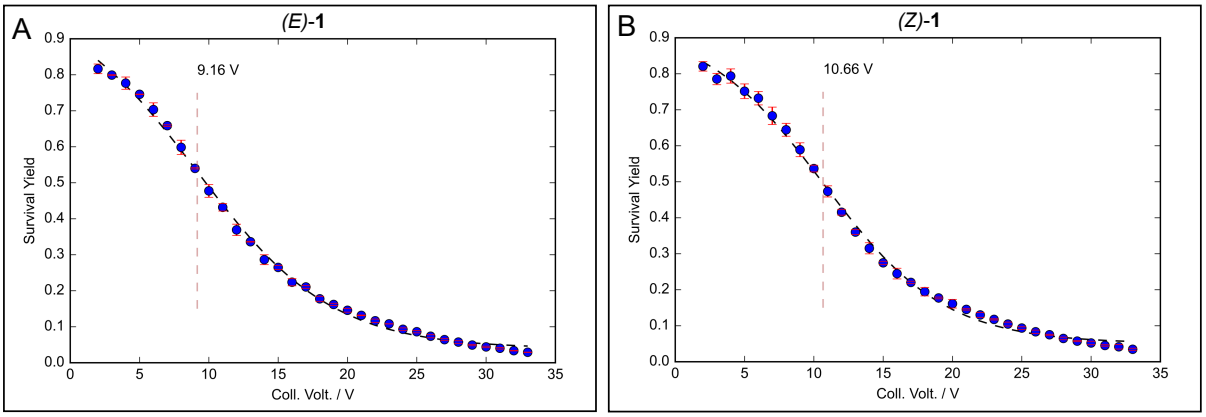

Figure 21: Survival-yield (SY) method for the determination of the characteristic collision voltage (CCV). A: SY-plot of (*E*)-**1**+$H^{\oplus}$. B: SY-plot of (*Z*)-**1**. Surprisingly, the gas-phase stability of (*Z*)-**1**+$H^{\oplus}$ is higher than that of (*E*)-**1**+$H^{\oplus}$. Copyright Wiley-VCH Verlag GmbH & Co. KGaA. Reproduced with permission.[153]

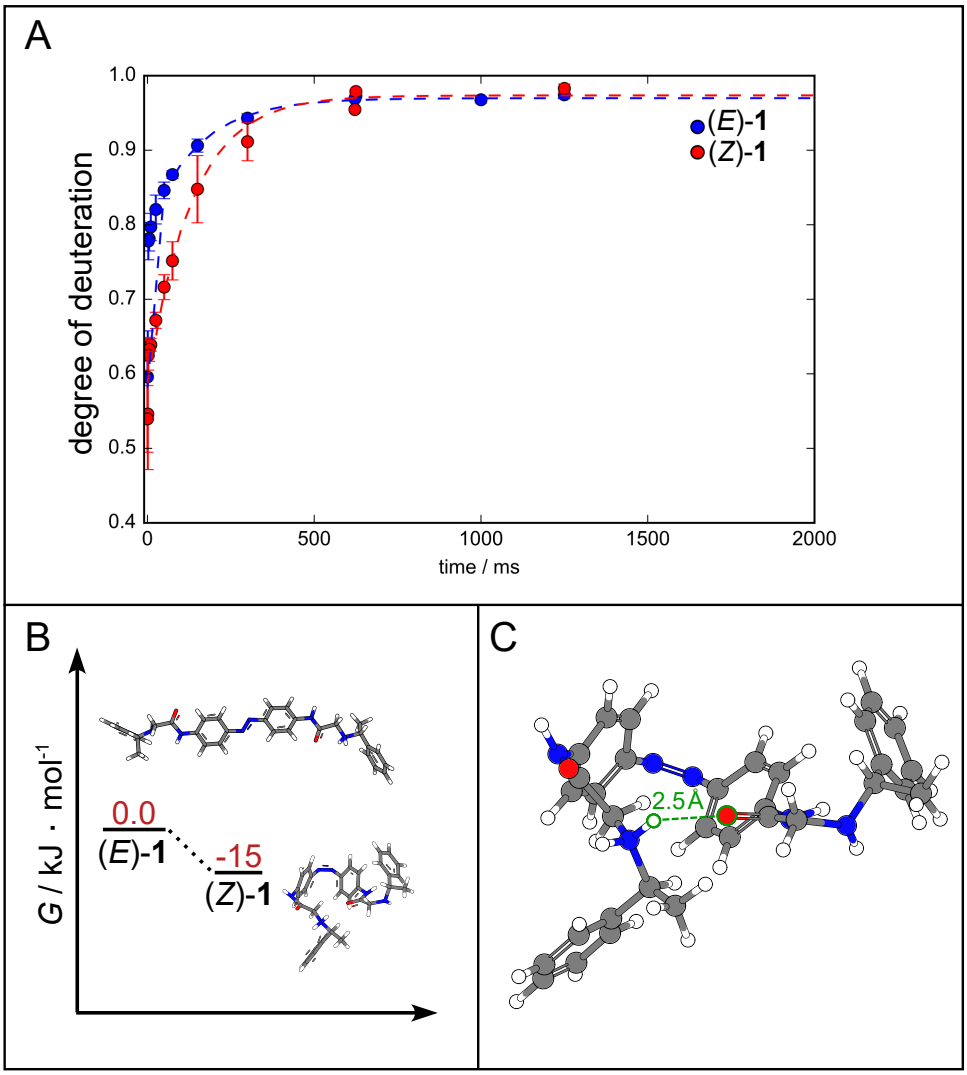

Figure 22: A: Gas-phase H/D-exchange experiment of (*E*)-**1**+$H^{\oplus}$ and (*Z*)-**1**+$H^{\oplus}$ with MeOD, which both follow a pseudo-first-order reaction. A faster exchange is observed for (*E*)-**1**+$H^{\oplus}$ ($k_{(E)}/k_{(Z)} \approx 2.5 \pm 0.4$). B: Modelling of the gas-phase stability of both photoisomers using the semiempirical PM3 method. C: Lowest energy conformer of (*Z*)-**1**. The proton bridge ($N^{\oplus}$–H $\cdots$ O = C) is highlighted. Copyright Wiley-VCH Verlag GmbH & Co. KGaA. Reproduced with permission.[153]

clearly located in the ground state† molecular structure minimum (see Figure 22C). With this good understanding of the protonation site and intramolecular stabilization of (*Z*)-**1** by ionic hydrogen bonding, we turned our attention to the ion mobility experiments. Given a 1:1-mixture of (*Z*)- and (*E*)-**1**, as shown in Figure 23A, the IM-MS experiment yields two peaks in agreement with the initial hypothesis. The drift times of $t_d(Z) \approx 5.2$ ms and $t_d(E) \approx 7.1$ ms correspond to CCS values of $\Omega_{(Z)} \approx 151$ Å^2 and $\Omega_{(E)} \approx 188$ Å^2 after polyalanine calibration. This is in good agreement with theoretical results obtained by CCS predictions, either obtained by the more conventional trajectory

†See footnote on page 25 for a clear definition of *ground state* in this context.

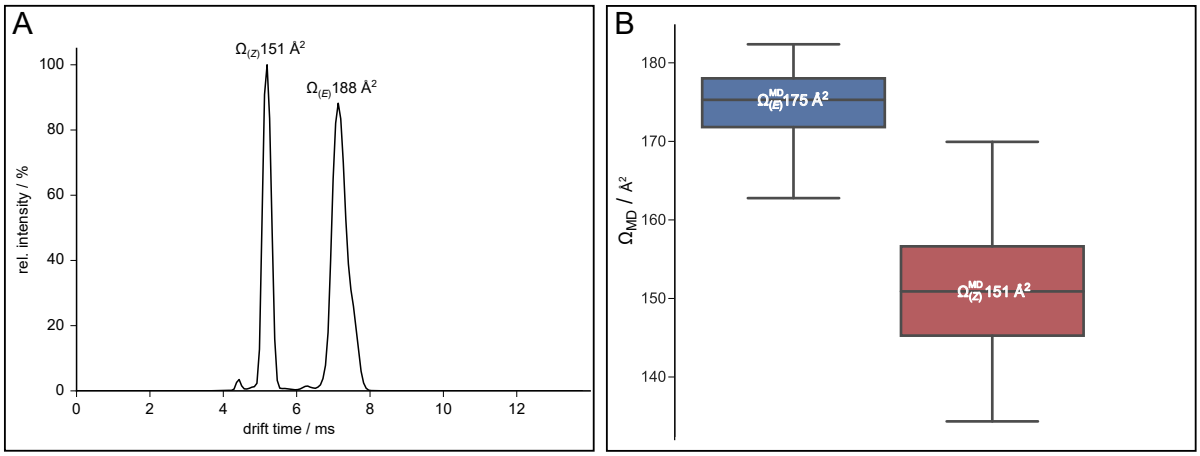

Figure 23: A: Ion mobilogram of a 1:1-mixture of both photoisomers of **1**, featuring two peaks that correspond to (*Z*)-**1**+H^+ and (*E*)-**1**+H^+. B: Theoretical collision cross sections of both photoisomers obtained using the projection approximation on a molecular dynamics simulation (simulation time: 100 ps; time step: 1 fs; using the AMBER force field,[167] and verlocity verlet as implemented in Gabedit.[168]). Copyright Wiley-VCH Verlag GmbH & Co. KGaA. Reproduced with permission.[153]

method (TM) approximation, or by means of a molecular dynamics (MD) simulation ↦ projection approximation (PA) pipeline. Finally, the question was investigated wether the integration obtained from both peaks in the ATD corresponds to the photoisomer content. For this, mixtures of different (*E*)/(*Z*)-isomer ratios were generated by mixing irradiated and non-irradiated **1** in defined amounts. The integral ratio of both peaks properly reflects the photoisomer content with a good linear correlation ($R^2 > 0.978$) that is at a practically useful level. An increase of the trap voltage to induce collisional activation of the ions before entering the IMS cell does not have any observable effect on the isomer ratio. Hence, as long as the activation remains in a reasonable range ($U_{trap} <$ 15 V), no collision-induced isomerization occurs under typical ESI conditions. Upon several cycles of photoswitching, both TW-IMS monitoring and UV-VIS monitoring give comparable results. Hence, quantification of photoisomers can also be reliably performed with this method.

As the ionization efficiency between both photoisomers differ, it is necessary to perform a calibration with known (*E*)/(*Z*)-ratios. However, where relative information is of interest, as for example when first-order processes are to be monitored, no calibration is necessary. To take a concrete example, the determination of first-order thermal relaxation processes is independent of the intensity scale. Here, it would be directly possible to infer the thermal relaxation rate from the integration ratio in the ATD.

The two prior studies show that both very small structural differences (diastereomers) and dynamic properties (photoisomers) can be studied by TW-IMS, but the question remained how the method would perform on larger and more complex molecules.

In my third publication, as the second-author,[169] I performed the IMS measurements in a project with Hendrik Schröder, who developed a new redox-switchable pseudo[1]-rotaxane, that has a lasso-type structure based on crown-ether ammonium complexation. In the wheel of this pseudo[1]rotaxane, a redox-active tetrathiafulvalene (TTF) unit was incorporated (see Figure 24A) that can be reversibly oxidized to the radical cation $TTF^{\cdot+}$ and dication TTF^{2+}. It was recently shown that the redox switching of the TTF unit can be used for the expulsion of the ammonium thread in crown-ether ammonium pseudo[2]rotaxanes.[170]

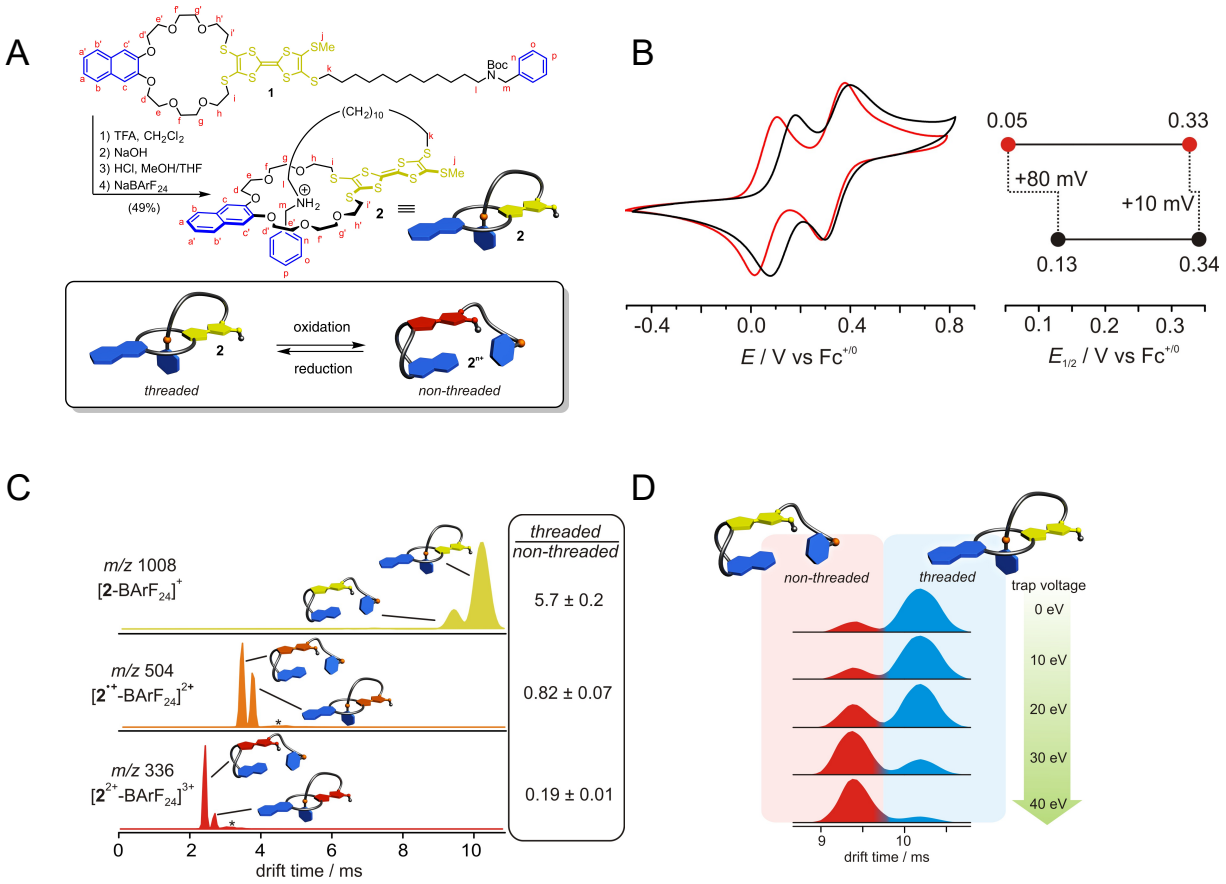

Figure 24: A) Synthesis of lasso-type pseudo[1]rotaxane **2** from Boc-protected precursor **1**. B) Normalized cyclic voltammograms ($100\ mV \cdot s^{-1}$, CH_2Cl_2, 1 mM, 298 K) of precursor **1** (red) and pseudo[1]rotaxane **2** (black) with NBu_4PF_6 (0.1 M) as electrolyte. C) Normalized arrival time distributions (ATDs) in the IM-MS experiment of the increasing oxidation states 0,+1,+2 of **2**. D) Normalized ATDs of the signal for **2** (*m/z* 1008) after collision-induced dissociation (CID) experiments with increasing trap voltage (collision energy) from top to bottom.[169]

In this study, the idea was to use the redox-controlled assembly/disassembly of axle and wheel to implement a lasso-type motion of the pseudorotaxane. In three steps, the Boc-protected precursor **1** was synthesized according to a literature procedure (see Figure 24 A).[171–173] Subsequent deprotection and salt exchange lead to the desired pseudo[1]rotaxane **2** in 49% overall yield. The electrochemical properties of both **1** and **2** were investigated by Hendrik Schröder using cyclic voltammetry (CV). Precursor **1** exhibits two fully reversible redox waves over a wide range of different scan rates, with half wave potentials of $E^1_{1/2} = 0.05$ V and $E^2_{1/2} = 0.33$ V. They correspond to the two one-electron oxidation steps of the TTF unit. The redox potentials of **1** provide a reference, as no repulsive axle-wheel interaction can occur. Pseudo[1]rotaxane **2** also exhibits two reversible redox waves ($E^1_{1/2} = 0.13$ V; $E^2_{1/2} = 0.34$ V) which are, however, anodically shifted by $\Delta E^1_{1/2} = +80$ mV and $\Delta E^2_{1/2} = +10$ mV, in comparison to **1**, respectively. Structurally, these potential differences can be explained by considering the charge repulsion between the oxidized TTF unit at the wheel and the threaded ammonium axle. Hence, the less strongly affected second oxidation potential is indicative of a partial expulsion of the axle that occurs already after the first oxidation step. To reveal further details of the redox-switching process, digital simulations of the cyclic voltammogram were performed, that give approximate equilibrium constants of the different redox states.

It has to be noted that the lasso-type molecular motion cannot be easily shown by NMR spectroscopy, as the singly oxidized radical-cation is a paramagnetic species, which leads to substantial line-broadening. Therefore, only the CV data were available to support the claim of a lasso-type redox-responsive behavior.

To provide definite evidence of the redox-induced opening of **2** by a "lasso"-type mechanism, I performed IM-MS experiments utilizing the setup described in section 2.7. As shown in Figure 24 C, pseudorotaxane **2** does indeed successively unfold upon increase of the oxidation state. Furthermore, the equilibrium constants by IMS are in good agreement with the constants obtained by digital simulations of the CV in solution. Finally, energy-resolved ion mobility unfolding experiments were performed as described in section 2.3. As shown in Figure 24 D, the pseudorotaxane **2** does indeed open up upon collisional activation before the ion mobility cell. These results strongly support the proposed redox-induced opening of **2**.

At first glance, the fact that the opened molecular lasso corresponds to a smaller ion than the threaded structure might seem surprising. However, a similar effect was noted in an IMS study of lasso peptides.[174] Hence, there seem to be two viable explanations for this unexpected effect: (1) After unthreading of the molecular lasso, the positively charged ammonium station is stabilized by dipole interactions with the electron-rich naphtalene moiety, or (2) the reduction in size upon unthreading is an inherently geometric effect, which would explain why a similar observation has been reported for the structurally unrelated, but topology-wise homologous lasso peptides.[174] The reason for this effect could lie in the gained flexibility of the ion after unfolding, which could give access to a randomly coiled, globular conformation. The closer the geometry approaches an ideal sphere, the higher the reduction in the CCS value. As this discussion shows, there are still several interesting questions left to be answered about the influence of the "topology" on the CCS value. From this angle, the question if other "lasso"-type objects will similarly exhibit a smaller CCS/drift time upon opening is intriguing.

The previous study illustrates that IM-MS can visualize the molecular motion induced by charge repulsion in TTF based systems. Naturally, the question then arised whether an even more complex rotaxane system featuring multiple TTF sites can be investigated in a similar manner.

Hence, *in my fourth publication, as the third-author,* I contributed IMS measurements to investigate the accordion-like motion of a group of electroswitchable crown ether/ammonium-oligorotaxanes (see Figure 25). Briefly, the conclusions that can be drawn stem from the charge repulsion-induced increase in the CCS value upon oxidation of the TTF wheels on the oligorotaxane. While the first oxidation of the single-unit rotaxane leads to a big increase in the CCS of $\Delta\Omega \approx +60$ Å^2, a much smaller increase of $\Delta\Omega \approx +15$ Å^2 is observed for the oligorotaxane with two wheel units. These observations are in line with the proposed intramolecular charge stabilization within the mixed-valence complex of the TTF-bearing wheels. Hence, when taking the other spectroscopic results by CV/DPV, EXSY-NMR, EPR and UV/VIS into account, this strongly indicates that an accordion-like motion is operative in the studied oligorotaxane.

As in the third study, IM-MS enables the observation of the dynamic movement of a molecular switch that is hardly available through any other spectroscopic technique.

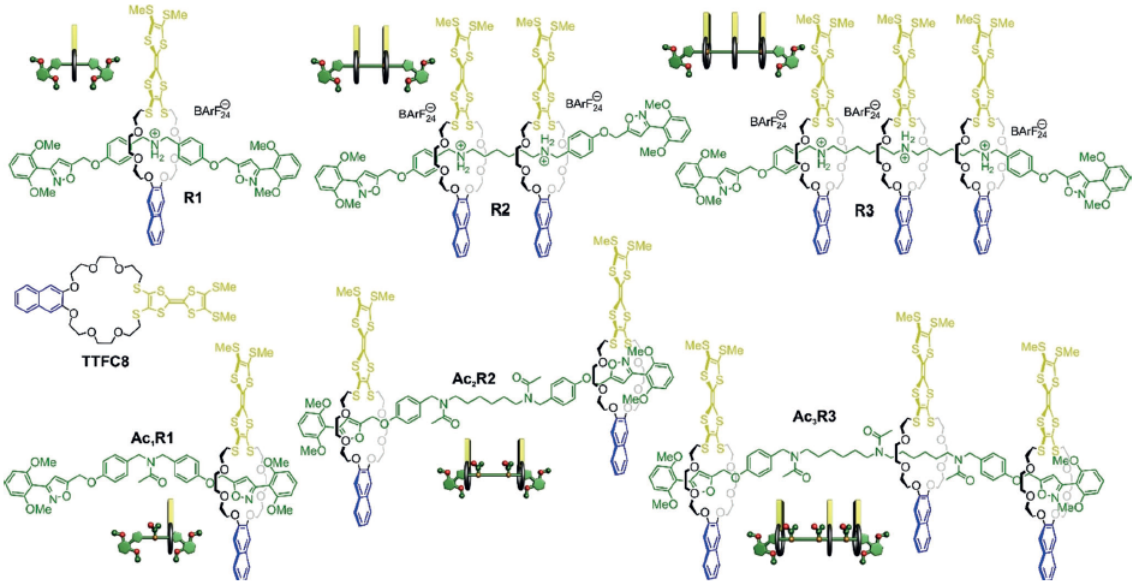

Figure 25: TTF-containing wheel **TTFC8**, free ammonium (**Rn**) and acetylated (**AcnRn**) oligo[n+1]rotaxanes (n = 1–3), and their cartoon representations ($BArF_{24}^-$ = tetrakis(3,5-bis(trifluoromethyl)phenyl)borate). Reproduced from [175] with permission by John Wiley & Sons, Inc.

In my fifth publication,[176] I contributed exchange kinetics experiments by mass spectrometry to a study of hierarchically assembled helicates, that are a probe for the evaluation of the energetics of weak interactions. As shown in Figure 26A, two catecholate based titanium helicates $Li_2[\mathbf{L}_3^{\mathbf{R}}Ti]$ form a triply lithium-bridged dimer $Li[Li_3\mathbf{L}_6^{\mathbf{R}}Ti_2]$. As shown in Figure 26B, the energetics of the putative dispersive interactions between two helicate cores can be determined by comparing differently subtituted systems with the other substituents or the unsubstituted case. The difference then corresponds to the Gibb's free enthalpy of the interaction, $\Delta\Delta G_{vdw}$. In the same fashion, $\Delta\Delta H_{vdw}$ and $\Delta\Delta S_{vdw}$ are obtained. While the main argumentation of the study revolves around the NMR characterization of the energetics of the monomer/dimer equilibrium, I contributed MS exchange experiments. A typical exchange reaction is shown in Figure 26C, in this case the exchange of methyl- and ethyl-substituted helicate cores. Figure 26D shows the corresponding mass spectrum, in which both reactants and the five exchange products can be clearly identified. In this fashion, the gradual exchange of helicate cores was monitored over time for all substituent sizes (R = Me, Et, *n*Pr, *n*Bu, *n*Pent, *n*Hex, *n*Hept, *n*Oct, *n*Non, *n*Dec, *n*Undec), from which a roughly linear correlation between exchange rate and substituent size was obtained. This trend is in agreement with the postulated dispersive interactions between

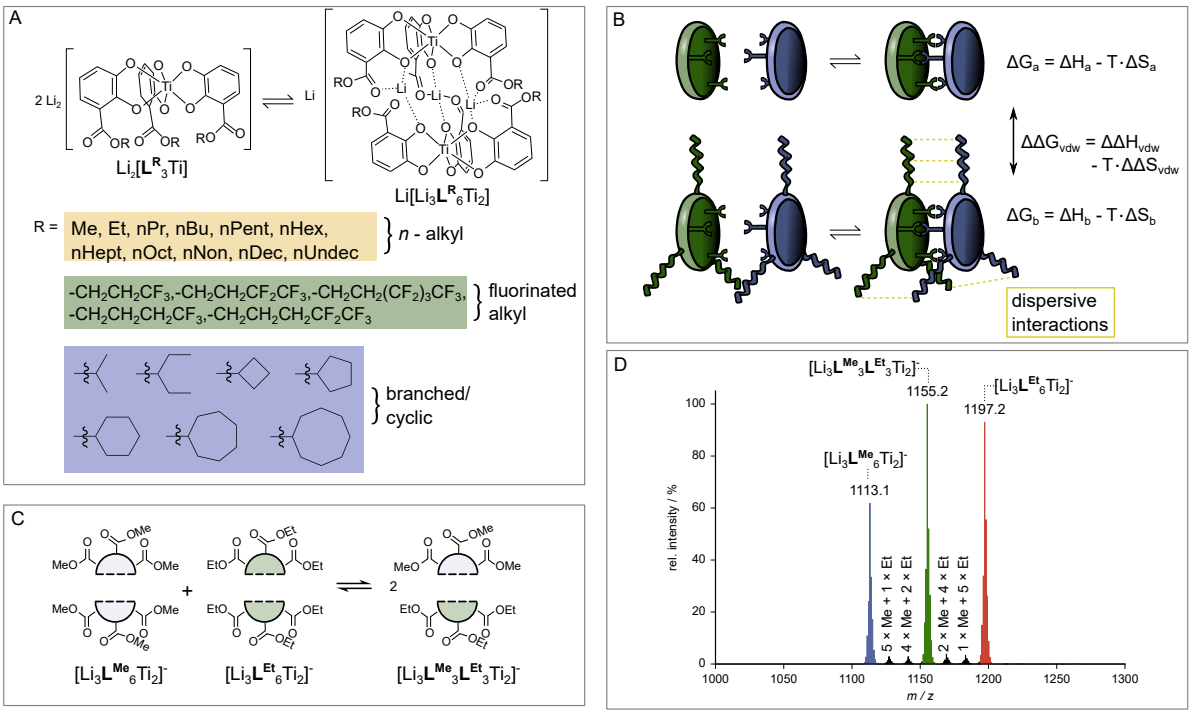

Figure 26: A: Monomer-dimer equilibrium of ester-substituted hierarchically formed catecholate-based triply lithium-bridged helicates with different classes of substituents. B: Schematic illustration of the monomer-dimer equilibrium, by which the weak interactions between the substituents can be determined. C: Exchange of mehtyl helicate $[Li_3\mathbf{L}_6^{\mathbf{Me}}Ti_2]^{\ominus}$ with ethyl substituted helicate $[Li_3\mathbf{L}_6^{\mathbf{Et}}Ti_2]^{\ominus}$ and the corresponding ESI mass spectrum (D).

substituents of the helicate cores, as the additional stabilization of the dimer will likely slow down the exchange kinetics as well. While the MS exchange experiments clearly show longer exchange times for bigger alkyl chain substituents—and are thus congruent with the putative dispersive interactions in the helicates—other effects could be responsible for the observations made, instead. For example, the long-chained alkyl substituents are non-polar, while the core is highly polar, so the substituent size could stronlgy affect the solute-solvent interactions as well, which could influence both thermodynamics and kinetics of the 2 $\times$ helicate-monomer $\leftrightharpoons$ helicate-dimer equilibrium. Hence, it is still questionable if the observed trends in thermodynamics and kinetics are indeed caused by dispersive interactions. Still, the two observations that 1) the trend in thermodynamic parameters by NMR spectroscopy in DMSO as the solvent and 2) the exchange kinetics via MS in THF as the solvent both fit to the theory of putative dispersive interactions make the involvement of solvent effects quite unlikely. In this regard, the MS measurements provided additional assurance that solvent-solute interactions due not interfere with the conclusions drawn in the publication.

In the next section, a short list of the major conclusions of the five studies is presented and the subsequent outlook section will discuss remaining questions and possible future directions for further research.

3.1 Main conclusions

1. Study. *Chiral recognition in crown ether/ammonium complexes.*
    - The importance of a single hydrogen bond for the gas-phase chiral recognition of crown ether/ammonium complexes is revealed by GP-HDX and targeted methyl esterification.
    - The *ee* quantification via the systematic change in the centroid drift time is evaluated as a practically useful technique.
2. Study. *IMS study of photoisomerism in a 4,4'-diamidoazobenzene model.*
    - If the azobenzene moiety is protonated, a fast thermal backrelaxation is induced, so that photoisomers cannot be distinguished via IMS.
    - In the present model system, the (*Z*)-isomer displays a higher gas-phase stability than the (*E*)-isomer.
    - GP-HDX experiments reveal the underlying hydrogen bond responsible for this surprising stabilization effect.
3. Study. *Redox-controlled self-inclusion of a pseudo[1]-rotaxane ("molecular lasso").*
    - Ion mobility-mass spectrometry experiments allow the direct observation of the redox-controlled opening of the molecular lasso due to TTF^{n+}/NH_3R^+-charge repulsion.
    - Increasing oxidation states go along with the successive unfolding of the molecular lasso.
    - In the same manner, collisional activation also induces a gradual opening of the molecular lasso.
    - The quantitative equilibrium constants obtained by IM-MS are in reasonable agreement with the CV experiments carried out in solution.

4. Study. *Accordion-like motion in electrochemically switchable crownether/ammonium oligorotaxanes.*

    - Comparison of CCS trends with different oxidation states supports the accordion-like motion in the oligorotaxane due to TTF^{n+}/TTF^{n+}-charge repulsion.

5. Study. *Chasing weak forces: hierarchically assembled helicates as a probe for the evaluation of the energetics of weak interactions.*

    - Titanium helicates with larger substituents exhibit slower exchange rates in kinetics monitored by ESI-MS. This supports the proposed theory of dispersive interactions between the helicate cores.

4
CHAPTER

Discussion and outlook

After summarizing the main results of the five studies in the preceding chapter, this discussion and outlook section seeks to discuss the relation of the work to prior research in the field of gas-phase supramolecular chemistry as well as possible future directions. The main theme of the presented work is that it is the *combination* of IM-MS with CID and GP-HDX that leads to the highest detail of information about the gas-phase structure and behavior of the ion.

The first study of this thesis on the chiral recognition in crown ether ammonium complexes is based on a thorough foundation of prior reports on the subject. Figure 27 shows several other chiral crown ether hosts that have been described for chiral recognition by mass spectrometry.[177] In fact, numerous other chiral selectors (cinchona alkaloids,[178,179] cyclodextrines,[180,181] resorcinarenes,[182,183] tetralactam macrocycles[184,185]) may be employed to study a plethora of analytes (alkyl ammonium ions,[186,187] amino acids,[180,188] peptides,[189,190] and drugs such as ibuprofen,[191] penicillamine,[192] pramipexole,[193] tenofovir,[193] valacyclovir[193]). All the cited studies

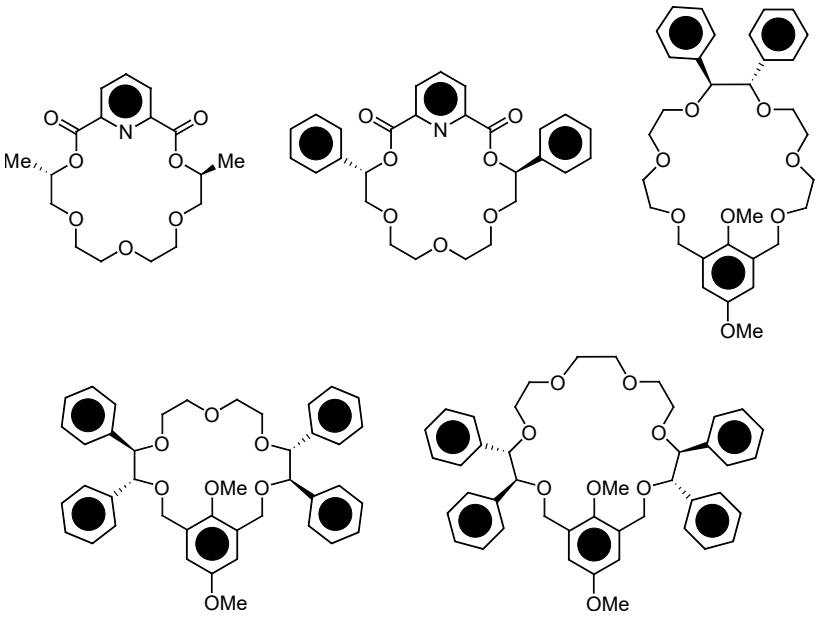

Figure 27: Several examples of crown ethers used in MS chiral recognition studies.[177]

rely on ESI-MS, but employ different methods for achieving enantiodifferentiation. Still, they share the common principle that a diastereomeric complex between the analyte and the chiral selector is formed. The interaction between these two components during complex formation must be strong enough that both diastereomeric complexes differ in an observable physical property. If one wishes to design a chiral selector targeted to a specific analyte, these non-covalent interactions in the complex thus play a crucial role for the success of the chiral recognition.

The reported finding in my thesis that a single hydrogen bond is responsible for the chiral recognition by CCS value is therefore of significance also considering recognition studies with other chiral selectors. So even though similar studies have been reported,[194] the combination of gas-phase techniques to understand the influence of a single hydrogen bonding contribution to the chiral recognition is novel in the field and useful for the design of new chiral selectors.

Still, several questions remain for future research: Would a more stable complex always be more compact (exhibit a smaller CCS), or are there cases where the more stable complex is less compact? Besides (un)natural amino acids, what are possible other substrates to use for the *ee* quantification? Can the method of small CCS changes be used for molecular self-sorting studies? What other types of structural evolution over time can be studied with the "centroid method"?

Several types of photoisomers have been investigated with IMS, as depicted in Figure 28. The energetic barries for isomerization and fragmentation of a series of retinal chromophores were determined by CID-IMS,[195] and the photoisomerization and photodissociation of carbocyanine dyes was achieved by photoexcitation of ions with a Titanium:Sapphire laser immediately before the drift tube,[196] or of azobenzenes by excitation with an LED array during ionization.[197] Donor-acceptor Stenhouse adducts are a new class of photoswitches with excellent synthetic tunability and fatigue resistance.[198,199] A coupling of CID-IM-MS with laser excitation was used to study the two-step photocyclization of a charge-tagged donor-acceptor Stenhouse adduct.[200] Similarly, the (*E*)- and (*Z*)-isomers of a spiropyran-merocyanine were investigated with IM-MS by excitation before ionization.[201]

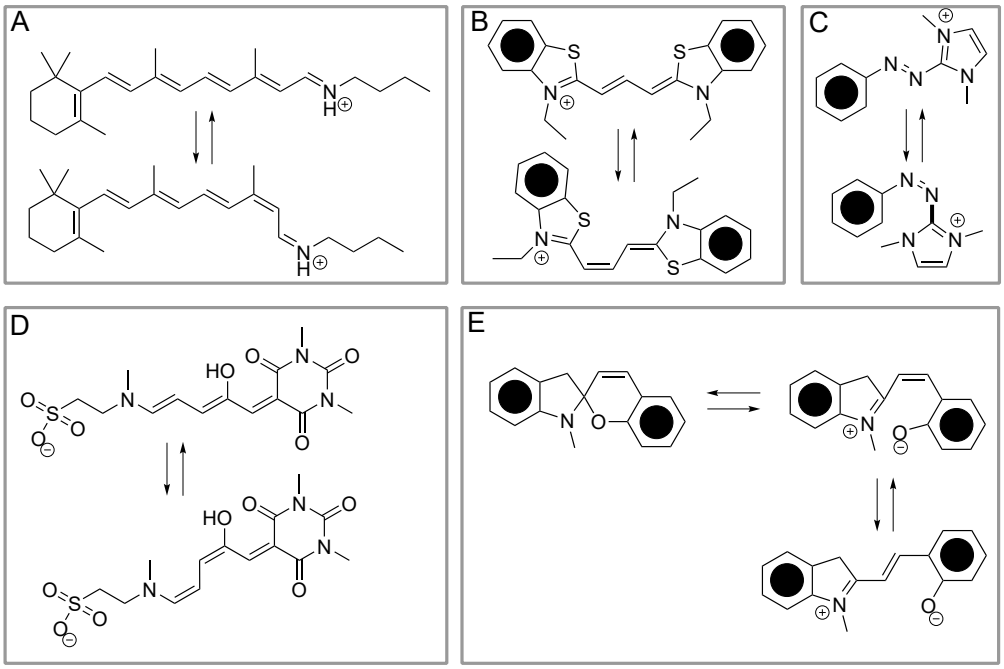

Figure 28: Examples for IMS photoisomerization studies. A: Retinal.[195] B: Carbocyanine dye.[196] C: Azobenzene.[197] D: Stenhouse adduct.[200] E: Spiropyran-merocyanine system.[201]

With the background of this existing research, the second study of my thesis illuminated the possibility of a charge-induced thermal backrelaxation mechanism of azobenzenes that can intervene in the differentiation of photoisomers. Hence, it is important that sites for stable charge formation are available remotely to the azogroup. It was shown that, when these conditions are met, even quantitative information about the photoisomerization process can be revealed. Again, the combination of different gas-phase techniques is a novel direction in the field of gas-phase photoisomerization studies and the information that nearby charges can induce backisomerization is also valuable from a practical viewpoint.

In the future, it would be interesting to generalize the presented method to the study of multi-component mixtures and possibly other types of photoswitches (e.g. spiropyrans, diarylethenes) in a quantitative fashion. It would also be interesting to discover if other photoswitch types similarly exhibit reversed gas-phase stabilities compared to the solution environment.

In my third study, unfolding experiments were performed by coupling CID and IM-MS to investigate the opening of the molecular lasso. One early study reported a CID-IM-MS assay for the quantification of the stabilization that ligand binding has on the folded state of soluble and membrane proteins.[202] By monitoring the CCS value of the

protein-ligand complex while increasing the collisional activation, the energetic barrier for unfolding was revealed. If the stabilizing effect of ligand-protein binding is large, one requires a high collision energy to induce unfolding, which can be quantified using specialized data analysis software.[202,203]

In fact, there are numerous reports of the application of IM-MS to biomolecules.

But while there is a similar interest in the investigation of the binding of small molecules to artificial supramolecular receptors, the number of IM-MS studies on artificial supramolecular systems remains comparably scarce.[203]

One IM-MS study[204] on the binding of lysine to cucurbiturils (see Figure 29A) and α-cyclodextrin reported the interesting observation that $[CB[5]+Lys+H]^+$ corresponds to an exclusion-complex ($\Omega_{exp} \approx 184$ Å^2, $\Omega_{theor,incl} \approx 170$ Å^2, $\Omega_{theor,excl} \approx 185$ Å^2), while $[CB[6]+Lys+2H]^{2+}$ is a threaded inclusion structure ($\Omega_{exp} \approx 189$ Å^2, $\Omega_{theor,incl} \approx 193$ Å^2, $\Omega_{theor,excl} \approx 218 - 225$ Å^2).[204] A very interesting insight into the structure of

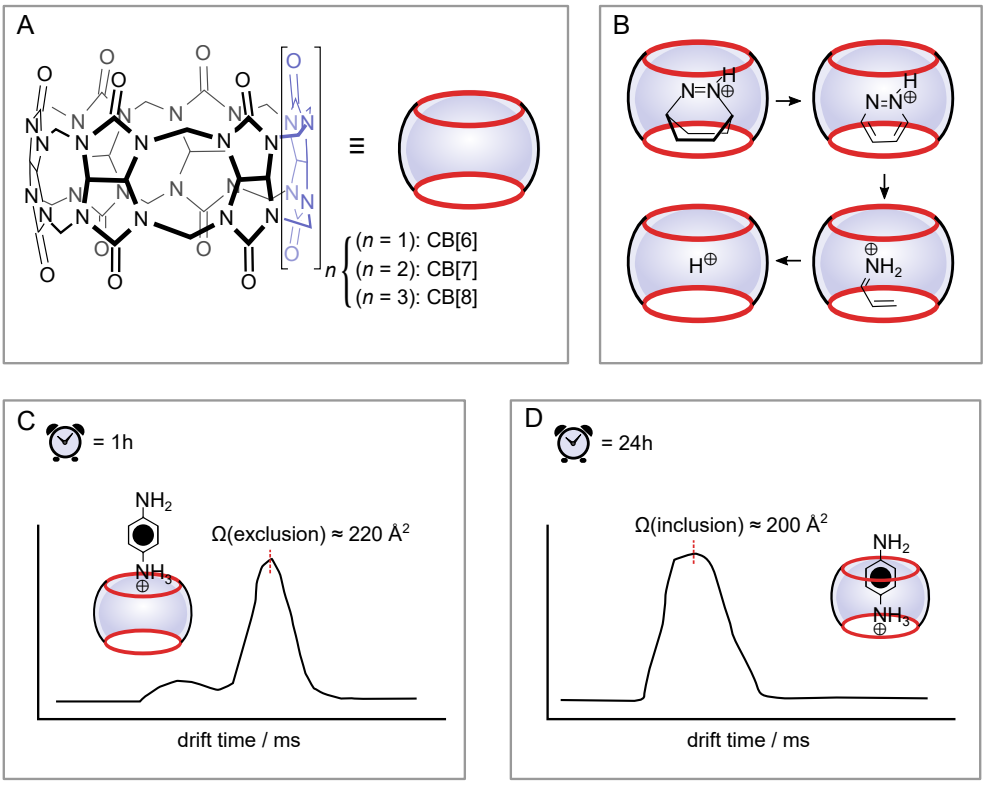

Figure 29: A: Structure of cucurbit[6-8]urils (CB). B: Fragments observed for a hydrophobic azocompound in CB[7]. By CID-IMS, the compactness of the host with different guests can be investigated. For example, the protonated form was shown to be less compact than the inclusion complex with the guest.[205] C: Schematic drawing of the exclusion complex of protonated *para*-phenylenediamine with CB[6] and the analogous inclusion complex (D).[120]

the inclusion complex of CB[7] with a hydrophobic azocompound as the guest was reported by CID-IM-MS.[205] As shown in Figure 29B, the guest successively fragments until the protonated CB[7] is left. Interestingly, the proton adduct corresponds to a larger drift time than the inclusion complex with the whole guest. Hence, the intramolecular forces that stabilize the host-guest complex also induce a compactation of the ion in the gas-phase.[205]

For the binding of CB[6] to protonated *para*-phenylenediamine as the guest, the time dependence of inclusion complex formation was studied.[120] As sketched in Figure 29C, the exclusion complex corresponds to a larger CCS value ($\Omega_{(\text{exclusion})} \approx 220$ Å^2), while the threaded structure (Figure 29D) is about 10% smaller ($\Omega_{(\text{inclusion})} \approx 200$ Å^2).[120]

A recent study of an oligorotaxane investigated the progressive unfolding upon increasing charge states by a combination of CCS calculations with PM6 molecular dynamics simulations.[206] These examples illustrate that IM-MS represents an ideal tool to differentiate exclusion and inclusion complexes.

When comparing the third study of the thesis with this existing research, it could be argued that the differentiation of threaded from dethreaded complexes has already been established. However, note that our study showed that the integration in the IM-MS experiment reproduces the equilibrium constants obtained by CV in solution. Hence, it was shown that a quantitatively accurate picture of the redox-controlled opening of the pseudo[1]rotaxane in solution was obtained. Furthermore, the unfolding of the pseudo[1]rotaxane yields a more compact ion—a surprising finding.

Several interesting questions remain for future research: Can equilibrium constants be determined in the same way for other types of redox switches? What is the reason for the surprising observation that the opened molecular lasso corresponds to a smaller CCS value? And why is a similar effect observed for lasso peptides which are only related by the topology of the system? Can the observed phenomenon be reproduced with molecular modelling or molecular dynamics simulations?

It was a recurrent theme in the studies of this thesis and in several of the discussed references, that it is the *combination* of IM-MS with CID and GP-HDX that leads to the most detailed information about the gas-phase structure and behavior of the ion.

A combination of IM-MS and GP-HDX was used in studies on bradykinin fragments,[207] and for lasso peptides,[174] while the coupling of CID and IM-MS was for example used

in the structure elucidation of strained aromatic hydrocarbon macrocycles.[208]
However, the five studies of this thesis show unprecented ways in which the combination of *all three methods* allow both the differentiation of isomers and the investigation of non-covalent interactions. Figure 6 gives a final overview of the information that can be obtained by designing gas-phase experiments with a combination of these methods.

Table 6: As the examples from this thesis show, a combination of IM-MS, CID and GP-HDX gives detailed insight into the gas-phase structure and dynamics of an ion.

	IM-MS	CID	GP-HDX
observables:	m/z, drift time, CCS, ΔCCS on activation	fragmentation, characteristic collision energy	number of exchanging protons, rate of exchange
non-covalent interactions:	unfolding studies	stability of interactions	hydrogen bonding
isomerism:	diastereomers, inclusion vs exclusion, (E)/(Z)-photoisomers, conformers (some cases)	inclusion vs exclusion, diastereomers (Cooks' kinetic method)	inclusion vs exclusion

In future studies, it would be possible to gain even more structural insights into hydrogen bonding by the use of IRMPD action spectroscopy. With this, a much more detailed view of an ion's structure could be obtained in some cases.[209–212]
Another intriguing direction for future research could be the computational prediction of mass spectra.[115,116] In particular, the computational prediction of CID spectra could give additional structural information of the ion.[114]
Another interesting type of experiment is ozone-induced dissociation in TW-IMS, that was recently reported for our instrument setup.[213]
From the viewpoint of systems chemistry, a fascinating possibility is to study the structural evolution of a complex system over time, as was recently showcased for TW-IMS.[120]
One very exciting question is whether gas-phase structural characterization techniques give an accurate picture of the solution environment. In this regard, studies that combine several independent techniques and compare the structural information are very

valuable. Table 7 gives a selection of techniques for possible future studies, along with their advantages and disadvantages.

As this discussion shows, the possibilities to extend the presented work in the future are only limited by the creativity of the researcher.

Table 7: Overview of the three gas-phase techniques in comparison to three common solution techniques.

method	IM-MS	MS/MS	GP-HDX	NMR spectro-scopy	X-ray crystallo-graphy	circular dichroism
phase	gas	gas	gas	liquid, solid (or gas)	solid	liquid, solid, gas
sample	highly sensitive, low sample consumption	highly sensitive, low sample consumption	highly sensitive, moderate sample consumption	non-destructive, around > 0.1 mg of sample needed	non-destructive, must be crystallized	non-destructive
mixtures	mixtures can be analysed with high analytic capacity	mixtures can be analysed with high analytic capacity	mixtures can be analysed with high analytic capacity	generally difficult, DOSY or 3D-NMR may assist in complex samples	pure sample needed	pure sample needed
speed	rapid acquisition, time limiting factor is often the simulation	rapid, interpretation maybe aided by spectral databases or *ab initio* methods	relatively slow as different HDX times must be scanned	can be rapid for small molecules (<500 Da)	slow	rapid
structural information	information about spatial (3D) arrangement of ion: individual isomers and conformers may be identified	information about connectivity from fragments, stability information from SY method	information about hydrogen bonding, in some cases about 3D structure of ion	detailed structural information about all aspects of molecular structure	direct determination of atomic positions, thus including stereochemical information, bond lengths and angles	diagnostic information about certain structural features such as α-helicity
limits	CCS calculations rely on simulations that are challenging for large systems, resolution may be too low	no detailed insight into 3D structure, isomers and conformers typically not distinguished, kinetic shift	interpretation of HDX results can be challenging, often additional tests with complementary techniques needed	mixtures lead to complex spectra that are hard to interpret, large amount of sample needed	only pure crystal, representative of solution?	cannot be used for mixtures, no detailed structural information except characteristic bands

5
CHAPTER

Research Projects

5.1 IMS and gas phase H/D exchange: revealing the importance of a single hydrogen bond for the chiral recognition of crown ether ammonium complexes

The study discussed in this chapter has been published at the 23th of April 2018 in *Chemical Communications*, a peer-reviewed journal of the royal society of chemistry:

> Ion mobility and gas phase H/D exchange: revealing the importance of a single hydrogen bond for the chiral recognition of crown ether ammonium complexes
> Wollschläger, J. M. ; Simon, K.; Gaedke, M. and Schalley, C. A.
> *Chem. Commun.* **2018**, *54*, 4967-4970.
> This work is available online:
> https://doi.org/10.1039/C8CC01671B

Abstract. Two new BINOL-based chiral crown ether/ammonium complexes are studied by travelling-wave ion-mobility spectrometry. Homo- and heterochiral crown ether/ammonium complexes differ in their collision cross sections, and these differences go along with changes in hydrogen bonding as revealed by gas phase H/D-exchange experiments. Applications for the determination of enantiomeric excess are discussed.

Contributions made by the author:
The author is first author and major contributor to the study, including formulation of the main argumentation, the design of gas-phase experiments, and writing of the manuscript. Marius Gaedke performed the synthesis of the new BINOL macrocycles. Konstantin Simon contributed to the gas-phase experiments and data analysis procedures during a student internship.

5.2 IMS study on the photoisomerization of a 4,4'-diamidoazobenzene model

The study discussed in this chapter has been first published at the 4th of February 2019 in *ChemPhotoChem*, a peer-reviewed journal at Wiley-VCH:

Ion Mobility-Mass Spectrometric Investigation on the Photoisomerization of a 4,4'-Diamidoazobenzene Model
Wollschläger, J. M. and Schalley, C. A.
ChemPhotoChem **2019**, *in press*.
This work is available online:
https://doi.org/10.1002/cptc.201800251

Abstract. The photoisomerization of a new 4,4'-diamidoazobenzene model is investigated with ion mobility-mass spectrometry. Taking observations of previous studies and new control experiments into consideration, a mechanism for a fast thermal (*Z*)→(*E*)-isomerization of azobenzenes during ionization is proposed. The experiments clearly show that a fast (*Z*)→(*E*) isomerization is operative when the azo group is protonated, while it can be prevented, when another protonation site remote from the azo group is offered. Besides this, the peak integration ratio in the ion mobilogram is shown to closely correlate with the photoisomer ratio in solution. Future prospects for applications in photocatalysis and systems chemistry are discussed.

Contributions made by the author:
The author is creator and major contributor to the study, including synthesis, design of gas-phase experiments, and writing of the manuscript. The author wants to thank students Thobias Trebut and Lukasz Polewski for contributions to this project during student internships.

5.3 Redox controlled self-inclusion of a pseudo[1]-rotaxane

The study discussed in this chapter has been published at the 26th of July 2017 in *Chemical Communications*, a peer-reviewed journal of the royal society of chemistry:

Redox-controlled self-inclusion of a lasso-type pseudo[1]rotaxane
Schröder, H. V.; Wollschläger, J. M. and Schalley, C. A.
Chem. Commun. **2017**, *53*, 9218-9221.
This work is available online:
https://doi.org/10.1039/c7cc05259f

Abstract. The self-inclusion behavior of a tetrathiafulvalene-containing lasso-type pseudo[1]rotaxane can be reversibly switched between threaded and non-threaded states by redox-stimuli. The switching mechanism was investigated by cyclic voltammetry in solution and monitored by ion mobility mass spectrometry in the gas phase.

Contributions made by the author:
Design and synthesis of the pseudo[1]rotaxane have been performed by H.V. Schröder. The author designed energy-resolved ion mobility experiments as well as ionization and oxidation procedures that are compatible with ESI-MS analysis. This entails careful optimization of instrument parameters to ensure control over the internal energy of the ions. The ion mobility data are in good agreement with the results of cyclic voltammetry experiments carried out in solution by H.V. Schröder, and were utilized in the present study to confirm the redox-controlled switching of the tetrathiafulvalene based lasso-type pseudo[1]rotaxane, thus providing the evidence for the major claim of the study.

5.4 Accordion-like motion in electrochemically switchable crown ether/ ammonium oligorotaxanes

The study discussed in this chapter has been published at the 25th of October 2017 in *Journal of the American Chemical Society*, a peer-reviewed journal of the american chemical society:

Accordion-Like Motion in Electrochemically Switchable Crown Ether/ Ammonium Oligorotaxanes
Schröder, H. V.; Stein, F.; Wollschläger, J. M. and Sobottka, S.; Gaedke, M.; Sarkar, B. and Schalley, C. A.
Angew. Chem. Int. Ed. **2019**, *58*, 1-6.
This work is available online:
https://doi.org/10.1002/anie.201813265

Abstract. Reversible oxidation reactions in electrochemically switchable oligorotaxanes with tetrathiafulvalene (TTF) decorated 24-crown-8 ether wheels generate intramolecular mixedvalence and radical-cation interactions between the wheels. This induces shuttling of the wheels and a contraction of interwheel distances. Further oxidation generates repulsive forces between the TTFs and maximizes the inter-wheel distances instead. These interactions and co-conformational changes were not observed for structurally similar controls in which acetyl groups along the axle prevent translational motion of the wheels. This operation mode of oligorotaxanes, which is reminiscent of an accordion-like motion, is promising for functional materials and nanodevices such as piston-type rotaxane motors.

Contributions made by the author:
The author contributed IMS experiments for the free and acetylated TTF oligorotaxanes in different charge/oxidation states. Parameters for TW-IMS parameters have been properly tuned to cover the range of charge states from +1 to +3. By comparison of CCS values between different oxidation states of the oligorotaxanes, additional evidence for the accordion-like motion was gained to complement the other spectroscopic techniques.

5.5 Chasing weak forces: hierarchically assembled helicates as a probe for the evaluation of the energetics of weak interactions

The study discussed in this chapter has been published at the 25th of October 2017 in *Journal of the American Chemical Society*, a peer-reviewed journal of the american chemical society:

> Chasing Weak Forces: Hierarchically Assembled Helicates as a Probe for the Evaluation of the Energetics of Weak Interactions
> Van Craen, D.; Rath, W. H.; Huth, M.; Kemp, L.; Räuber, C.; Wollschläger, J. M. ; Schalley, C. A.; Valkonen, A.; Rissanen, K. and Albrecht, M.
> *J. Am. Chem. Soc.* **2017**, *139*, 16959-16966.
> This work is available online:
> https://doi.org/10.1021/jacs.7b10098

Abstract. London dispersion forces are the weakest interactions between molecules. Because of this, their influence on chemical processes is often low, but can definitely not be ignored, and even becomes important in cases of molecules with large contact surfaces. Hierarchically assembled dinuclear titanium(IV) helicates represent a rare example in which the direct observation of London dispersion forces is possible in solution even in the presence of strong cohesive solvent effects. Hereby, the dispersion forces do not unlimitedly support the formation of the dimeric complexes. Although they have some favorable enthalpic contribution to the dimerization of the monomeric complex units, large flexible substituents become conformationally restricted by the interactions leading to an entropic disadvantage. The dimeric helicates are entropically destabilized.

Contributions made by the author:
The author contributed MS/MS experiments and time-resolved MS studies to reveal the exchange kinetics of the titanium helicates for a homologous series of different *n*-alkyl, cycloalkyl, branched alkyl and fluoroalkyl substituents. The exchange kinetics contributed evidence to the study of dispersive interactions in the titanium helicates.

6

CHAPTER

Appendix

Bibliography

[1] Steed, J. W.; Turner, D. R.; Wallace, K. *Core concepts in supramolecular chemistry and nanochemistry*; John Wiley & Sons Chichester, England, 2007; p.18.

[2] Goshe, A. J.; Crowley, J. D.; Bosnich, B. *Helvetica Chimica Acta* **2001**, *84*, 2971–2985.

[3] Bruns, C. J.; Stoddart, J. F. *The nature of the mechanical bond: from molecules to machines*; John Wiley & Sons, Hoboken, NJ, USA, 2016.

[4] Stoddart, J. F. *Chemical Society Reviews* **2009**, *38*, 1802–1820.

[5] Schröder, H. V.; Hupatz, H.; Achazi, A. J.; Sobottka, S.; Sarkar, B.; Paulus, B.; Schalley, C. A. *Chemistry–A European Journal* **2017**, *23*, 2960–2967.

[6] Schwarz, F. B.; Heinrich, T.; Lippitz, A.; Unger, W. E.; Schalley, C. A. *Chemical Communications* **2016**, *52*, 14458–14461.

[7] Schwarz, F. B.; Heinrich, T.; Kaufmann, J. O.; Lippitz, A.; Puttreddy, R.; Rissanen, K.; Unger, W. E.; Schalley, C. A. *Chemistry–A European Journal* **2016**, *22*, 14383–14389.

[8] von Krbek, L. K.; Achazi, A. J.; Schoder, S.; Gaedke, M.; Biberger, T.; Paulus, B.; Schalley, C. A. *Chemistry–A European Journal* **2017**, *23*, 2877–2883.

[9] von Krbek, L. K.; Achazi, A. J.; Solleder, M.; Weber, M.; Paulus, B.; Schalley, C. A. *Chemistry–A European Journal* **2016**, *22*, 15475–15484.

[10] Traulsen, N. L.; Traulsen, C. H.-H.; Deutinger, P. M.; Müller, S.; Schmidt, D.; Linder, I.; Schalley, C. A. *Organic & biomolecular chemistry* **2015**, *13*, 10881–10887.

[11] Nowosinski, K.; von Krbek, L. K.; Traulsen, N. L.; Schalley, C. A. *Organic letters* **2015**, *17*, 5076–5079.

[12] Qi, Z.; Heinrich, T.; Moorthy, S.; Schalley, C. A. *Chemical Society Reviews* **2015**, *44*, 515–531.

[13] Sakamoto, S.; Fujita, M.; Kim, K.; Yamaguchi, K. *Tetrahedron* **2000**, *56*, 955–964.

[14] Weimann, D. P.; Winkler, H. D.; Falenski, J. A.; Koksch, B.; Schalley, C. A. *Nature chemistry* **2009**, *1*, 573–577.

[15] Winkler, H.; Weimann, D.; Springer, A.; Schalley, C. *Angewandte Chemie International Edition* **2009**, *48*, 7246–7250.

[16] Qi, Z.; Schlaich, C.; Schalley, C. A. *Chemistry–A European Journal* **2013**, *19*, 14867–14875.

[17] Winkler, H. D. F.; Dzyuba, E. V.; Springer, A.; Losensky, L.; Schalley, C. A. *Chemical Science* **2012**, *3*, 1111–1120.

[18] Boeri Erba, E.; Petosa, C. *Protein Science* **2015**, *24*, 1176–1192.

[19] Seo, J.; Hoffmann, W.; Warnke, S.; Huang, X.; Gewinner, S.; Schöllkopf, W.; Bowers, M. T.; von Helden, G.; Pagel, K. *Nature chemistry* **2017**, *9*, 39.

[20] Poyer, S.; Comby-Zerbino, C.; Choi, C. M.; MacAleese, L.; Deo, C.; Bogliotti, N.; Xie, J.; Salpin, J.-Y.; Dugourd, P.; Chirot, F. *Analytical Chemistry* **2017**, *89*, 4230–4237.

[21] Herbert, C. G.; Johnstone, R. A. *Mass spectrometry basics*; CRC press, Boca Raton, Florida, 2002; p 55.

[22] Kebarle, P.; Verkerk, U. H. *Mass Spectrometry Reviews* **2009**, *28*, 898–917.

[23] Gaskell, S. J. *Journal of Mass Spectrometry* **1997**, *32*, 677–688.

[24] Konermann, L.; Ahadi, E.; Rodriguez, A. D.; Vahidi, S. *Analytical Chemistry* **2013**, *85*, 2–9.

[25] Herbert, C. G.; Johnstone, R. A. *Mass spectrometry basics*; CRC press, Boca Raton, Florida, 2002; p 65.

[26] Wilkins, C. L.; Trimpin, S. *Ion mobility spectrometry-mass spectrometry: theory and applications*; CRC press, Boca Raton, USA, 2010.

[27] McLean, J. A.; Ruotolo, B. T.; Gillig, K. J.; Russell, D. H. *International Journal of Mass Spectrometry* **2005**, *240*, 301–315.

[28] Fenn, L. S.; McLean, J. A. *Molecular BioSystems* **2009**, *5*, 1298–1302.

[29] Paglia, G.; Astarita, G. *Nature Protocols* **2017**, *12*, 797–813.

[30] Lapthorn, C.; Pullen, F.; Chowdhry, B. Z. *Mass Spectrometry Reviews* **2013**, *32*, 43–71.

[31] Creaser, C. S.; Griffiths, J. R.; Bramwell, C. J.; Noreen, S.; Hill, C. A.; Thomas, C. L. P. *Analyst* **2004**, *129*, 984–994.

[32] Gabelica, V.; Marklund, E. *Current opinion in chemical biology* **2018**, *42*, 51–59.

[33] Shvartsburg, A. A.; Smith, R. D. *Analytical Chemistry* **2008**, *80*, 9689–9699.

[34] Shvartsburg, A. A.; Jarrold, M. F. *Chemical Physics Letters* **1996**, *261*, 86–91.

[35] Zakharova, N. L.; Crawford, C. L.; Hauck, B. C.; Quinton, J. K.; Seims, W. F.; Hill, H. H.; Clark, A. E. *Journal of the American Society for Mass Spectrometry* **2012**, *23*, 792–805.

[36] Bleiholder, C.; Wyttenbach, T.; Bowers, M. T. *International Journal of Mass Spectrometry* **2011**, *308*, 1–10.

[37] Wu, C.; Siems, W. F.; Klasmeier, J.; Hill, H. H. *Analytical chemistry* **2000**, *72*, 391–395.

[38] Hoffmann, W.; Hofmann, J.; Pagel, K. *Journal of the American Society for Mass Spectrometry* **2014**, *25*, 471–479.

[39] Fujii, T. *Ion/Molecule Attachment Reactions: Mass Spectrometry*; Springer, New York, USA, 2015; p 26.

[40] Derwa, F.; de Pauw, E.; Natalis, P. *Organic Mass Spectrometry* **1991**, *26*, 117–118.

[41] Guo, X.; Duursma, M. C.; Kistemaker, P. G.; Nibbering, N. M.; Vekey, K.; Drahos, L.; Heeren, R. M. *Journal of Mass Spectrometry* **2003**, *38*, 597–606.

[42] Collette, C.; Drahos, L.; Pauw, E. D.; Vékey, K. *Rapid Communications in Mass Spectrometry* **1998**, *12*, 1673–1678.

[43] Guo, X.; Duursma, M. C.; Al-Khalili, A.; Heeren, R. M. *International Journal of Mass Spectrometry* **2003**, *225*, 71–82.

[44] Vékey, K. *Journal of Mass Spectrometry* **1996**, *31*, 445–463.

[45] Memboeuf, A.; Nasioudis, A.; Indelicato, S.; Pollreisz, F.; Kuki, k.; Kéki, S.; van den Brink, O. F.; Vékey, K.; Drahos, L. *Analytical Chemistry* **2010**, *82*, 2294–2302.

[46] Winkler, F.; Golacar, F.; Mermoud, F.; Stahl, D.; Gäumann, T.; Buchs, A. *International Journal of Mass Spectrometry and Ion Physics* **1983**, *46*, 321–324.

[47] Barber, M.; Bordoli, R.; Sedgwick, R.; Tyler, A. *Nature* **1981**, *293*, 270–275.

[48] Göth, M.; Witte, F.; Quennet, M.; Jungk, P.; Podolan, G.; Lentz, D.; Hoffmann, W.; Pagel, K.; Reissig, H.-U.; Paulus, B. *Chemistry–A European Journal* **2018**, *24*, 12879–12889.

[49] Armentrout, P.; Ervin, K. M.; Rodgers, M. *The Journal of Physical Chemistry A* **2008**, *112*, 10071–10085.

[50] Rodgers, M.; Ervin, K. M.; Armentrout, P. *The Journal of Chemical Physics* **1997**, *106*, 4499–4508.

[51] Li, Z.; Couzijn, E. P. A.; Zhang, X. *Chemical Communications* **2012**, *48*, 9864–9866.

[52] Dalleska, N.; Honma, K.; Armentrout, P. *Journal of the American Chemical Society* **1993**, *115*, 12125–12131.

[53] Fujii, T. *Ion/Molecule Attachment Reactions: Mass Spectrometry*; Springer, New York, USA, 2015; p 29.

[54] Winkler, H. D. F.; Dzyuba, E. V.; Schalley, C. A. *New Journal of Chemistry* **2011**, *35*, 529–541.

[55] Campbell, S.; Rodgers, M.; Marzluff, E. M.; Beauchamp, J. *Journal of the American Chemical Society* **1995**, *117*, 12840–12854.

[56] Hemling, M. E.; Conboy, J. J.; Bean, M. F.; Mentzer, M.; Carr, S. A. *Journal of the American Society for Mass Spectrometry* **1994**, *5*, 434–442.

[57] Rajabi, K. *Physical Chemistry Chemical Physics* **2015**, *17*, 3607–3616.

[58] Chen, Y.; Yue, L.; Li, Z.; Ding, X.; Wang, L.; Dai, X.; Fang, X.; Pan, Y.; Ding, C.-F. *Analytical Methods* **2015**, *7*, 5551–5556.

[59] Zherebker, A.; Kostyukevich, Y.; Kononikhin, A.; Roznyatovsky, V. A.; Popov, I.; Grishin, Y. K.; Perminova, I. V.; Nikolaev, E. *Analyst* **2016**, *141*, 2426–2434.

[60] Mistarz, U. H.; Brown, J. M.; Haselmann, K. F.; Rand, K. D. *Analytical Chemistry* **2014**, *86*, 11868–11876.

[61] Rand, K. D.; Pringle, S. D.; Murphy, J. P.; Fadgen, K. E.; Brown, J.; Engen, J. R. *Analytical Chemistry* **2009**, *81*, 10019–10028.

[62] Winkler, H. D. F.; Dzyuba, E. V.; Sklorz, J. A. W.; Beyeh, N. K.; Rissanen, K.; Schalley, C. A. *Chemical Science* **2011**, *2*, 615–624.

[63] Giles, K.; Williams, J. P.; Campuzano, I. *Rapid Communications in Mass Spectrometry* **2011**, *25*, 1559–1566.

[64] Waters Synapt G2, HDMS, System Operator's Guide, *Waters Corporation* **2012**, 1–9.

[65] Schrödinger, E. *Physical Review* **1926**, *28*, 1049–1070.

[66] Alcami, M.; Mo, O.; Yáñez, M. *Mass spectrometry reviews* **2001**, *20*, 195–245.

[67] Echenique, P.; Alonso, J. L. *Molecular Physics* **2007**, *105*, 3057–3098.

[68] Bachrach, S. M. *Computational organic chemistry*, 2nd ed.; John Wiley & Sons, Hoboken, New Jersey, USA, 2014; p. 22-23.

[69] Hohenberg, P.; Kohn, W. *Physical review* **1964**, *136*, B864–B871.

[70] Koch, W.; Holthausen, M. C. *A chemist's guide to density functional theory*; John Wiley & Sons, Weinheim, Germany, 2015; p. 33.

[71] Fiolhais, C.; Nogueira, F.; Marques, M. A. *A primer in density functional theory*; Springer Science & Business Media, Berlin, Heidelberg, 2003; Vol. 620; p. 16.

[72] Perdew, J. P.; Schmidt, K. *AIP Conference Proceedings* **2001**, *577*, 1–20.

[73] Jaeger, M.; Freitag, L.; Gonzalez, L. *Coordination Chemistry Reviews* **2015**, *304*, 146–165.

[74] Schwabe, T.; Grimme, S. *Physical Chemistry Chemical Physics* **2006**, *8*, 4398–4401.

[75] Becke, A. D. *Journal of Chemical Physics* **1993**, *98*, 5648–5652.

[76] Lee, C.; Yang, W.; Parr, R. G. *Physical review B* **1988**, *37*, 785–789.

[77] Bachrach, S. M. *Computational organic chemistry*, 2nd ed.; John Wiley & Sons, Hoboken, New Jersey, USA, 2014; p. 25.

[78] Stephens, P.; Devlin, F.; Chabalowski, C.; Frisch, M. J. *The Journal of Physical Chemistry* **1994**, *98*, 11623–11627.

[79] Zhao, Y.; Truhlar, D. G. *Theoretical Chemistry Accounts* **2008**, *120*, 215–241.

[80] Rezac, J.; Hobza, P. *Chemical Reviews* **2016**, *116*, 5038–5071.

[81] Hill, S. E.; Feller, D. *International Journal of Mass Spectrometry* **2000**, *201*, 41–58.

[82] Achazi, A. J.; von Krbek, L. K. S.; Schalley, C. A.; Paulus, B. *Journal of Computational Chemistry* **2016**, *37*, 18–24.

[83] Achazi, A. J.; Mollenhauer, D.; Paulus, B. *Beilstein Journal of Organic Chemistry* **2015**, *11*, 687–692.

[84] Marshall, M. S.; Burns, L. A.; Sherrill, C. D. *The Journal of Chemical Physics* **2011**, *135*, 194102.

[85] Sherrill, C. D.; Takatani, T.; Hohenstein, E. G. *The Journal of Physical Chemistry A* **2009**, *113*, 10146–10159.

[86] Granatier, J.; Pitonak, M.; Hobza, P. *Journal of Chemical Theory and Computation* **2012**, *8*, 2282–2292.

[87] Grimme, S.; Antony, J.; Ehrlich, S.; Krieg, H. *The Journal of Chemical Physics* **2010**, *132*, 154104.

[88] Thanthiriwatte, K. S.; Hohenstein, E. G.; Burns, L. A.; Sherrill, C. D. *Journal of Chemical Theory and Computation* **2010**, *7*, 88–96.

[89] Bauza, A.; Alkorta, I.; Frontera, A.; Elguero, J. *Journal of Chemical Theory and Computation* **2013**, *9*, 5201–5210.

[90] Karthikeyan, S.; Sedlak, R.; Hobza, P. *The Journal of Physical Chemistry A* **2011**, *115*, 9422–9428.

[91] Rezac, J.; de la Lande, A. *Journal of Chemical Theory and Computation* **2015**, *11*, 528–537.

[92] Hohenstein, E. G.; Chill, S. T.; Sherrill, C. D. *Journal of Chemical Theory and Computation* **2008**, *4*, 1996–2000.

[93] Staroverov, V. N.; Scuseria, G. E.; Tao, J.; Perdew, J. P. *The Journal of Chemical Physics* **2003**, *119*, 12129–12137.

[94] Grimme, S.; Hansen, A.; Brandenburg, J. G.; Bannwarth, C. *Chemical Reviews* **2016**, *116*, 5105–5154.

[95] Antony, J.; Sure, R.; Grimme, S. *Chemical Communications* **2015**, *51*, 1764–1774.

[96] Caldeweyher, E.; Bannwarth, C.; Grimme, S. *The Journal of Chemical Physics* **2017**, *147*, 034112.

[97] Wright, P.; Alex, A.; Nyaruwata, T.; Parsons, T.; Pullen, F. *Rapid Communications in Mass Spectrometry* **2010**, *24*, 1025–1031.

[98] Aiken, A. C.; DeCarlo, P. F.; Jimenez, J. L. *Analytical chemistry* **2007**, *79*, 8350–8358.

[99] McLafferty, F. W.; Tureček, F.; Turecek, F. *Interpretation of mass spectra*; University science books, Sausalito, USA, 1993.

[100] McLafferty, F. W. *Analytical Chemistry* **1959**, *31*, 477–477.

[101] Beavis, R. C.; Colby, S. M.; Goodacre, R.; Harrington, P. d. B.; Reilly, J. P.; Sokolow, S.; Wilkerson, C. W. *Encyclopedia of Analytical Chemistry: Applications, Theory and Instrumentation* **2006**, Artificial intelligence and expert systems in mass spectrometry (https://doi.org/10.1002/9780470027318.a6002).

[102] Buchanan, B. G.; Smith, D.; White, W.; Gritter, R.; Feigenbaum, E.; Lederberg, J.; Djerassi, C. *Journal of the American Chemical Society* **1976**, *98*, 6168–6178.

[103] Bristow, A. W.; Webb, K. S.; Lubben, A. T.; Halket, J. *Rapid communications in mass spectrometry* **2004**, *18*, 1447–1454.

[104] Hopley, C.; Bristow, T.; Lubben, A.; Simpson, A.; Bull, E.; Klagkou, K.; Herniman, J.; Langley, J. *Rapid Communications in Mass Spectrometry* **2008**, *22*, 1779–1786.

[105] Klagkou, K.; Pullen, F.; Harrison, M.; Organ, A.; Firth, A.; Langley, G. J. *Rapid communications in mass spectrometry* **2003**, *17*, 2373–2379.

[106] Holman, S. W.; Wright, P.; Langley, G. J. *Rapid Communications in Mass Spectrometry* **2008**, *22*, 2355–2365.

[107] Wright, P.; Alex, A.; Gibson, D.; Jones, R.; Macrae, P. *Rapid Communications in Mass Spectrometry* **2005**, *19*, 2005–2014.

[108] Hufsky, F.; Scheubert, K.; Böcker, S. *TrAC Trends in Analytical Chemistry* **2014**, *53*, 41–48.

[109] Men, L.; Wang, Y. *Rapid Communications in Mass Spectrometry* **2005**, *19*, 23–30.

[110] Bythell, B. J.; Molesworth, S.; Osburn, S.; Cooper, T.; Paizs, B.; Van Stipdonk, M. *Journal of the American Society for Mass Spectrometry* **2008**, *19*, 1788–1798.

[111] Bourcier, S.; Hoppilliard, Y. *Rapid Communications in Mass Spectrometry* **2009**, *23*, 93–103.

[112] Crotti, A. E.; Fonseca, T.; Hong, H.; Staunton, J.; Galembeck, S. E.; Lopes, N. P.; Gates, P. J. *International Journal of Mass Spectrometry* **2004**, *232*, 271–276.

[113] Alex, A.; Harvey, S.; Parsons, T.; Pullen, F. S.; Wright, P.; Riley, J.-A. *Rapid Communications in Mass Spectrometry* **2009**, *23*, 2619–2627.

[114] Wright, P.; Alex, A.; Pullen, F. *Rapid Communications in Mass Spectrometry* **2014**, *28*, 1127–1143.

[115] Pracht, P.; Bauer, C. A.; Grimme, S. *Journal of Computational Chemistry* **2017**, *38*, 2618–2631.

[116] Asgeirsson, V.; Bauer, C. A.; Grimme, S. *Chemical Science* **2017**, *8*, 4879–4895.

[117] Troć, A.; Zimnicka, M.; Danikiewicz, W. *Journal of Mass Spectrometry* **2015**, *50*, 542–548.

[118] Révész, g.; Schröder, D.; Rokob, T. A.; Havlík, M.; Dolenský, B. *Angewandte Chemie International Edition* **2011**, *50*, 2401–2404.

[119] Carroy, G.; Lemaur, V.; De Winter, J.; Isaacs, L.; De Pauw, E.; Cornil, J.; Gerbaux, P. *Physical Chemistry Chemical Physics* **2016**, *18*, 12557–12568.

[120] Carroy, G.; Daxhelet, C.; Lemaur, V.; De Winter, J.; De Pauw, E.; Cornil, J.; Gerbaux, P. *Chemistry-A European Journal* **2016**, *22*, 4528–4534.

[121] Servage, K. A.; Silveira, J. A.; Fort, K. L.; Russell, D. H. *The Journal of Physical Chemistry Letters* **2014**, *5*, 1825–1830.

[122] Schubert, F.; Rossi, M.; Baldauf, C.; Pagel, K.; Warnke, S.; von Helden, G.; Filsinger, F.; Kupser, P.; Meijer, G.; Salwiczek, M.; Koksch, B.; Scheffler, M.; Blum, V. *Physical Chemistry Chemical Physics* **2015**, *17*, 7373–7385.

[123] Santos, J. J.; Toma, S. H.; Lalli, P. M.; Riccio, M. F.; Eberlin, M. N.; Toma, H. E.; Araki, K. *Analyst* **2012**, *137*, 4045–4051.

[124] Troć, A.; Gajewy, J.; Danikiewicz, W.; Kwit, M. *Chemistry – A European Journal* **2016**, *22*, 13258–13264.

[125] Hanozin, E.; Mignolet, B.; Morsa, D.; Sluysmans, D.; Duwez, A.-S.; Stoddart, J. F.; Remacle, F.; De Pauw, E. *ACS Nano* **2017**, *11*, 10253–10263.

[126] Mohr, S.; Eixarch, M.; Amsler, M.; Mantsinen, M. J.; Genovese, L. *Nuclear Materials and Energy* **2018**, *15*, 64–70.

[127] Koch, W.; Holthausen, M. C. *A chemist's guide to density functional theory*; John Wiley & Sons, Weinheim, Germany, 2015; p. 113.

[128] Ramachandran, K.; Deepa, G.; Namboori, K. *Computational chemistry and molecular modeling: principles and applications*; Springer Science & Business Media, Berlin, Heidelberg, Germany, 2008; p. 6.

[129] Dewar, M. J.; Thiel, W. *Journal of the American Chemical Society* **1977**, *99*, 4899–4907.

[130] Ramachandran, K.; Deepa, G.; Namboori, K. *Computational chemistry and molecular modeling: principles and applications*; Springer Science & Business Media, Berlin, Heidelberg, Germany, 2008; p. 141.

[131] Dewar, M. J.; Zoebisch, E. G.; Healy, E. F.; Stewart, J. J. *Journal of the American Chemical Society* **1985**, *107*, 3902–3909.

[132] Stewart, J. J. *Journal of Computational Chemistry* **1989**, *10*, 221–264.

[133] Huczynski, A.; Przybylski, P.; Brzezinski, B. *Journal of Molecular Structure* **2006**, *788*, 176–183.

[134] March, R. E.; Lewars, E. G.; Stadey, C. J.; Miao, X.-S.; Zhao, X.; Metcalfe, C. D. *International Journal of Mass Spectrometry* **2006**, *248*, 61–85.

[135] Hofmeister, G. E.; Zhou, Z.; Leary, J. A. *Journal of the American Chemical Society* **1991**, *113*, 5964–5970.

[136] Wang, H.-Y.; Zhang, X.; Guo, Y.-L.; Tang, Q.-H.; Lu, L. *Journal of the American Society for Mass Spectrometry* **2006**, *17*, 253–263.

[137] Molina, E. R.; Eizaguirre, A.; Haldys, V.; Urban, D.; Doisneau, G.; Bourdreux, Y.; Beau, J.-M.; Salpin, J.-Y.; Spezia, R. *ChemPhysChem* **2017**, *18*, 2812–2823.

[138] Wollschläger, J. M.; Simon, K.; Gaedke, M.; Schalley, C. A. *Chemical Communications* **2018**, *54*, 4967–4970.

[139] Fabro, S.; Smith, R. L.; Williams, R. *Nature* **1967**, *215*, 296–296.

[140] Zhou, S.; Wang, F.; Hsieh, T.-C.; M Wu, J.; Wu, E. *Current medicinal chemistry* **2013**, *20*, 4102–4108.

[141] Sawada, M.; Okumura, Y.; Yamada, H.; Takai, Y.; Takahashi, S.; Kaneda, T.; Hirose, K.; Misumi, S. *Organic Mass Spectrometry* **1993**, *28*, 1525–1528.

[142] Lebrilla, C. B. *Accounts of Chemical Research* **2001**, *34*, 653–661.

[143] Tao, W. A.; Wu, L.; Cooks, R. G. *Chemical Communications* **2000**, 2023–2024.

[144] Tao, W. A.; Gozzo, F. C.; Cooks, R. G. *Analytical Chemistry* **2001**, *73*, 1692–1698.

[145] Augusti, D. V.; Augusti, R.; Carazza, F.; Cooks, R. G. *Chemical Communications* **2002**, 2242–2243.

[146] Laskin, J.; Futrell, J. H. *The Journal of Physical Chemistry A* **2000**, *104*, 8829–8837.

[147] Nagy, G.; Pohl, N. L. B. *Analytical Chemistry* **2015**, *87*, 4566–4571.

[148] Fujihara, A.; Maeda, N.; Doan, T. N.; Hayakawa, S. *Journal of the American Society for Mass Spectrometry* **2017**, *28*, 224–228.

[149] Dwivedi, P.; Wu, C.; Matz, L. M.; Clowers, B. H.; Siems, W. F.; Hill, H. H. *Analytical Chemistry* **2006**, *78*, 8200–8206.

[150] Yu, X.; Yao, Z.-P. *Analytica Chimica Acta* **2017**, *968*, 1–20.

[151] Zehnacker, A. *Chiral recognition in the gas phase*; CRC Press, Boca Raton, USA, 2010.

[152] Zehnacker, A.; Suhm, M. *Angewandte Chemie International Edition* **2008**, *47*, 6970–6992.

[153] Wollschläger, J. M.; Schalley, C. A. *ChemPhotoChem* **2019**, in press (doi: https://doi.org/10.1002/cptc.201800251).

[154] Hartley, G. S. *Nature* **1937**, *140*, 281–281.

[155] Bandara, H. M. D.; Burdette, S. C. *Chemical Society Reviews* **2012**, *41*, 1809–1825.

[156] Renner, C.; Moroder, L. *ChemBioChem* **2006**, *7*, 868–878.

[157] Barrett, C. J.; Mamiya, J.-i.; Yager, K. G.; Ikeda, T. *Soft Matter* **2007**, *3*, 1249–1261.

[158] Yesodha, S. K.; Pillai, C. K. S.; Tsutsumi, N. *Progress in Polymer Science* **2004**, *29*, 45–74.

[159] Ruslim, C.; Ichimura, K. *Journal of Materials Chemistry* **1999**, *9*, 673–681.

[160] Weber, C.; Liebig, T.; Gensler, M.; Pithan, L.; Bommel, S.; Bleger, D.; Rabe, J. P.; Hecht, S.; Kowarik, S. *Macromolecules* **2015**, *48*, 1531–1537.

[161] Urner, L. H.; Thota, B. N. S.; Nachtigall, O.; Warnke, S.; von Helden, G.; Haag, R.; Pagel, K. *Chemical Communications* **2015**, *51*, 8801–8804.

[162] Bull, J. N.; Scholz, M. S.; Coughlan, N. J.; Bieske, E. J. *Physical Chemistry Chemical Physics* **2017**, *19*, 12776–12783.

[163] Scholz, M. S.; Bull, J. N.; Coughlan, N. J. A.; Carrascosa, E.; Adamson, B. D.; Bieske, E. J. *The Journal of Physical Chemistry A* **2017**, *121*, 6413–6419.

[164] Beharry, A. A.; Woolley, G. A. *Chemical Society Reviews* **2011**, *40*, 4422–4437.

[165] Beharry, A. A.; Sadovski, O.; Woolley, G. A. *Journal of the American Chemical Society* **2011**, *133*, 19684–19687.

[166] Dias, A.; Piedade, M. M. D.; Simões, J. M.; Simoni, J.; Teixeira, C.; Diogo, H.; Meng-Yan, Y.; Pilcher, G. *The Journal of Chemical Thermodynamics* **1992**, *24*, 439–447.

[167] Wang, J.; Wolf, R. M.; Caldwell, J. W.; Kollman, P. A.; Case, D. A. *Journal of Computational Chemistry* **2004**, *25*, 1157–1174.

[168] Allouche, A.-R. *Journal of Computational Chemistry* **2011**, *32*, 174–182.

[169] Schröder, H. V.; Wollschläger, J. M.; Schalley, C. A. *Chemical Communications* **2017**, *53*, 9218–9221.

[170] Schröder, H. V.; Sobottka, S.; Nößler, M.; Hupatz, H.; Gaedke, M.; Sarkar, B.; Schalley, C. A. *Chemical Science* **2017**, *8*, 6300–6306.

[171] Hansen, T. K.; Joergensen, T.; Stein, P. C.; Becher, J. *The Journal of Organic Chemistry* **1992**, *57*, 6403–6409.

[172] Svenstrup, N.; Rasmussen, K. M.; Hansen, T. K.; Becher, J. *Synthesis* **1994**, *1994*, 809–812.

[173] Schröder, H. V.; Hupatz, H.; Achazi, A. J.; Sobottka, S.; Sarkar, B.; Paulus, B.; Schalley, C. A. *Chemistry–A European Journal* **2017**, *23*, 2960–2967.

[174] Hanozin, E.; Morsa, D.; De Pauw, E. *Proteomics* **2015**, *15*, 2823–2834.

[175] Schröder, H. V.; Stein, F.; Wollschläger, J. M.; Sobottka, S.; Gaedke, M.; Sarkar, B.; Schalley, C. A. *Angewandte Chemie International Edition* **2019**, *131*, 3534–3538.

[176] Van Craen, D.; Rath, W. H.; Huth, M.; Kemp, L.; Räuber, C.; Wollschläger, J. M.; Schalley, C. A.; Valkonen, A.; Rissanen, K.; Albrecht, M. *Journal of the American Chemical Society* **2017**, *139*, 16959–16966.

[177] Schalley, C. A. *International Journal of Mass Spectrometry* **2000**, *194*, 11–39.

[178] Schug, K. A.; Maier, N. M.; Lindner, W. *Chemical Communications* **2006**, 414–416.

[179] Schug, K.; Frycak, P.; Maier, N. M.; Lindner, W. *Analytical chemistry* **2005**, *77*, 3660–3670.

[180] Cheng, Y.; Hercules, D. M. *Journal of Mass Spectrometry* **2001**, *36*, 834–836.

[181] Gal, J. F.; Stone, M.; Lebrilla, C. B. *International Journal of Mass Spectrometry* **2003**, *222*, 259–267.

[182] Botta, B.; Caporuscio, F.; D'Acquarica, I.; Delle Monache, G.; Subissati, D.; Tafi, A.; Botta, M.; Filippi, A.; Speranza, M. *Chemistry–A European Journal* **2006**, *12*, 8096–8105.

[183] Fraschetti, C.; Letzel, M. C.; Paletta, M.; Mattay, J.; Speranza, M.; Filippi, A.; Aschi, M.; Rozhenko, A. B. *Journal of Mass Spectrometry* **2012**, *47*, 72–78.

[184] Gasparrini, F.; Pierini, M.; Villani, C.; Filippi, A.; Speranza, M. *Journal of the American Chemical Society* **2008**, *130*, 522–534.

[185] Fraschetti, C.; Pierini, M.; Villani, C.; Gasparrini, F.; Mortera, S. L.; Filippi, A.; Speranza, M. *Rendiconti Lincei* **2011**, *22*, 191–199.

[186] Chu, I. H.; Dearden, D. V.; Bradshaw, J. S.; Huszthy, P.; Izatt, R. M. *Journal of the American Chemical Society* **1993**, *115*, 4318–4320.

[187] Dearden, D. V.; Dejsupa, C.; Liang, Y.; Bradshaw, J. S.; Izatt, R. M. *Journal of the American Chemical Society* **1997**, *119*, 353–359.

[188] Seymour, J. L.; Tureček, F.; Malkov, A. V.; Kočovskỳ, P. *Journal of Mass Spectrometry* **2004**, *39*, 1044–1052.

[189] Grigorean, G.; Cong, X.; Lebrilla, C. B. *International Journal of Mass Spectrometry* **2004**, *234*, 71–77.

[190] Botta, B.; Fraschetti, C.; DAcquarica, I.; Speranza, M.; Novara, F. R.; Mattay, J.; Letzel, M. C. *The Journal of Physical Chemistry A* **2009**, *113*, 14625–14629.

[191] Augusti, D. V.; Augusti, R. *Tetrahedron: Asymmetry* **2005**, *16*, 1881–1885.

[192] Grigorean, G.; Lebrilla, C. B. *Analytical chemistry* **2001**, *73*, 1684–1691.

[193] Karthikraj, R.; Prabhakar, S.; Vairamani, M. *Rapid Communications in Mass Spectrometry* **2012**, *26*, 1385–1391.

[194] Domalain, V.; Hubert-Roux, M.; Tognetti, V.; Joubert, L.; Lange, C. M.; Rouden, J.; Afonso, C. *Chem. Sci.* **2014**, *5*, 3234–3239.

[195] Musbat, L.; Nihamkin, M.; Toker, Y.; Dilger, J.; Fuller, D.; El-Baba, T.; Clemmer, D.; Sarkar, S.; Kronik, L.; Hirshfeld, A. *Physical Review E* **2017**, *95*, 012406.

[196] Adamson, B.; Coughlan, N.; Markworth, P.; Continetti, R.; Bieske, E. *Review of Scientific Instruments* **2014**, *85*, 123109.

[197] Bull, J. N.; Scholz, M. S.; Coughlan, N. J. A.; Kawai, A.; Bieske, E. J. *Analytical Chemistry* **2016**, *88*, 11978–11981.

[198] Lerch, M. M.; Wezenberg, S. J.; Szymanski, W.; Feringa, B. L. *Journal of the American Chemical Society* **2016**, *138*, 6344–6347.

[199] Helmy, S.; Oh, S.; Leibfarth, F. A.; Hawker, C. J.; Read de Alaniz, J. *The Journal of Organic Chemistry* **2014**, *79*, 11316–11329.

[200] Bull, J. N.; Carrascosa, E.; Mallo, N.; Scholz, M. S.; da Silva, G.; Beves, J. E.; Bieske, E. J. *The Journal of Physical Chemistry Letters* **2018**, *9*, 665–671.

[201] Rogers, R. A.; Rodier, A. R.; Stanley, J. A.; Douglas, N. A.; Li, X.; Brittain, W. J. *Chemical Communications* **2014**, *50*, 3424–3426.

[202] Allison, T. M.; Reading, E.; Liko, I.; Baldwin, A. J.; Laganowsky, A.; Robinson, C. V. *Nature Communications* **2015**, *6*, 8551–8561.

[203] Kalenius, E.; Groessl, M.; Rissanen, K. *Nature Reviews Chemistry* **2019**, *3*, 4–14.

[204] Zhang, H.; Grabenauer, M.; Bowers, M. T.; Dearden, D. V. *The Journal of Physical Chemistry A* **2009**, *113*, 1508–1517.

[205] Lee, T.-C.; Kalenius, E.; Lazar, A. I.; Assaf, K. I.; Kuhnert, N.; Grün, C. H.; Jänis, J.; Scherman, O. A.; Nau, W. M. *Nature Chemistry* **2013**, *5*, 376.

[206] Hanozin, E.; Mignolet, B.; Morsa, D.; Sluysmans, D.; Duwez, A.-S.; Stoddart, J. F.; Remacle, F.; De Pauw, E. *ACS Nano* **2017**, *11*, 10253–10263.

[207] Sawyer, H. A.; Marini, J. T.; Stone, E. G.; Ruotolo, B. T.; Gillig, K. J.; Russell, D. H. *Journal of the American Society for Mass Spectrometry* **2005**, *16*, 893–905.

[208] Zhang, W.; Quernheim, M.; Räder, H. J.; Müllen, K. *Analytical Chemistry* **2016**, *88*, 952–959.

[209] Azargun, M.; Fridgen, T. D. *Physical Chemistry Chemical Physics* **2015**, *17*, 25778–25785.

[210] Cruz-Ortiz, A. F.; Rossa, M.; Berthias, F.; Berdakin, M.; Maitre, P.; Pino, G. A. *The Journal of Physical Chemistry Letters* **2017**, *8*, 5501–5506.

[211] Wu, R.; Yang, B.; Berden, G.; Oomens, J.; Rodgers, M. *The Journal of Physical Chemistry B* **2015**, *119*, 2795–2805.

[212] González Flórez, A. I.; Mucha, E.; Ahn, D.-S.; Gewinner, S.; Schöllkopf, W.; Pagel, K.; von Helden, G. *Angewandte Chemie International Edition* **2016**, *55*, 3295–3299.

[213] Vu, N.; Brown, J.; Giles, K.; Zhang, Q. *Rapid Communications in Mass Spectrometry* **2017**, *31*, 1415–1423.

[214] Kluyver, T.; Ragan-Kelley, B.; Pérez, F.; Granger, B. E.; Bussonnier, M.; Frederic, J.; Kelley, K.; Hamrick, J. B.; Grout, J.; Corlay, S. Jupyter Notebooks-a publishing format for reproducible computational workflows. ELPUB. 2016; pp 87–90.

[215] Van Der Walt, S.; Colbert, S. C.; Varoquaux, G. *Computing in Science & Engineering* **2011**, *13*, 22.

[216] Bressert, E. *SciPy and NumPy: an overview for developers*; O'Reilly Media, Inc., Sebastopol, USA, 2012.

[217] Hunter, J. D. *Computing in science & engineering* **2007**, *9*, 90.

[218] Pedregosa, F.; Varoquaux, G.; Gramfort, A.; Michel, V.; Thirion, B.; Grisel, O.; Blondel, M.; Prettenhofer, P.; Weiss, R.; Dubourg, V. *Journal of Machine Learning Research* **2011**, *12*, 2825–2830.

[219] Meurer, A.; Smith, C. P.; Paprocki, M.; Čertík, O.; Kirpichev, S. B.; Rocklin, M.; Kumar, A.; Ivanov, S.; Moore, J. K.; Singh, S. *PeerJ Computer Science* **2017**, *3*, e103.

[220] Abadi, M.; Barham, P.; Chen, J.; Chen, Z.; Davis, A.; Dean, J.; Devin, M.; Ghemawat, S.; Irving, G.; Isard, M. Tensorflow: A system for large-scale machine learning. 12th {USENIX} Symposium on Operating Systems Design and Implementation ({OSDI} 16). 2016; pp 265–283.

[221] Bush, M. F.; Campuzano, I. D. G.; Robinson, C. V. *Analytical Chemistry* **2012**, *84*, 7124–7130.

6.2 Curriculum vitae

Mein Lebenslauf wird aus Gründen des Datenschutzes in der elektronischen Fassung meiner Arbeit nicht veröffentlicht.

6.3 List of publications

1. Ion mobility and gas phase H/D exchange: revealing the importance of a single hydrogen bond for the chiral recognition of crown ether ammonium complexes
   Wollschläger, J. M. ; Simon, K.; Gaedke, M. and Schalley, C. A.
   Chem. Commun. **2018**, *54*, 4967-4970. http://dx.doi.org/10.1039/C8CC01671B

2. Ion Mobility-Mass Spectrometric Investigation on the Photoisomerization of a 4,4'-Diamidoazobenzene Model
   Wollschläger, J. M. and Schalley, C. A.
   ChemPhotoChem **2019**, *in press*. http://dx.doi.org/10.1002/cptc.201800251

3. Redox-controlled self-inclusion of a lasso-type pseudo[1]rotaxane
   Schröder, H. V.; Wollschläger, J. M. and Schalley, C. A.
   Chem. Commun. **2017**, *53*, 9218-9221. http://dx.doi.org/10.1039/c7cc05259f

4. Accordion-Like Motion in Electrochemically Switchable Crown Ether/ Ammonium Oligorotaxanes
   Schröder, H. V.; Stein, F.; Wollschläger, J. M. and Sobottka, S.; Gaedke, M.; Sarkar, B. and Schalley, C. A.
   Angew. Chem. Int. Ed. **2019**, *58*, 1-6. http://dx.doi.org/10.1002/anie.201813265

5. Chasing Weak Forces: Hierarchically Assembled Helicates as a Probe for the Evaluation of the Energetics of Weak Interactions
   Van Craen, D.; Rath, W. H.; Huth, M.; Kemp, L.; Räuber, C.; Wollschläger, J. M. ; Schalley, C. A.; Valkonen, A.; Rissanen, K. and Albrecht, M.
   J. Am. Chem. Soc. **2017**, *139*, 16959-16966. http://dx.doi.org/10.1021/jacs.7b10098

6.4 Acknowledgments/Danksagung

Ich möchte mich an dieser Stelle bei allen bedanken, welche mich während meiner Arbeit unterstützt haben. Ohne Euch wäre diese Arbeit nicht möglich gewesen!
Zuallererst möchte ich mich bei Prof. Dr. Christoph A. Schalley bedanken, der mich in die Welt der Supramolekularen Chemie und Massenspektrometrie eingeführt hat. In den letzten Jahren konnte ich durch seine Unterstützung an vielen spannenden Projekten arbeiten und habe dabei viel gelernt.
Ich danke Prof. Dr. Beate Paulus für die Übernahme des Zweitgutachtens und die Betreuung im SFB 765.
Dr. Andreas Springer danke ich von ganzem Herzen für die Einführung in die Geräte und die tolle Hilfestellung in vielen Projekten. Außerdem möchte ich auch allen anderen Mitarbeitern der Massenspektrometrie für die schöne Arbeitsatmosphäre danken, insbesondere Fabian Klautzsch als Ansprechpartner für das FT-ICR und viele interessante Gespräche.
Ferner danke ich Hendrik Schröder für die Zusammenarbeit in zwei spannenden Projekten sowie den Studenten Konstantin Simon, Lukasz Polewski und Thobias Trebut.
Schließlich möchte ich mich noch bei der gesamten Arbeitsgruppe Schalley für die Freundlichkeit, Kollegialität und Unterstützung bedanken.

Ich danke dem SFB 765 sowie der Studienstiftung des deutschen Volkes für die finanzielle Unterstützung im Rahmen eines Stipendiums.

6.5 Data analysis workflow and software development

Methods to interactively explore data form a crucial strategy to tackle any scientific data-heavy problem. Jupyter notebooks (http://jupyter.org/) provide an interactive computing environment that allows the convenient document creation, editing and sharing.[214] What really sets the jupyter project apart from other software solutions is the ability to embedd rich media and executable code into a single HTML notebook. Code is written in python, a general purpose programming language—so the possibilities are endless. Besides the convenience of use and the many possibilities for adaptation, jupyter is also easily integrated into any existing workflow. Furthermore, as jupyter notebooks typically rely on the excellent open source ecosystem of numeric computing libraries such as numpy,[215] scipy,[216] matplotlib,[217] scikit-learn,[218] sympy,[219] tensorflow,[220] among many others, the results are highly transparent and easily reproducible. Integration of computation and visualization into jupyter HTML notebooks offers a highly modular approach for scientific computing and data analysis.

As shown in Figure 30, a small python library, `libms`, was used to provide common data workflows including the visualization of MS, MS/MS and IMS spectra, the automated plot of survival yield runs and the automated calibration of TW-IMS data. For the prediction of CCS values, an open source implementation of the PA and EHS CCS prediction algorithms, `goccs`, was developed by the author.[a] Further information regarding this project can be found on the author's github page (https://github.com/jmwoll).

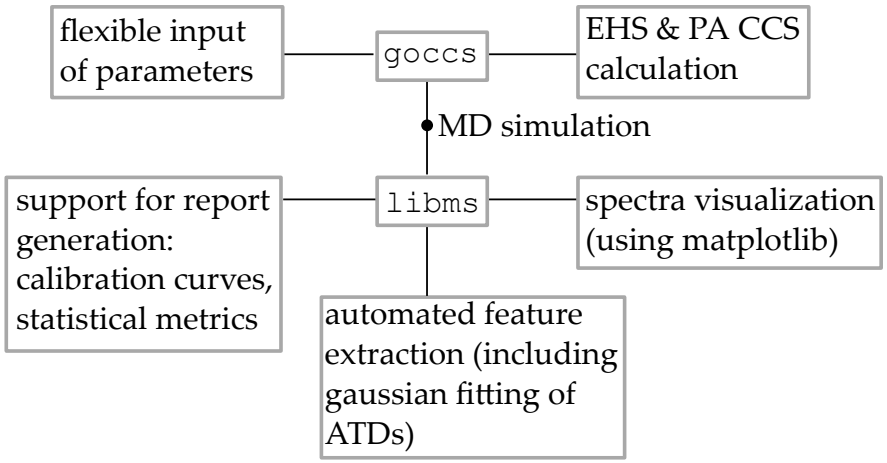

Figure 30: Overview over data analysis software developed for my thesis.

[a]The GPL3 licensed `goccs` software can be found under the DOI: https://doi.org/10.5281/zenodo.1285206

6.6 Typical TW-IMS CCS calibration procedure

Typically, TW-IMS CCS calibration has been performed using polyalanine reference standard. For best results, the IMS cell is started and let to equilibrate for at least 45 min. This is done to ensure that the internal pressure of the IMS cell settles to a constant value. In the mean time, a solution of 0.01 mg-0.05 mg polyalanine in 1 mL acetonitrile is prepared, to which 0.4% HCOOH are added. The mass spectrum should give a polymer distribution as depicted in Figure 31 (bottom) and a high linear correlation, as shown in Figure 31 (top right).

Table 8 shows the m/z-values and the corresponding CCS values in helium and nitrogen.

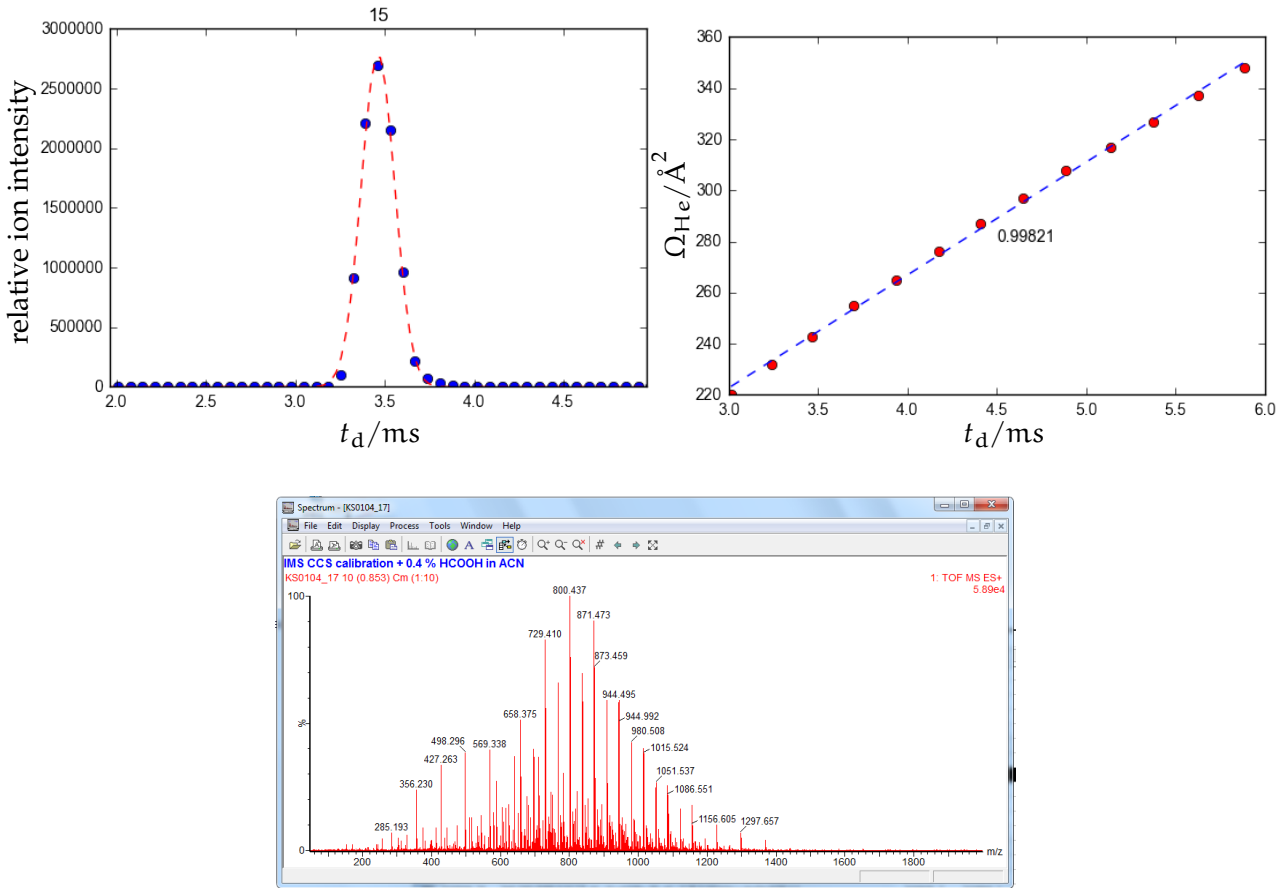

Figure 31: top left: Example of an automated gaussian fit for the fully automated extraction of drift time centroids from the ATD. top right: A typical linear calibration curve obtained as the final result. bottom: Mass spectrum of polyalanine (0.01 mg/1 mL, acetonitrile+0.4% HCOOH) as used for TW-IMS CCS calibration.

Table 8: Important data for TW-IMS calibration using the polyalanine reference.[221]

formula	$\Omega_{He}/Å^2$	$\Omega_{N_2}/Å^2$	m/z	z
$3Ala + H^{\oplus}$	89	151	232.13	+1
$4Ala + H^{\oplus}$	100	166	303.17	+1
$5Ala + H^{\oplus}$	114	181	374.20	+1
$6Ala + H^{\oplus}$	128	195	445.24	+1
$7Ala + H^{\oplus}$	141	211	516.28	+1
$8Ala + H^{\oplus}$	157	228	587.31	+1
$9Ala + H^{\oplus}$	170	243	658.35	+1
$10Ala + H^{\oplus}$	181	256	729.39	+1
$11Ala + H^{\oplus}$	194	271	800.43	+1
$12Ala + H^{\oplus}$	206	282	871.46	+1
$13Ala + H^{\oplus}$	217	294	942.50	+1
$14Ala + H^{\oplus}$	228	306	1013.54	+1
$11Ala + 2H^{\oplus}$	197	296	400.72	+2
$12Ala + 2H^{\oplus}$	208	309	436.24	+2
$13Ala + 2H^{\oplus}$	220	320	471.75	+2
$14Ala + 2H^{\oplus}$	232	333	507.27	+2
$15Ala + 2H^{\oplus}$	243	344	542.79	+2
$16Ala + 2H^{\oplus}$	255	357	578.31	+2
$17Ala + 2H^{\oplus}$	265	369	613.83	+2
$18Ala + 2H^{\oplus}$	276	380	649.35	+2
$19Ala + 2H^{\oplus}$	287	393	684.87	+2
$20Ala + 2H^{\oplus}$	297	404	720.38	+2
$21Ala + 2H^{\oplus}$	308	416	755.90	+2
$22Ala + 2H^{\oplus}$	317	428	791.42	+2
$23Ala + 2H^{\oplus}$	327	437	826.94	+2
$24Ala + 2H^{\oplus}$	337	448	862.46	+2
$25Ala + 2H^{\oplus}$	348	458	897.98	+2
$26Ala + 2H^{\oplus}$	358	470	933.50	+2
$19Ala + 3H^{\oplus}$	338	482	456.91	+3
$20Ala + 3H^{\oplus}$	348	491	480.59	+3
$21Ala + 3H^{\oplus}$	361	501	504.27	+3
$22Ala + 3H^{\oplus}$	373	518	527.95	+3
$23Ala + 3H^{\oplus}$	386	532	551.63	+3
$24Ala + 3H^{\oplus}$	399	545	575.31	+3
$25Ala + 3H^{\oplus}$	412	561	598.99	+3
$26Ala + 3H^{\oplus}$	425	576	622.67	+3
$27Ala + 3H^{\oplus}$	438	592	646.35	+3
$28Ala + 3H^{\oplus}$	452	606	670.02	+3
$29Ala + 3H^{\oplus}$	465	621	693.70	+3
$30Ala + 3H^{\oplus}$	479	634	717.38	+3
$31Ala + 3H^{\oplus}$	490	649	741.06	+3
$32Ala + 3H^{\oplus}$	502	666	764.74	+3
$33Ala + 3H^{\oplus}$	516	674	788.42	+3